ENGINEERING A MULTI-FUNCTIONAL DNA ORIGAMI NANOROD FOR THE CONTROL OF NANOSCALE PROCESSES

A Dissertation
Presented to
The Academic Faculty

by

Travis Andrew Meyer

In Partial Fulfillment
of the Requirements for the Degree
Doctor of Philosophy in the
Wallace H. Coulter Department of Biomedical Engineering

Georgia Institute of Technology
Emory University
August 2019

ENGINEERING A MULTI-FUNCTIONAL DNA ORIGAMI NANOROD FOR THE CONTROL OF NANOSCALE PROCESSES

Approved by:

Dr. Yonggang Ke, Advisor
Biomedical Engineering
Emory University

Dr. Gang Bao, Advisor
Bioengineering
Rice University

Dr. Hui Mao
Radiology
Emory University

Dr. M.G. Finn
Chemistry
Georgia Institute of Technology

Dr. Gabe Kwong
Biomedical Engineering
Georgia Institute of Technology

Dr. Younan Xia
Biomedical Engineering
Georgia Institute of Technology

Date Approved: [July 1st, 2019]

To Olivia Anne Meyer

ACKNOWLEDGEMENTS

As with all scientific endeavors, the work conducted for this thesis was not done in a vacuum, and I have many people to thank for their help, advice, assistance, and encouragement.

I first would like to thank my advisors, Dr. Yonggang Ke and Dr. Gang Bao, who have been fantastic mentors and have taught me so much about what it means to be a good scientist. I especially am grateful for their support in allowing me to pursue my own research plans. I came to them as a fresh-faced graduate student with a poorly thought out research plan and they were gracious enough to allow me to work on it for the next 5 years, providing the scientific, personal, and financial support to allow me to see my idea to its fruition. I would also like to thank my committee members, who have been a fantastic resource as I've progressed through my thesis. Their helpful suggestions and alternate viewpoints have helped shape the work presented here for the better.

I want to thank all of the past members of the Bao lab - you helped facilitate my easy transition into graduate school and the collegial environment and fun we had, from lab Olympics to tuxedo shirt Tuesdays to lab happy hours, meant so much to me. I would especially like to thank Dr. Sheng Tong and Dr. Chris Quinto, who taught me everything I know about synthesizing and working with iron oxide nanoparticles and were very influential in all of the work I have done in that area. Dr. Sheng Tong also provided the streptavidin-coated IONPs used for portions of Specific Aim 1. I would also like to thank all of the past and current members of the Ke lab for all of their help and support over the past 5 years. Dr. Pengfei Wang and Dr. Palash Dutta were especially influential in helping

me get started in the DNA nanotechnology field, and I imagine they were both very sick of my constant nagging questions.

I want to thank the numerous collaborators I have worked with who helped make all of this work possible. In particular, I want to thank Dr. Chuan Zhang and Dr. Chenwei Wu from Shanghai Jiao Tong University, who provided the 10nm DNA-coated iron oxide particles used for preliminary studies for Specific Aim 1 as well as the polymer used for synthesizing the 15 nm particles used in the rest of the work. I was literally at my wit's end trying everything I could think of before they kindly shared their materials with us, and the work on DNA-mediated IONP assembly would absolutely not have been completed without their generosity. I also would like to thank Dr. Khalid Salaita and Alisina Bazrafshan from Emory University, who were major partners in the work on the DNA origami motors. The majority of the experimental work (and thus the majority of late nights) as well as the data analysis and figure creation was done by Alisina, and he deserves far more credit than I do for the success of this work. I also want to thank all of the operators and managers of the various core facilities I have used – particularly Dr. Hong Yi at the Robert P. Apkarian Electron Microscopy Core at Emory University.

I want to thank my family and friends for all their support. Graduate school can be a challenging and stressful time, and I would not have survived it without all of you. To all my friends in Atlanta, you made graduate school such a wonderful time in my life and I will never forget all of the wonderful times we've shared over the past 7 years. I could not have asked for a better group of people to make it through graduate school with. I'd like to thank my parents for all their unwavering support and unconditional love - it is because of you both that I am who I am today. Finally, I'd like to thank my wife Alex, who had to put

up with many late nights and long weekends in lab, my constant underestimation of the time it would take me to finish up experiments, and all the other negatives that are part of life as a graduate student. She kept me grounded and sane through the tough moments, bought me donuts when experiments didn't work, and in general was my rock and support for the past 5 years.

Finally, none of this work would have been possible without generous funding from the National Institutes of Health and the National Science Foundation, particularly the NSF Graduate Research Fellowship Program.

.

TABLE OF CONTENTS

LIST OF FIGURES

LIST OF SYMBOLS AND ABBREVIATIONS

16HB	16-Helix Bundle
2D/3D	Two-dimensional/Three-dimensional
AGE	Agarose Gel Electrophoresis
AF647	AlexaFluor-647
AuNP	Gold Nanoparticle
DBCO	Dibenzocyclooctyne
DLS	Dynamic Light Scattering
DNA	Deoxyribonucleic Acid
ssDNA	Single-stranded Deoxyribonucleic Acid
dsDNA	Double-stranded Deoxyribonucleic Acid
DNA-IONP	Deoxyribonucleic Acid-Coated Iron Oxide Nanoparticles
DSPE-PEG	1,2-distearoyl-sn-glycero-3-phosphoethanolamine - poly(ethylene glycol)
IONP	Iron Oxide Nanoparticle
MRI	Magnetic Resonance Imaging
NMR	Nuclear Magnetic Resonance
r_2	T_2 Relaxivity
RNA	Ribonucleic Acid
STV	Streptavidin
STV-IONP	Streptavidin-Conjugated Iron Oxide Nanoparticles
TBE	Tris, Borate, EDTA Buffer
TEM	Transmission Electron Microscopy

SUMMARY

DNA origami has emerged over the past decade as a promising technology for the synthesis and study of matter at the nanoscale, with applications in a wide variety of fields. In this work, we designed and synthesized a DNA origami nanorod capable of providing a support scaffold for the precise spatial arrangement of two different components - iron oxide magnetic nanoparticles and molecular motor foothold domains. Using this system, we are able to demonstrate new functionality of DNA origami nanostructures while simultaneously answering questions about the mechanism of MRI contrast enhancement with clustered iron oxide nanoparticles and the factors that affect rolling nanoscale locomotion.

In the first part of this thesis, iron oxide nanoparticles are assembled onto our DNA nanorod in prescribed patterns to help understand how their spatial organization affects MRI contrast generation. Clustering of these nanocrystals has been previously demonstrated to increase the efficiency of contrast generation, and thus offers promise as a means of synthesizing the next generation of MRI contrast agents. However, current techniques for inducing assembly offer limited control over the properties of the final superstructure, hindering in-depth mechanistic studies into the nature of this enhancement. We designed the DNA origami nanorod to contain binding sites for the iron oxide nanoparticles. We demonstrate successful synthesis of DNA-coated particles using the 'Programmable Atom Equivalent' technique and show successful binding of both these particles and streptavidin-modified commercial iron oxide nanoparticles, finding that the use of DNA-coated particles produces constructs with much higher yield and purity. This

system facilitates the assembly of IONP clusters with precise and independent control over both number and spacing - we assemble up to 4 nanoparticles with reasonable yield and controlled spacing, and also assemble a pair of particles with spacing between 25 and 125 nm in ~10 nm increments. Finally, we show that discrete changes in the number of iron oxide nanoparticles in a cluster between 1 and 3 leads to enhancement in T_2 relaxivity up to 20%, while changes in spacing between 40 and 110 nm shows negligible differences. Saturating the number of binding sites enables the assembly of ~8-9 nanoparticles and produces T_2 relaxivity enhancements up to 140%, which is comparable to previous clustering techniques. Dimerization of DNA origami-iron oxide nanoparticle constructs also facilitates dynamic modulation of T_2 MRI contrast, opening up the possibility for biosensing applications.

In the second part of the thesis, we use our DNA origami nanorod to synthesize a nanoscale molecular motor which exhibits a unique rolling behavior. These motors exhibit super-diffusive motion over several hours with net displacements of several microns and velocities up to 200 nm per minute, which are significant improvements over traditional DNA walkers. We tune the exact location of the motor domain strands - by selectively decorating only certain sides of the rod, we are able to show that motors which are capable of exhibiting a rolling behavior show higher processivity with increased directionality. We also find that the density and polyvalency of motor domains plays a large role in controlling motion, such that net displacement drops when the density of motor domains drops. Finally, we find that the rigidity of the DNA origami rod has an impact on motor behavior, with more flexible structures exhibiting less ballistic motion and lower processivity compared to rigid motors.

The work presented here represents two novel applications of DNA origami nanostructures and offer promise as platform technologies for the further development of the next generation of MRI contrast agents as well as more advanced molecular motors.

CHAPTER 1. INTRODUCTION

Processes that occur at the nanoscale are the foundational building blocks of our world. As such, there is considerable interest in ways to study and manipulate matter at this scale, with applications in a number of fields including biomedicine. Traditional methods for working with nanoscale processes are either are costly and time consuming, such as electron beam lithography, or are limited in their scope, such as canonical nanoparticle synthesis. DNA nanotechnology has emerged over the past decade as a promising technology for bridging this gap, offering the capacity for precise and tunable nanoscale synthesis while maintaining the ease and scale of traditional bottom-up self-assembly. DNA nanotechnology, and DNA origami in particular, has been used to build nanoscale machines with prescribed motions, to organize nanoparticles in order to manipulate light propagation, to study the action of individual proteins, and to develop novel drug delivery vehicles.

The goal of this thesis is to develop novel ways in which DNA origami can be used to manipulate nanoscale processes. To this end, we have developed a single DNA origami nanorod which is used in two distinct studies, highlighting the multifunctionality of this structure. In Chapter 2 I present background information on the field of DNA nanotechnology in general and DNA origami in particular, highlighting applications in which DNA origami structures have been used to create nanoscale machines and organize the assembly of various heteroelements. I also present background on other fields related to work in the 2 studies - magnetic resonance imaging (MRI) and MRI contrast agents, and molecular motors.

In Specific Aim 1 (Chapters 3 and 4), I investigated the effect of iron oxide nanoparticle (IONP) clustering on MRI contrast generation. After confirming that we can induce general clustering using the dual solvent exchange coating technique, we sought to use a 16-helix bundle (16HB) DNA origami rod as a scaffold to control the spatial orientation of the iron oxide nanoparticles. Our hypothesis was that precise changes in the number and spacing of IONPs would lead to changes in T_2 relaxivity. We also hypothesized that dynamic changes in the DNA origami scaffold would translate to dynamic changes in T_2 relaxivity. We first designed, synthesized, and characterized a 16HB DNA origami rod, followed by the investigation of various methods for attaching IONPs to the 16HB. We found DNA-coated IONPs with complementary capture sequences on the DNA origami produced the highest quality 16HB-IONP constructs. We next investigated factors affecting IONP binding to the 16HB rod while also demonstrating the precise control over spacing and number of particles attached to the rod. Finally, we show how the organization of the IONPs on the DNA origami affects T_2 relaxivity of the system, while also showing the dynamic assembly of 16HB dimers leads to alterations in the magnetic signal.

In Specific Aim 2 (Chapter 5) we investigated a new application for the same 16HB rod - the synthesis of the first DNA origami molecular motor, and the first autonomous nanoscale rolling motor of any type. We demonstrate that a structure containing RNA-binding domains extending from the surface can successfully bind to an RNA-coated surface, and that introduction of the nuclease RNase H can induce motion of the 16HB along the surface through a burned-bridge Brownian ratchet mechanism. Careful engineering of the spatial distribution of the RNA-binding motor domains allows us to interrogate the mechanism of locomotion, namely rolling verse walking, as well as to

investigate the effects of manipulating motor domain density and polyvalency on motion. Finally, we alter the mechanical properties of the motor through the introduction of planned defects to investigate the effect of rigidity on the efficiency and directionality of movement.

Combined, this work demonstrates two novel applications for DNA origami nanostructures. We expect this work will serve as an initial platform for further studies into these phenomena and open up a range of new possibilities for the use of structural DNA nanotechnology as MRI contrast agents and theranostic drug delivery agents, as well as molecular motors for DNA computing, biosensing, and molecular robotics.

CHAPTER 2. BACKGROUND

This chapter contains background on the 3 main components of this thesis: DNA nanotechnology, which is the technique used predominately throughout the thesis; Magnetic Nanoparticles and MRI, the basis for Specific Aim 1; Molecular Motors, which is the basis for Specific Aim 2.

2.1 DNA Nanotechnology and DNA Origami

This section will cover some brief details on the DNA origami technique as well as an overview of functional uses of these structures in the literature. Much of this information was covered in a review paper I wrote, and several passages were quoted verbatim from that article[1]. Over the past three decades, deoxyribonucleic acid (DNA), the genetic carrier of information in most living organisms, has seen an ever-expanding role as a material for the construction of nanoscale objects [2-4]. The field of structural DNA nanotechnology dates back to the early 1980's, when Nadrian Seeman hypothesized that structurally-rigid branched DNA constructs, analogous to Holliday Junction structures found in biology, could be used as a material for the construction of nanoscale structures [5]. DNA has several useful characteristics for a construction material; it is a chemically stable biomolecule with a well-defined structure and appealing mechanical properties[2]. Furthermore, the highly specific molecular recognition capability of DNA, mediated by Watson-Crick base-pairing, enables the programmed self-assembly of a large number of unique DNA sequences into well-defined higher-order architectures. The relatively simplistic nature of DNA, both from a structural and recognition stand-point, makes *de*

novo design of DNA nanostructures feasible compared to more complex protein assemblies.

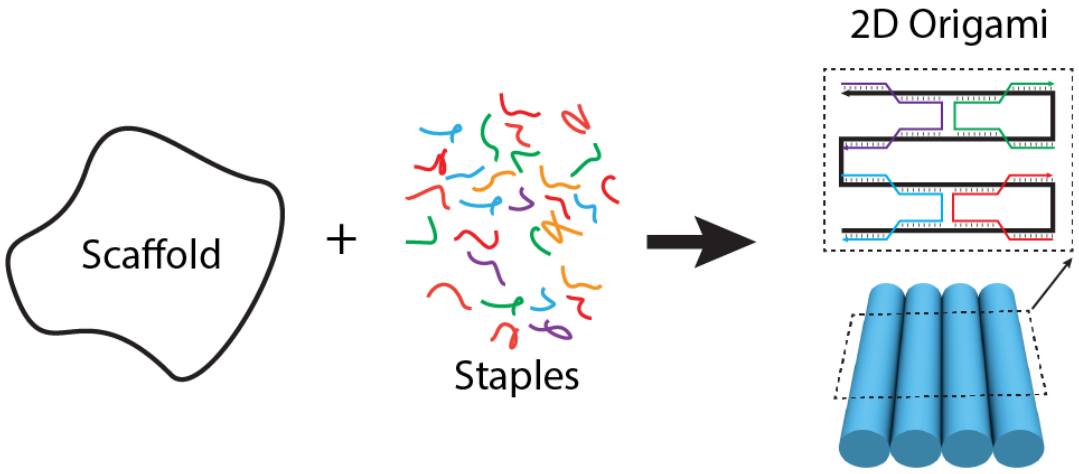

Figure 2-1: Schematic of DNA Origami Assembly. DNA origami structures are produced by annealing a long scaffold strand with many short synthetic staple strands, producing a nanostructure consisting of multiple DNA double-helices linked together into arbitrary shapes.

DNA nanostructures have gradually increased in complexity over the past 3 decades, from a simple cube with a single double helical edges[6] to massive, arbitrarily-prescribed shapes formed from over 400 unique oligonucleotides[7]. A major breakthrough in structural DNA nanotechnology came in 2006 with the development of DNA origami by Paul Rothemund[8]. DNA origami is a process of molecular self-folding: a long single-stranded DNA (scaffold), typically M13 phage genomic DNA (~7000 bases), is folded into prescribed objects by hundreds of short synthetic DNA oligonucleotide "staple strands", typically 20-60 bases long, which are designed to be complementary to different parts of the scaffold DNA (Figure 2-1). Each staple strand consists of several domains which are complementary to linearly distant regions within the scaffold strand - hybridization of these

domains brings the regions into close proximity in 3D space. Staple strands are designed to cross-over between neighboring duplexes, effectively 'stapling' individual helices into larger helical bundles (HB). Full details on the principles of DNA origami design are not particularly relevant to this work but readers are encouraged to look at several excellent review articles for a comprehensive elaboration [9, 10].

In the first report of DNA origami planar, arbitrary-shaped, two-dimensional (2D) objects with length scales around 100 nm were constructed [8]. Simple 3D hollow containers were constructed in 2009 *via* the folding of 2D planar DNA origami sheets, such as a tetrahedron[11] and a cube [12]. A milestone advancement in constructing 3D origami structures was introduced by Shih and coworkers in 2009, in which DNA helices are bundled into a honeycomb lattice to construct solid 3D objects [13]. To simply the design process and enable a general route for the rapid design of sophisticated shapes, they developed the caDNAno software[14]. The Shih group later on demonstrated square [15] and hybrid lattice[16] [17] design concepts. Subsequent work enabled the introduction of curvature by simply adding or deleting bases between adjacent DNA helical crossovers [17]. In a departure from the traditional rigid lattice model, a study published in 2011 by Yan and coworkers used concentric DNA rings to define the surface feature of 3D objects, inducing curvature through the manipulation of strand crossover positions[18].

2.1.1 DNA Origami for Nanofabrication

The DNA origami technique has been used extensively for the fabrication of nanoscale constructs, including many that are unobtainable (or extremely difficult to obtain) with other approaches. At the macroscopic scale, top-down fabrication of materials

is used to create products with specific structures and functions. Unfortunately, this same capability has been difficult to achieve on the nanoscale, as bottom-up self-assembly methods suffer from limited scope due to thermodynamic constraints and top-down methods are time-consuming and costly. DNA origami helps to bridge this fabrication gap, as the ability to self-assemble arbitrary shapes with full addressability allows for the fabrication of nanostructures with well-defined form and the capacity to precisely arrange heteroelements. A particularly appealing aspect of DNA origami is the global addressability - the use of a unique scaffold strand in DNA origami means that the relative spatial location of every single base-pair is known with nanometer precision. This creates a molecular "breadboard", in which guest species can be organized in arbitrary patterns and arrangements on the DNA origami surface. This capacity for precision nanofabrication has positioned DNA origami nanostructures as an excellent platform for studying the effects of spatial organization on interactions between various heteroelements.

Heteroelements are typically incorporated into DNA origami nanostructures through modifications to select staple strands. The most common option is to use modified staple strands in which a unique 'capture' sequence extends as a free, single-stranded protrusion. Heteroelements modified with oligonucleotides bearing the complementary sequence are docked at that location through hybridization. Chemical modifications to staple strands are also used – biotinylated staple strands are frequently used to facilitate the docking of streptavidin-modified heteroelements, for example. By selectively designing which staple strands are chemically modified or contain 'capture' extensions, the position of other molecular species can be organized.

DNA origami has been used for the construction of functional structures consisting entirely of DNA, as well as template structures for the organization of both synthetic nanomaterial components as well as biomolecules, as molds for nanoparticle synthesis, as masks for nanolithography, and as scaffolds for artificial enzyme cascades, *etc*. The devices fabricated using these techniques have been utilized for many applications, including nanoplasmonics, nanophotonics, biosensing, and drug delivery.

2.1.1.1 Nanofabrication of DNA Constructs

That form dictates function, a governing principle of the natural world, is as true at the nanoscale as it is in other areas. Controlling the form of nanostructures enables the control of the functions of these particles. For DNA origami, the ability to tune the precise shape/size of nanoscale features while also controlling the spatial organization of sequence-specific DNA strands has enabled the construction of a wide variety of functional DNA origami nanostructures. One of the best examples of this comes from the work of Hiroshi Sugiyama's group, who developed a single DNA origami chip that has been used to study many different single-molecule processes. The authors designed a 2D rectangular DNA origami structure with a square hole in the center, which they call a "DNA frame" [19]. Four different ssDNA extensions extend into the middle of the hole, providing anchoring points for loading various DNA cargo. The DNA origami frame allows for easy identification of structures using atomic force microscopy (AFM) imaging and added stability to the cargo, while the hole in the center facilitates high resolution AFM imaging by limiting the amount of background near the targets. This chip has been used to study a wide variety of nanoscale processes with high-speed AFM, including transcription factor binding[20], photoresponsive DNA elements[21], DNA repair[22], Cre-lox

recombination[23], CRISPR-Cas9 activity[24], G-quadruplex formation [25-28], B-Z form DNA transitions[29], and much more. AFM imaging and 2D DNA nanostructures have also been used for biosensing applications - in this case, the identity of bound species visualized under AFM can be determined either through the introduction of indexing elements such as DNA dumbbells[30] or through the use of asymmetric DNA structures[31].

3D DNA origami structures with specific form/function relationships have also been designed, often times with some form of dynamic elements. Shih and Bellot *et al.* created a trapezoidal “nanoactuator” in which the incorporation of additional DNA oligonucleotides could force the trapezoid into either “closed” or “open” conformations[32]. As an example of how this conformational transition could be used, the authors conjugated two halves of a split Enhanced Green Fluorescent Protein (EGFP) to either side of the nanoactuator in order to regulate the distance between the EGFP halves - increased fluorescence was only observed in the closed conformation. Kuzuya et al constructed a reconfigurable "plier"-like DNA origami structure, which facilitated the detection of solution-phase binding events through binding-induced switching in the plier conformation [33, 34]. Carlos Castro's group has developed numerous dynamic DNA origami elements designed to behave like macro-scale mechanical implements, including sliding and rotational joints, which can be combined to create more complex motion [35]. These devices have been used to monitor things like nucleosome stability[36] and depletion forces [37].

2.1.1.2 Nanofabrication with Synthetic Nanoparticle Heteroelements

A wide variety of nanomaterials can interface with DNA using a range of conjugation techniques, which have been well summarized in a previous review[38]. By far the most common material used for nanofabrication with DNA origami is gold. Gold nanoparticles (AuNPs) and nanorods (AuNRs) have very interesting optical properties that can be modulated through inter-particle interactions. Furthermore, AuNPs can be easily incorporated into DNA nanostructures using the facile conjugation of thiolated-oligonucleotides with the gold surface. There are a vast number of examples in the literature of nanofabrication using AuNPs, but only a few representative studies will be highlighted here. Recent work by Oleg Gang's group have demonstrated the ability for DNA origami nanostructures to program the fabrication of well-defined two-dimensional networks of AuNPs[39]. The authors used a cross-shaped origami tile with a hole in the center for capturing a single AuNP. The four edges of the tile were modified with unique ssDNA extensions to allow for a wide range of anisotropic and specific connections between different tiles in a lock-and-key mechanism. The authors used this system to fabricate well-defined AuNP clusters and chains, as well as large 2D arrays. The same group has also used three-dimensional polyhedral DNA origami nanostructures to construct well-defined 3D AuNP crystal structures [40, 41]. Other groups have explored similar gold nanoparticle arrays, including the use of hexagonal tiles[42] and "nano-flowers"[43] to construct linear chains as well as hexagonal and square lattices.

The prevailing rationale for using DNA nanostructures to organize AuNPs is the ability to use interactions between the nanoparticles as a means of manipulating light. This was elegantly demonstrated by Liedl *et al.*, who used a 24-helix bundle DNA origami rod

to pattern the self-assembly of AuNPs into helices with either a right-handed or left-handed pitch [44]. These nanostructures exhibit pronounced circular dichroism effects in the visible range of the electromagnetic spectrum that change based on the helicity of the organized AuNPs. Subsequent work by the same group demonstrated switchable circular dichroism using a similar DNA origami rod-based architecture, where the orientation of the superstructure in reference to incident light could be controlled[45]. Other groups have similarly used DNA origami to control the plasmonic behavior of AuNRs, including a AuNR capable of walking along a DNA origami track[46], stacked-arrangements of offset AuNRs [47], chiral AuNP rings [48], and the fabrication of static [49] and dynamic [50] AuNR dimers.

The fabrication of devices where AuNPs interact with other optically active materials has also been accomplished using DNA origami. In their pioneering work, Tinnefeld *et al.* demonstrated that a zepto-liter electromagnetic "hot spot" could be constructed by organizing 100 nm AuNP dimers on a 12-helix bundle DNA origami pillar[51]. When the authors placed a fluorescent dye in the gap between the AuNPs, they demonstrated fluorescence enhancements of up to 117-fold. By using this system, the authors were able to monitor DNA hybridization and Holliday Junction conformational dynamics at the single-molecule level. Similar studies have been conducted by other groups, including distance-dependent quenching/enhancement effects of fluorescent dye-gold nanoparticle systems on a triangular DNA origami tile[52] as well as "nano-antennas" for hot spot-induced enhancement of surface-enhanced Raman spectroscopy[53]. AuNP/quantum dot heteroelement devices have also been constructed to study the distance-dependent fluorescence quenching between the two elements[54]. Similar work

from the Liedl group investigated the fluorescence life-time of quantum dot-AuNP pairs on a DNA origami frame[55].

2.1.1.3 Nanofabrication with Biological Heteroelements

In biology, the spatial arrangement of proteins into large supra-molecular complexes leads to enhanced activity or new functionality, particularly in regard to multi-enzyme pathways. The ability to mimic these complexes through nanofabrication with DNA origami is a useful tool to better understand native multi-protein systems, as well as to construct more efficient enzymatic nanoreactors for technical applications. While simpler DNA nanostructures had been previously used to assemble multi-enzyme systems, Yan *et al.* were the first to use DNA origami to scaffold a more complex, three-protein system[56]. Using a two-dimensional rectangular DNA origami tile, the authors were able to investigate the effects of protein distance on a glucose oxidase/horseradish peroxidase bi-enzymatic process. The authors found that if a non-enzymatic "bridge" protein was placed in between the two enzymes the reaction rate could be increased even further. The authors attributed this effect to the more effective "shuttling" of reaction intermediates between the hydration shells of the two enzymes. Subsequent studies by the same group increased the complexity of the design, utilizing a flexible ssDNA linker modified with cofactor NAD+ to control the preference for two competing enzymatic reactions[57]. Three-dimensional DNA origami nanostructures have also been used to modulate and study enzymatic behavior, including the use of a "nanocage" to encapsulate multiple enzymes to improve reaction efficiency[58].

DNA origami nanostructures have also been used to control and study non-enzymatic proteins. Shih and Reck-Peterson *et al.* used a 12-helix bundle DNA origami tube as a platform for organizing the motor proteins kinesin and dynein[59]. Using single-molecule fluorescence techniques to track the DNA nanostructure, the authors were able to study the interplay between motor proteins with opposite-polarity movement. Hogberg and Teixeira *et al.* also used a tubular DNA origami structure to pattern proteins, focusing on understanding how the spatial organization of ligands affects receptor-mediated cell responses[60]. By controlling the distance between two Ephrin-A2 molecules, the authors were able to show how ligand placement alters receptor EphA2 phosphorylation and subsequent cell invasion.

2.2 Magnetic Resonance Imaging and Iron Oxide Nanoparticles

2.2.1 Magnetic Resonance Imaging

Magnetic resonance imaging (MRI) was developed in 1973 and 1974 by Paul Lauterber and Peter Mansfield, based on the principle of nuclear magnetic resonance (NMR) [61, 62]. Since that time, MRI machines have become a staple in clinics around the world and are an essential part of modern healthcare as a means of studying and diagnosing a wide variety of injuries and pathologies. MRI has numerous advantages which make it well suited as a clinical diagnostic imaging technique – it uses non-ionizing radiation (unlike x-ray and CT imaging), so it is considered safer than other imaging modalities; it has a large depth of penetration, allowing the visualization of structures and organs deep within the body; contrast arises due to variations in the chemical environment of hydrogen protons (water) and thus all tissues in the body contribute to the signal, enabling the

visualization of soft organs such as the brain, muscles, liver, etc. Relative to other imaging techniques, MRI has relatively high spatial resolution, though relatively poor temporal resolution.

MRI works on the principles of nuclear magnetic resonance and is a method by which NMR signals can be obtained throughout the body and then reconstructed into two-dimensional (2D) and three-dimensional (3D) images. Protons have a spin angular momentum, and as charged particles, thus have a magnetic moment. In the presence of an external magnetic field, such as that provided by the magnetic in an MRI scanner, the magnetic moments of protons align with the magnetic field and precess around this axis at the Larmor frequency, which can be described by the following equation, where ω is the Larmor frequency, γ is the gyromagnetic ratio, and B_0 is the strength of the external static magnetic field:

$$\omega = \gamma B_0$$

This frequency is unique to nuclei of different atoms, and thus can be used to isolate individual elements – while other atoms can contribute to NMR signals, MRI predominately focuses on imaging H^1 protons due to their abundant prevalence in the body. The equilibrium of all hydrogen protons aligning with and precessing about the external magnetic field can then be disturbed through the application of a radio-frequency (RF) pulse. Photons of the appropriate energy are absorbed by the protons, and this energy rotates the magnetic moments of protons away from the longitudinal axis set by the external magnetic field, producing both longitudinal and transverse components of the magnetic moment. Upon removal of the pulse, the spins relax back to equilibrium through two

different mechanisms: spin-spin and spin-lattice relaxation. Spin-spin relaxation, also known as T_2 relaxation, leads to the loss of the transverse component of the magnetization vector. In this case, all the individual protons within a region experience slightly different external magnetic fields due to the different chemical environments, and thus precess at slightly different frequencies. This leads to a loss of phase coherence (dephasing) and a concomitant decrease the net transverse magnetization vector. This relaxation process is described by the following equation, where M_{TR} is the transverse magnetization vector, $M_0\sin(\alpha)$ is the magnetization vector in the transverse plane immediately following a RF pulse, and T2 is a characteristic time constant which describes the signal decay:

$$M_{TR}(t) = M_0 \sin(\alpha) e^{(-t/T2)}$$

Spin-lattice relaxation, or T_1 relaxation, is the phenomenon that leads to the recovery of the longitudinal component of the magnetization vector. In this case, interactions of protons with the neighboring environment (lattice) leads to a transfer of energy in the form of heat. This allows the protons to return to their lowest energy state, which is aligned with the external magnetic field (maximal longitudinal component, zero transverse component). This process is defined by the following equation, where M_l is the longitudinal component of the magnetization vector, M_0 is the equilibrium magnetization vector, and T1 is a characteristic time constant which describes the signal decay:

$$M_l(t) = M_0(1 - e^{\left(-\frac{t}{T1}\right)})$$

Contrast between different tissues arises from differences in the values of T_1 and T_2. For example, cerebral spinal fluid (CSF) has $T_1 \sim 3000$ms and $T_2 \sim 2000$ms, while fat

has T_1 ~ 200ms and T_2 ~100ms. Thus, at any given time t, the transverse magnetization vector will differ depending on the type of tissue, and the magnitude of this vector is converted into pixel brightness when rendering the final image (Figure 2-2). Further details about MRI, such as RF pulse sequences used to generate different forms of contrast and spatial encoding through the use of magnetic field gradients, are outside the scope of this thesis, but can be found elsewhere[63].

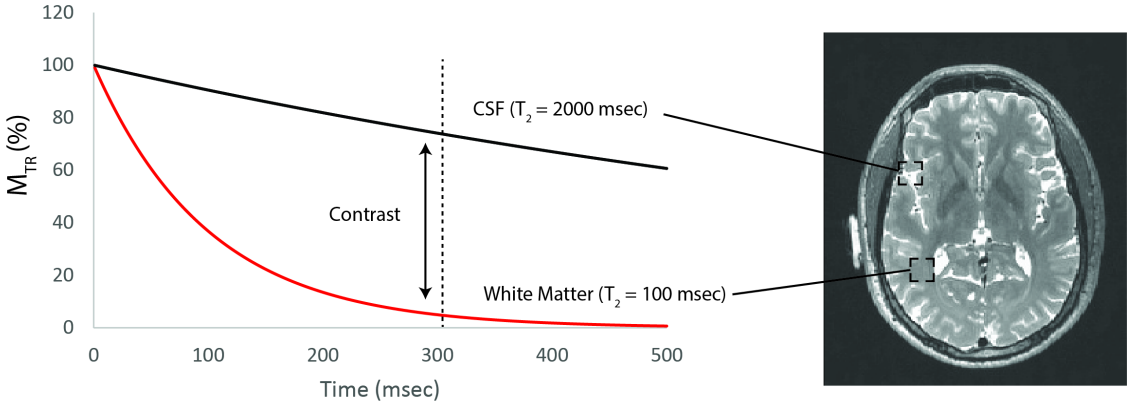

Figure 2-2. Mechanism of MRI Contrast Generation. Contrast in MRI images is due to differences in the relaxation rate of water protons within tissue. For T2 imaging parameters, tissues which have shorter T2 values have signals which decay more rapidly, appearing as darker regions within an MR image.

2.2.2 Contrast Enhanced MRI and Molecular Imaging

While MRI is incredibly useful for the visualization of numerous tissues and the diagnosis of numerous pathologies, the mechanism of contrast generation oftentimes makes it difficult to distinguish between regions with relatively similar chemical compositions/magnetic properties. This is perhaps most pronounced in the case of solid tumors located within other tissues, such as in liver cancer. In this case, the tumor tissue is often similar enough to healthy liver tissue that the tumor is indistinguishable on MRI images. Additionally, MRI primary provides structural information about anatomy within the body and offers no insight into physiologic function or cellular/molecular characteristics (complex MRI pulse sequences and data analysis do allow for some limited functional information based on dynamic changes in MRI signal). Due to this limitation, scientists have developed MRI contrast agents, which are exogenous agents introduced into the body that alter the MRI signal in their vicinity and thus produce "artificial" contrast on MRI images wherever they are located. In this manner, contrast-enhanced MRI can be used to visualize and identify new physiologic or pathologic characteristics based on interactions between these features and the contrast agents. Through careful design and engineering of these contrast agents, information about cellular and molecular processes within the body can be gleaned. For example, by engineering contrast agents to bind to specific proteins within the body through recognition elements such as antibodies, aptamers, or receptor ligands the presence of these specific proteins can be identified. Similarly, it can be possible to engineer dynamic elements into contrast agents, such that their ability to modulate MRI contrast can be altered. If this dynamic element is tied to some cellular process, such as enzymatic activity, the change in contrast induced by changes in contrast

agent can be used to identify the presence of said process. This type of imaging has come to be known as molecular imaging, due to the ability to analyze molecular characteristics within the body[64].

Two different classes of MRI contrast agents exist, based on the method in which they alter the relaxation of the magnetic vectors. The first class of agents as known as T_1 agents and serve to decrease T_1 of water protons in their vicinity through a mechanism described by inner-sphere theory. These agents lead to a more rapid increase in the longitudinal magnetization component and produce hyper-intense, brighter images (positive contrast) under T_1 imaging parameters. The most well-known and widely used T_1 contrast agents are chelates of the paramagnetic ion gadolinium. The second class of agents, and those of interest for this work, is known as T_2 agents. These species serve to decrease the T2 of water protons in their vicinity through a mechanism described by outer-sphere theory, leading to enhanced dephasing of the transverse components of magnetic moments and creating hypo-intense, dark regions (negative contrast) under T_2 imaging parameters. Based on outer-sphere theory, water molecules which diffuse into regions near the MRI contrast agent experience a slightly different magnetic field due to the magnetic moment of the contrast agent. This field inhomogeneity causes these protons to spin at different frequencies, leading to accelerated dephasing, a loss of coherence, and a shortening of T_2. Thus, at any given time the transverse magnetization of voxels with a T_2 contrast agent will be lower and the intensity of the signal measured on the MRI will be lower. The efficacy of T_2 contrast agents is typically quantified using the T_2 relaxivity, or r_2, which corresponds to increases in the rate of T_2 shortening per unit concentration of the nanoparticles (typically expressed in units of s^{-1} mM $iron^{-1}$). Contrast agents with a higher

r_2 are more effective at shortening T_2, producing greater contrast enhancement at lower doses. Most T_2 contrast agents are magnetic nanoparticles, and their ability to alter T_2 is expressed by the following equation, where b is a constant that depends on the nature of the nanoparticle and the diffusion coefficient, C_x is the concentration of the particles, R_{NMR} is the minimal distance of approach (effective nanoparticle radius), and M_{NMR}^{SAT} is the saturation magnetization of the nanoparticles:

$$R_2 = \frac{1}{T_2} = bC_x {R_{NMR}}^2 {M_{NMR}^{SAT}}^2$$

Thus, the relaxivity quadratically increases with respect to nanoparticle radius and nanoparticle magnetization[65]. As either the size or the magnetization increases, the effective volume at which the particles create magnetic field in-homogeneities increases and thus more substantial dephasing of a larger number of water protons occurs. This equation is only valid when the following equation is satisfied, where γ is the proton gyromagnetic ratio, B_{Eq} is the magnetic field of the contrast agent, and τ_D is the diffusion correlation time ($\tau_D = \frac{{R_{NMR}}^2}{D}$):[66]

$$\gamma B_{Eq} \tau_D < 1$$

This is typically true if the echo time used for measuring the NMR signal is larger than τ_D. As the nanoparticle size grows larger, the amount of time protons spend in its vicinity increases to the point where they no longer experience magnetic field in-homogeneities in the time scale of the measurement. In this case, known as the static dephasing region (SDR), r_2 is no longer dependent on nanoparticle radius and has reached it maximum theoretical value for a fixed concentration and magnetic saturation[66]. At this

point, further increases in particle radius actually serve to decrease r_2 due to a refocusing effect of the spin echo pulse sequences [65]. Based on experimental data and theoretical simulations, MRI contract enhancement efficiency can be predicted accurately by simply knowing the size and magnetic saturation of the magnetic nanoparticle contrast agents[67].

2.2.3 Iron Oxide Nanoparticles as MRI Contrast Agents

Of the relevant T_2 MRI contrast agents, superparamagnetic iron oxide nanoparticles (IONPs) are the most common[68]. IONPs are magnetic single-domain nanocrystals, typically composed of either magnetite (Fe_3O_4) or maghemite (γ-Fe_2O_3), which exhibit superparamagnetic behavior. Superparamagnetism is a magnetic phenomenon observed at the nanoscale; it is a state in which sufficiently small ferromagnetic/ferrimagnetic materials exhibit negligible net room-temperature magnetization in the absence of an external magnetic field (comparable to paramagnetic materials) while maintaining a high magnetic susceptibility (comparable to the bulk ferromagnetic/ferrimagnetic material) (Figure 2-3). As such, superparamagnetic particles exhibit strong magnetization in the presence of an external field, without remnant magnetization when the field is removed. This behavior ensures that colloidal superparamagnetic particles remain stable in solution without spontaneous aggregation, while also exhibiting pronounced magnetic effects when "activated" by an external field.

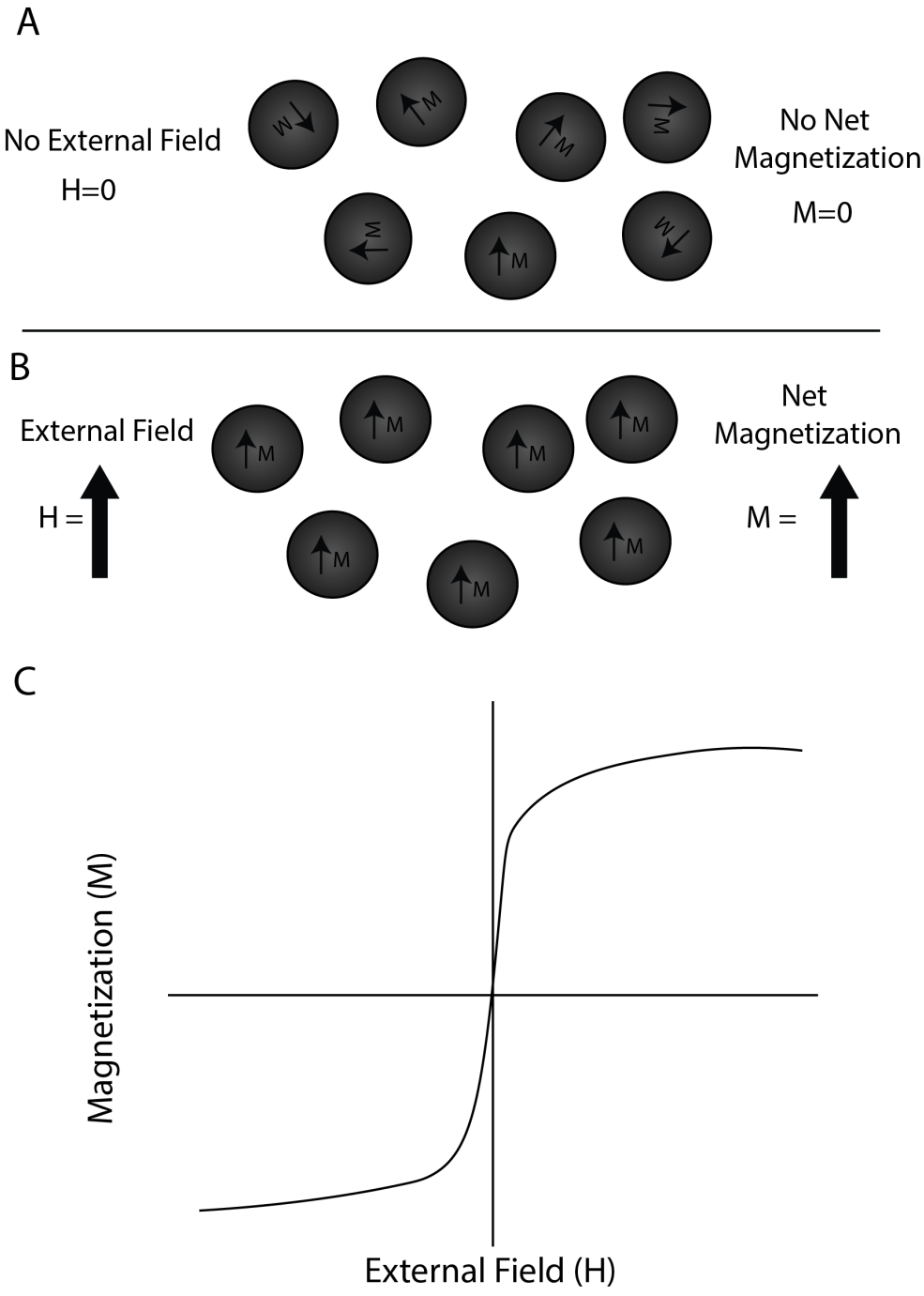

Figure 2-3: Superparamagnetism. A) Particles in the superparamagnetic regime have magnetic moments which rapidly change due to Brownian and Néelian relaxation mechanisms, such that there is no net magnetization (M) in the absence of an external field (H). B) In the presence of an external field, the magnetic moments of each particle lock in place, producing a net magnetization. C) H/M curve showing magnetization only in the presence of external fields with no remnant magnetization.

IONPs have generated considerable interest in the nanomedicine field, due to their unique magnetic behavior, biocompatibility, and relative ease of synthesis[69]. IONPs have seen extensive use as MRI contrast agents[70, 71], but also have been leveraged to produce magnetically-guided drug delivery vehicles, hyperthermia agents, vectors for bioseparation processes, carriers for gene transfection, and other application[72-78]. In particular, the MRI contrast enhancement and drug-delivery capabilities have positioned IONPs as dual diagnostic/therapeutic (theranostic) agents[79-81].

The two IONP-based contrast agents approved for clinical use, Ferridex and Resovist, have r_2 values around 98 $mM^{-1}s^{-1}$ and 150 $mM^{-1}s^{-1}$, respectively[70]. There has been considerable effort in the field to fabricate magnetic nanoparticles with higher r_2 values that can function as improved contrast agents. One technique to accomplish this has been the synthesis of IONPs with larger magnetic moments. Synthetic strategies such as thermal decomposition have been used to produce iron oxide nanocrystals with larger sizes, more uniform crystallinity, and better control over composition. Contrast agents with r_2 values as high as 760 $mM^{-1}s^{-1}$ have been created through precise control over iron oxide nanocrystal synthesis[82], though IONPs of this quality are challenging to synthesize.

2.2.3.1 Assembly of Iron Oxide Nanoparticles to Enhance T_2 Relaxivity

Another technique for increasing r_2 has been through the controlled clustering of individual IONPs, as assemblies of these particles behave as larger magnetic spheres with a larger capacity to influence proton relaxation[83, 84]. IONP clustering is traditionally accomplished through the use of amphiphilic polymers, which stabilize aggregates of hydrocarbon-modified IONPs in a hydrophobic core. A wide variety of block copolymers

have been used in this regard, including poly(trimethylammonium ethylacrylate methyl sulfate)-b-poly(acrylamide) (PTEA-b-PAM)[85], poly(ethylene imine)-b-poly(ε-caprolactone)-b-poly(ethylene glycol) (PEI-b-PCL-b-PEG)[86], and poly(ethylene oxide-b-d,l-lactide) (PEO-b-PL)[87], among others. Other techniques, such as encapsulation in a silica matrix[88] and lipoprotein micelles[89] have also been used.

In addition to their use as MRI contrast agents, IONPs have seen recent development as sensing elements for *in vitro* diagnostic assays or *in vivo* dynamic molecular imaging contrast agents. One technique was developed in 2002 by Ralph Weissleder's lab, in which changes in the T_2 signal of water in a sample due to IONP interactions were monitored using nuclear magnetic resonance (NMR). Aggregation of the particles led to increases in r_2 and subsequent decreases in T_2 of the sample[86, 90]. This type of sensor was termed a magnetic relaxation switch (MRSw). The stimuli-responsive behavior was introduced through chemical functionalization of the IONP surface with various sensing elements, such as DNA, antibodies, and peptides. Work by Weissleder group and others to diversify functionalization with sensing elements have led to sensors capable of detecting viruses[91], monitoring enzyme activity[92-96] and calcium levels[97, 98], identifying enantiomeric impurities[99], and measuring small-molecule analytes such as glucose[100], hormones[101] and antibiotics[102]. As T_2 changes can be monitored using MRI, similar sensors have also been used for *in vivo* detection [103, 104].

Several mechanistic and theoretical studies have been used to elucidate the mechanism behind the r_2 enhancement following IONP assembly. Theoretical experiments utilizing analytical analysis[83] and computational models such as Monte Carlo simulations have been used to predict changes in T_2 with IONP clusters in a range of sizes

[66, 84, 105]. These studies have found that R_2 values increase with increasing cluster size, which is consistent with the experimental evidence. In these cases, the proposed mechanism is based on the increased effective radius of the magnetic particle, leading to an increased time that individual water molecules spend within the magnetic field and thus increased spin dephasing. In particular, these theoretical studies enable the prediction of how precise changes in the nature of the IONP clusters can affect r_2 enhancement. Brown et al found that R_2 scales with an increase in the number of particles following a power law relationship, and that the specific scaling factor is dependent on the spatial organization of particles within the cluster (fractal dimensions)[66, 105]. The shape of IONP clusters was also investigated by Vuong et al, who found that spherical and shell organization strategies produced higher R_2 enhancements compared to linear assemblies[66]. For linear and 2-particle IONP assemblies, interparticle distance also plays a role in R_2 enhancement, with increasing particle spacing leading to decreased R_2 enhancement[66, 84].

Experimental studies into the mechanisms of r_2 enhancement have also been conducted. Researchers in the Weissleder group conducted several detailed mechanistic studies on their magnetic resonance switch system, using a variety of different IONP core constructs (including manganese ferrite particles and iron core-manganese ferrite shell particles) with different sizes[106]. They found that R_2 enhancement began to level off, consistent with moving from the motional averaging regime to the static dephasing regime. However, a subsequent decrease in r_2 at large cluster sizes for the highest M_s magnetic particles pointed to potential decreases in the effective magnetization of the clusters at larger sizes. These differences were attributed to the fractal assembly of the particles within each cluster. Similar results were also obtained in work by Poselt et al [86]. Other work

by Hak et al decoupled particle size from iron concentration by synthesizing oil-emulsion droplets of uniform size which would be loaded with varying amounts of IONPs[107]. They found that both IONP concentration and droplet size had effects on r_2 enhancement, and that the quantitative values fell somewhere between that predicted by motion averaging regime models and static dephasing regime models. They also hypothesize that water molecules trapped in the coating of IONPs could contribute to the r_2 enhancement in ways not adequately described by the theoretical models used. Other work has shown that reduced magnetic field symmetry contributes to enhanced inhomogeneity and thus enhanced r_2 was observed using different-sized IONPs included in the same polymer emulsion[108]. By varying the molecular weight of the polymer, the researchers were also able to establish that increased distance between IONPs led to a small decrease in r_2, which is consistent with simulations. Relative changes in the number of IONPs in clusters was controlled by attaching streptavidin-coated IONPs to biotinylated Zinc-finger proteins attached to a linear dsDNA template - attaching ~11 IONPs together led to a small r_2 enhancement of ~10%[109].

2.3 Molecular Motors and DNA Walkers

Directed motion at the molecular level plays a critical role in a wide variety of biological functions, including intracellular transport and mitosis[110-112]. This includes protein molecules which walk along tracks, from the kinesin, dynein, and myosin families. These molecular walkers contain “feet” which interact with a track, allowing the walker to stay attached to the track while also providing a mechanism for motion. There has been considerable interest in developing synthetic motors inspired by these biological machines for use as model systems for studying natural processes as

well as for technical applications, such as biosensing, molecular computing, etc.[113, 114]. There are several different characteristics which define molecular walkers. The first of these is *processivity*; that is, the ability of the walker to stay attached to the track and to continue motion along this track over multiple cycles. Other parameters include *directionality* (preferential movement towards one side of the track), *repetition* (repeated steps of the motor cycle to enable processive walking), *progressive operation* (the ability of the walker to reset to an original state after each motor cycle), and *autonomy* (ability to continually operate without external interactions as long as fuel is present). While molecular machines must have 4 of these 5 characteristics to be classified as a walker, autonomy is a characteristic which can be desirable but not necessary.

2.3.1 Biological Molecular Motors

The protein molecular walkers move along tracks made of cytoskeletal filaments, namely microtubules and actin, and are all ATPases – they convert chemical energy generated by the hydrolysis of adenosine triphosphate (ATP) into adenosine diphosphate (ADP) into mechanical work. In this case, chemical energy from ATP leads to a conformational change in the catalytic motor domain of the protein, driving long range (up to 25nm) translation movement[110]. There are over 80 different isoforms within the three class of these motor proteins; while these motor protein families share many similarities, particularly in regard to the use of ATP as a fuel source, the exact nature of their behavior can vary. For example, Myosin-V is a processive motor protein which moves along actin filaments through the coordinated motion of 2 "feet", enabling the protein to remain bound to the track at all times[115]. In comparison, the related Myosin-II has only one foot that interacts with actin filaments and thus is not a processive motor

(though this behavior is critically important for its role in force generation in muscles) [116]. Meanwhile, the kinesin protein KIFIA is a processive motor that only uses one foot, maintaining adherence to the track through numerous secondary interactions that enable a motion more akin to sliding than walking[117]. One of the most studied motor proteins is Kinesin-I, a homodimeric protein with high processivity (~1mm run lengths) and directionality enabled by the coordinated out-of-phase movement of two identical feet and a slight energetic bias towards forward diffusional "searching" of the next binding step[118].

2.3.2 Mechanisms of Molecular Motors

The study of natural motor proteins has led to numerous insights into the molecular mechanisms for generating both *processivity* and *directionality*[114]. In order for a motor to be processive, at least one component of the motor must be attached to the track at all times. This can be accomplished in several different ways: either through the use of two different feet with mutually-exclusive conditions/fuel for unbinding, or through the use of an asymmetric track which differentiates the rate at which two identical feet bind and unbind (as Kinesin-I). Processive motors with one foot are also possible as long as secondary interactions between motor and track keep the motor attached during foot unbinding (as KIFIA). More than 2 feet would also allow for highly processive movement, though there are no biological motors which act in this manner.

For *directionality* to exist, there needs to be some energy state difference between subsequent steps in order to bias movement in one particular direction. One method in which this can occur is known as the Brownian ratchet method, which requires an energy

input (ATP for biological motors, though other energy types are possible), a randomization agent (typically thermal fluctuations), and an asymmetric energy potential in the direction of motion[119, 120]. There are several different mechanisms by which these Brownian ratchets can be constructed. One version is a 'burned-bridge' ratchet, in which walker motion consumes footholds it had previously been bound to, thus eliminating the possibility for backward motion. In a walker with two different feet, directionality can be imparted by incorporating a switchable element into either the motor or the track which manipulates the potential energy landscape. Finally, a walker with two different feet which includes one irreversible step can create directed motion through kinetic control.

2.3.3 Synthetic Molecular Motors: DNA Walkers

Of the various types of synthetic motors that have been created, DNA walkers are some of the most studied – the precise programmability of DNA makes it an excellent material for constructing nanoscale machines. The first realization of a synthetic DNA walker came in 2004 in a report by Sherman and Seeman [121]. This non-autonomous motor consisted of a triple-crossover DNA tile as a track, with 3 unique single-stranded footholds extending from the surface. The DNA walker consisted of two dsDNA 'legs' attached to 2 ssDNA 'feet', with the legs attached by flexible ssDNA linkers. The feet were attached to the track foothold via hybridization with sacrificial anchor strands, which contain regions complementary to both the foot and the track. Addition of a fuel strand led to the removal of the anchoring strand via strand displacement, allowing the freed foot to hybridize to the next foothold on the track following the addition of the subsequent anchor strand. This simple walker satisfies the

four main criteria - it is processive (remains bound to the track through at least one anchoring strand at any given time), repetitive, progressive, and exhibits directionality through the sequential addition of new anchoring strands. In this instance, the energy required for movement comes from the free-energy gain associated with anchor/toe-hold/fuel strand hybridization. Shin and Pierce reported a very similar system, utilizing a single DNA duplex with extended toe-holds as the track and a motor consisting of a single dsDNA region along with 2 ssDNA feet[122]. In this instance, the walker moves in a 'hand-over-hand' motion where the leading foot switches at each step, in comparison to the 'inch-worm' movement of the previous walker. More complex non-autonomous motors have also been developed, including a 4-footed triangular DNA walker capable of moving across a 2D DNA origami track and picking up/delivering DNA-modified gold nanoparticles[123].

Outside of these non-autonomous DNA walkers, there have been numerous reported studies of autonomous DNA walkers using a variety of mechanisms to induce movement. Two studies utilized a burnt-bridge brownian ratchet mechanism to facilitate walking of a ssDNA motor[124, 125]. In this case, enzymatic activity at motor/foothold duplexes provides the energy source for movement. Cleavage of the foothold strand frees a ssDNA region of the walker to hybridize to a neighboring foothold via a strand displacement mechanism, while the consumption of old footholds facilitates directional movement. In one case, a restriction enzyme was used to cleave a recognition site in the walker/foot-hold duplex, while the other introduced a DNAzyme directly into the walking strand. The first enzyme-free autonomous DNA walker was introduced in 2008, involving a single-stranded DNA track consisting of overlapping binding regions

(footholds) and a single duplex with two ssDNA feet[126]. Toe-hold mediated binding to a meta-stable DNA hairpin H1 in solution leads to the unbinding of a single foot and then subsequent freeing of the foot through binding to another hairpin H2. In this instance, directionality is enabled due to steric hindrance effects which makes it energetically favorable for movement to occur in one direction. A similar enzyme-free autonomous walker was subsequently reported involving the movement of a DNA walker consisting of 2 different feet which are displaced from the track via signaling strand/hairpin interactions[127]. Hybridization of the free foot to a new foothold reveals a second signaling strand, allowing the process to repeat. Revealing signaling strands in this manner ensures that one foot is bound at any given time (processivity) while directionality is ensured due to blocking of previous foot-holds by the hairpin fuel (burnt bridge ratchet).

Autonomous DNA walkers with more than 2 feet have also been constructed, including a 'molecular spider' consisting of three DNAzyme legs attached to a streptavidin protein core which can move along a 2D DNA origami track[128]. An increase in the number of feet enhances the processivity of the motor. Careful design of these footholds on the 2D tile enabled the incorporation of turn and stop commands. Another study created a molecular walker consisting of up to 6 catalytic legs through the use of dimerized streptavidin cores, which could walk through a DNA-coated dextran matrix[129]. In an extreme case, Salaita et al developed a rolling DNA motor consisting of a DNA-functionalized microparticle moving along an RNA-coated surface using RNase H activity to drive movement in a burned-bridge ratchet movement[130]. These highly polyvalent motors make thousands of connections to the track at any given

time. However, the unique rolling behavior enables high speed movement by limiting unproductive sampling interactions. In the other direction, monopodal DNA walkers have also been developed, using various designs such as "cleat" domains to ensure processivity through constant attachment to the track[131].

2.3.3.1 Applications of DNA Walkers

Beyond their functions as models used to better understand mechanisms of directed motion at the molecular scale, DNA walkers have also been developed with practical applications in mind, including bioanalysis[132] and molecular computing. One-dimensional DNA walkers have been used to detect the presence of target mRNA sequences through the transport of cargo molecules to enhance an electrochemiluminesence signal[133, 134]. One common theme is the use of DNA walkers as a signal-amplification strategy to increase sensitivity - a target molecule intitiates movement of a DNA walker which can then catalytically process a large number of signal molecules. This strategy is most applicable for walkers which can traverse as 2D surface, as this offers a larger pool of signaling molecules to be triggered. Walkers which sequentially remove quencher-labeled strands and thus increase fluoresence have been developed[135], as well as walkers which remove redox labels from an electrode to modify the electochemical signal[136]. Finally, walkers which traverse 3D surfaces, typically DNA-modified particles, have been used for the detection of both nucleic acids[137, 138] and proteins[139, 140], as well as for cellular imaging applications[141, 142]. Beyond sensing applications, DNA walkers have been used deliver cargo molecules, either over long distances [143] or to sort molecules into specific locations[144].

CHAPTER 3. CONTROL OF IRON OXIDE NANOPARTICLE CLUSTERING USING DUAL SOLVENT EXCHANGE

3.1 Abstract

Superparamagnetic iron oxide nanoparticles (IONPs) have demonstrated considerable promise for magnetic resonance contrast, drug/gene delivery, and hyperthermia applications. In recent years, it has been shown that controlling the self-assembly of SPIOs into larger superstructures can have a significant impact on the magnetic properties that dictate the functionality of the particles for biomedical applications. In this work, we developed a novel method for controlling the clustering of two different SPIO core sizes (8 nm and 15 nm) by varying the amount of amphiphilic coating molecule used during the dual-solvent exchange coating process. We show that hydrodynamic size and T_2 relaxivity can be increased using this method, while the specific absorption rate is decreased. These results highlight a new, simple method for triggering the self-assembly of SPIOs using commercially available materials. This approach can be used to generate nanoparticles with high relaxivity, promising for contrast-enhanced magnetic resonance imaging

3.2 Introduction

This section contains text and data that have been reported in a previous publication (© 2015 IEEE, reprinted, with permission, from reference [145])

Superparamagnetic iron oxide nanoparticles (IONPs) have received significant attention in the past two decades as potential drug/gene delivery vehicles, MRI contrast

agents, and magnetic hyperthermia mediators due to their unique magnetic properties, high biocompatibility, and ease of synthesis[69]. Considerable efforts have been made to produce high-quality IONPs with improved magnetic properties – notably high T_2 relaxivity for MRI contrast and high specific absorption rate (SAR) for magnetic fluid hyperthermia, both important in developing IONPs for a broad range of biomedical applications[146].

In addition to improving the quality of synthesis for individual IONPs, recent work has demonstrated that controlling the self-assembly of nanoparticles can have a significant impact on magnetic properties, including T_2 relaxivity and SAR [147, 148]. By controlling the size and shape of the final nanoparticle assemblies, T_2 relaxivity and SAR can be altered to match the intended application. However, the majority of the techniques used to facilitate self-assembly utilize non-biocompatible materials, are technically challenging, and/or require complicated synthesis of di-block or tri-block copolymers.

In this work, we demonstrate a new, simple method to control clustering of IONPs using commercially available, biocompatible materials through the dual-solvent exchange coating method[149]. This technique involves the gradual increase of the environment polarity through a two-step solvent exchange process, which drives the micellization of an amphiphilic molecule, typically a phospholipid-poly(ethylene glycol) (PEG) conjugate, onto the surface of the hydrocarbon-stabilized iron oxide cores through hydrophobic interactions. By controlling the ratio of amphiphilic molecules to iron oxide cores during the coating process, we show that clustering of the nanoparticles can be induced, leading to colloidally-stable nanoparticles with a range of hydrodynamic diameters. We then characterized the T_2 relaxivity and SAR of the clustered IONPs, demonstrating the ability

to modulate these parameters post-nanoparticle synthesis. This work demonstrates a novel, simple method for controlling the self-assembly of individual IONPs into larger nanoparticles that show promise as high-sensitivity MRI contrast agents.

3.3 Materials and Methods

Iron acetylacetonate ($Fe(acac)_3$, 99%), 1,2-hexadecanediol (technical grade, 90%), oleic acid (technical grade, 90%), and oleylamine (technical grade, 70%), toluene (>99.9%), chloroform (99%), dimethyl sulfoxide (DMSO 99%) benzyl ether (98%), hydrochloric acid, hydroxylamine HCl, sodium hydroxide, ammonium acetate, and ferrozine were purchased from Sigma-Aldrich and used as received; 1,2- distearoyl-sn-glycero-3-phosphoethanolamine-N-[methoxy(polyethylene glycol)- 5000] (DSPE-PEG 5000) was purchased from Avanti Polar Lipids.

3.3.1.1 Iron oxide nanoparticle synthesis

Iron oxide nanoparticle cores of 8 nm diameter were synthesized by an adapted published procedure[150]. Iron acetylacetonate (6 mmol), 1,2-hexadecanediol (30 mmol), oleic acid (18 mmol), and oleylamine (18 mmol) were mixed in benzyl ether (60 ml) in a 500 ml flask under magnetic stirring. After 40 minutes of incubation under vacuum to remove excess oxygen, the solution was raised to 120°C and left for 40 minutes to remove excess water vapor. Then the vacuum was removed and replaced by nitrogen flow, and the temperature was raised to 200°C and held for 2 hours before ramping to 300°C and holding for 1 hour. The mixture was then allowed to cool to room temperature and was purified via three repeated rounds of centrifugation using ethanol (240 ml) induced precipitation, followed my resuspension in toluene. 15 nm particles were obtained using an iterated seed-

mediated growth process[150]. Briefly, iron oxide nanoparticle seeds are mixed with an amount of iron acetylacetonate based on the necessary mass to increase diameter of iron oxide cores by ~2 nm. Oleic acid and oleylamine are added at a 3:1 molar ratio to the iron acetylacetonate amount and 1,2-hexadecanediol is added at a 5:1 molar ratio to the iron acetylacetonate. Benzyl ether is then added to obtain a final iron acetylacetonate concentration of 20 mg/ml. The heating and purification steps were repeated exactly as before for the synthesis of the original seeds.

3.3.1.2 IONP- DSPE-PEG Coating

To render the as-synthesized iron oxide cores water soluble, the dual solvent exchange coating method was utilized. Briefly, 200 μL of iron oxide cores (5 mg Fe/mL in toluene) was added to 800 uL of chloroform with differing amounts of 1,2-distearoyl-*sn*-glycero-3-phosphoethanolamine-N-[methoxy(polyethylene glycol)-2000] (DSPE-PEG), ranging from 0.5 mg (0.5:1 w/w DSPE-PEG:Fe coating ratio) to 4 mg (4:1 coating ratio). 4 mL of DMSO was added dropwise to the solution over 30 minutes in an argon environment. Chloroform and toluene were then removed under vacuum, followed by addition of 16 mL of de-ionized water over 30 minutes using a syringe pump. The mixture was substituted with fresh water using three rounds of centrifugation in centrifugal filter tubes (Vivaspin 20, 100kDa MWCO). Finally, empty micelles were removed by three rounds of ultracentrifugation (100,000 x*g*, 1 hour).

3.3.1.3 Iron Concentration Measurements

Iron concentrations were measured using the colorimetric ferrozine assay[151]. For water-soluble coated IONPs, 50 µl of sample was mixed with 50 µl of 12 M HCl and incubated at room temperature for 30 minutes. For IONPs suspended in toluene, 10µL of IONP sample was added to 50uL of 12 M HCl and incubated at room temperature for 30 minutes with occasional vortexing, then 10uL of the aqueous phase was removed and added to 50 µL de-ionized water and 40 µL 12 M HCl. 240 µl of 2 M NaOH, 50 µl of 4 M ammonium acetate, 110 µl 5% hydroxylamine HCl, and 500 µl water were then added sequentially to the mixture in that order. After 30 minutes of incubation, 50 µl of the solution were mixed with 0.02% ferrozine solution in a 384 well plate. Light absorption was read at 562 nm with 810 nm as the reference wavelength using a microplate reader. The absorption was compared to a molecular iron standard to determine the concentration.

3.3.1.4 Characterization

Transmission electron microscopy (TEM) was used to determine the size and shape of the iron oxide cores after synthesis. Briefly, 5 µL of as-synthesized cores in toluene (~ 40 µg Fe/mL) were drop-cast onto carbon coated TEM grids. Images were recorded using a HT7500 microscope (Hitachi) operating at 75 kV attached to a CCD camera.

Dynamic light scattering (DLS) was used to investigate the hydrodynamic diameters of the coated iron oxide nanoparticles. Samples were diluted to 100 µg Fe/mL in de-ionized water and filtered using a 0.2µm syringe filter to remove dust particles. Measurements were taken at 25°C using a DynaPro Nanostar DLS instrument (Wyatt). The intensity weighted distribution was reported.

The effect of aggregation on MR contrast was measured using a 0.47 T Minispec Analyzer MQ20 (Bruker). The transverse relaxation times of IONPs (concentrations from 1 μg Fe/mL to 10 μg Fe/mL) were recorded at 40°C using the Hahn spin-echo method. T_2 relaxivity (r_2) was calculated by plotting $1/T_2$ against the molar concentration of iron and calculating the slope using linear regression.

Magnetic fluid hyperthermia heating efficiency was analyzed by measuring the temperature rise when samples were exposed to an alternating magnetic field (3355 kHz, 23.77 kA/m) generated by a 7.5-turn, 2.54 cm inner diameter inductor coil. A 1 mL aqueous suspension of IONPs (400 μg/mL) was placed inside the coil with polystyrene insulation, and the temperature was measured in real time using a fiber optic temperature probe. The slope of the linear region of the temperature vs. time plot was calculated using linear regression and normalized to a water sample. The specific absorption rate (SAR) was calculated using the equation

$$SAR\left(\frac{W}{g}\right) = \frac{C_p \times m_{H2O} \times \Delta T/t}{m_{Fe}}$$

where C_p is the specific heat of water, m_{H2O} is the mass of water, $\Delta T/t$ is the normalized slope of the temperature vs. time plot, and m_{Fe} is the mass of iron.

All presented values represent 3 independent measurements of single samples. Error bars represent standard deviation of these measurements.

3.4 Results and Discussion

IONP cores were synthesized using the thermal decomposition method in benzyl ether with $Fe(acac)_3$ as the metal precursor. The synthesized particles were monodisperse with diameters of 8.2 ± 1.6 nm and 15.1 ± 2.2 nm as measured by TEM (Figure 3-1). The particles displayed superparamagnetic properties, with magnetic saturation values of 88.4 and 89.6 emu/g for 8 nm and 15 nm IONPs, respectively, as measured using a SQUID magnetometer.

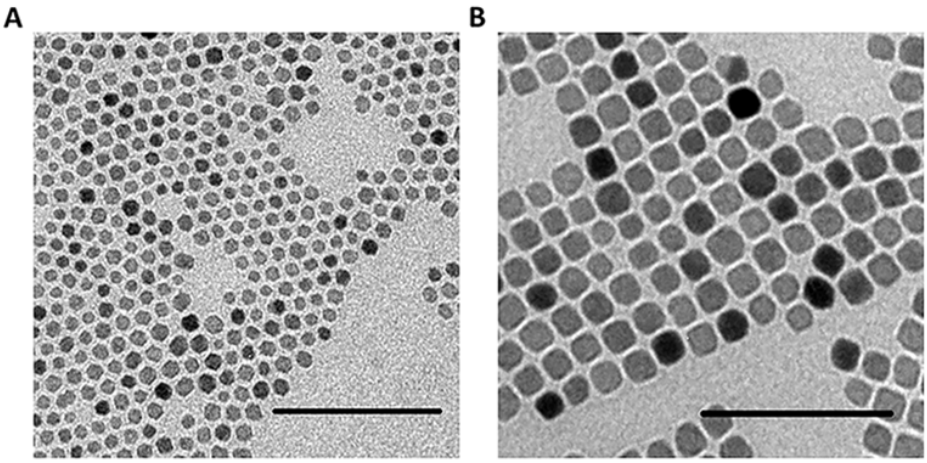

Figure 3-1 : Iron Oxide Nanoparticle Characterization. Representative TEM images of A) 8 nm and B) 15 nm iron oxide cores. Scale bar – 100 nm

We sought to investigate if the self-assembly of IONPs into clusters could be driven by modifying the dual-solvent exchange coating technique. The dual-solvent exchange process works by altering the surface energy of the iron oxide cores through changes in the polarity of the environment. This increases the strength of hydrophobic interactions between the hydrocarbon ligands on the nanoparticle surface and the phospholipid block of DSPE-PEG, driving self-assembly into the final core-shell structure in a process

analogous to the formation of micelles. We had previously observed that larger coating ratios (defined as the mass ratio of DSPE-PEG to iron in the coating reaction) were necessary to stabilize smaller iron oxide cores. This is presumably due to their higher total surface area per mass of iron (i.e. higher surface area to volume ratio) - an increased amount of DSPE-PEG was needed to stabilize the increased hydrophobic surface area. This inspired us to attempt to shift the equilibrium of the system by purposefully using lower coating ratios, such that DSPE-PEG would no longer be in sufficient quantity to stabilize the entire surface area of cores as single entities. We hypothesized this would force the nanoparticles to cluster within the DSPE-PEG shell in an effort to minimize their surface energy and reduce the total surface area to be stabilized by DSPE-PEG.

Two different sizes of iron oxide cores (8 nm and 15 nm) were coated at different DSPE-PEG:Fe coating ratios (from 0.5:1 to 4:1 w/w), and the resulting nanoparticles were analyzed using dynamic light scattering. We found that lower coating ratios resulted in larger hydrodynamic diameters, indicative of core clustering induced by the coating process (Figure 3-2). We only show results for two coating ratios which produced singly-dispersed cores (4:1 and 2:1 for 8 nm cores, 2:1 and 1:1 for 15 nm cores), and two coating ratios which produced clustered systems (1:1 and 0.75:1 for 8 nm cores, 0.75:1 and 0.5:1 for 15 nm cores). When coating ratios were normalized based on iron oxide core surface area, it can be seen that both iron oxide cores begin to cluster when the coating ratio is less than 2 DSPE-PEG molecules per nm^2.

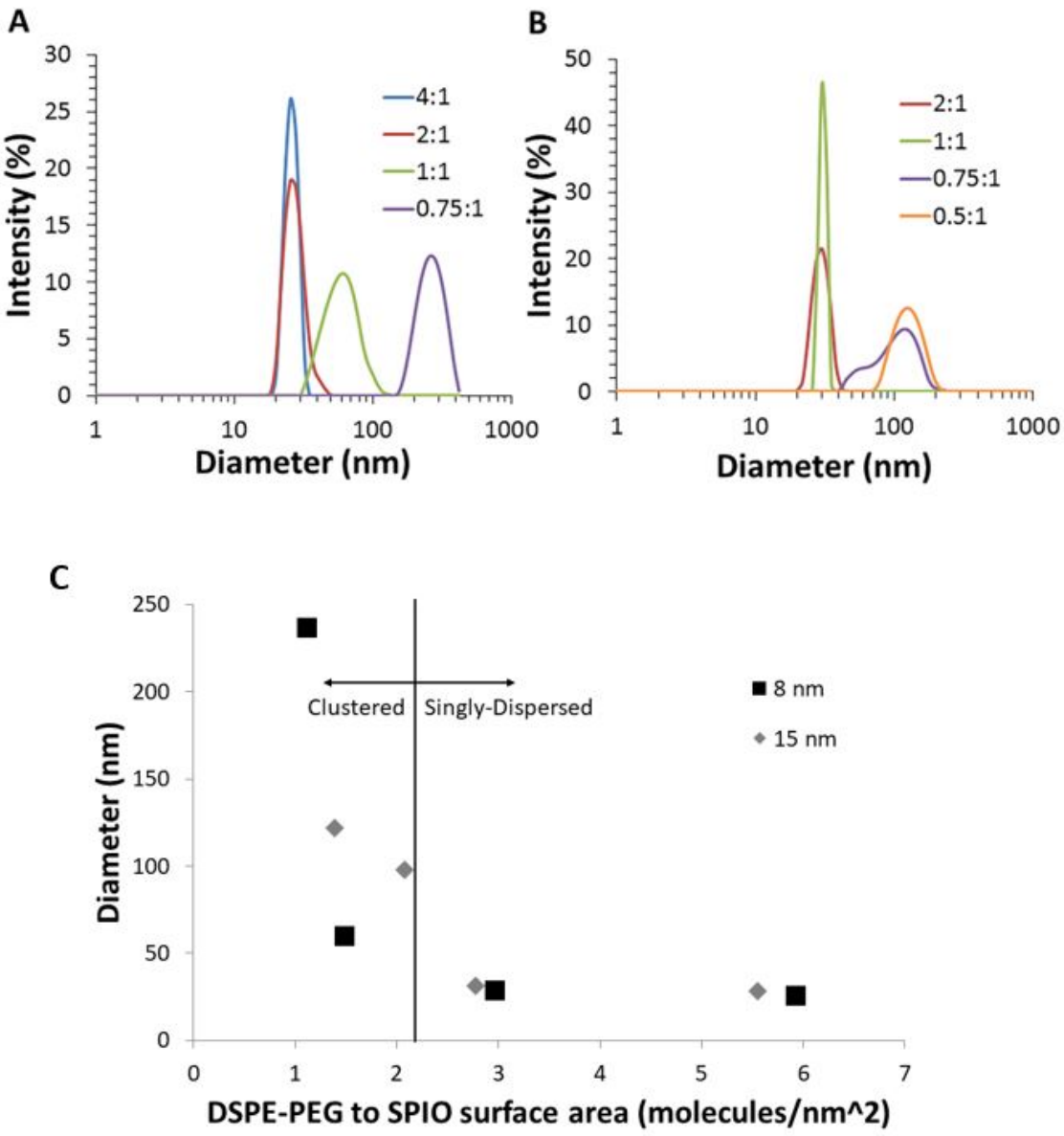

Figure 3-2: Size Distribution of Iron Oxide Nanoparticle Clusters. Intensity-weighted size distributions obtained via DLS of A) 8 nm IONP and B) 15 nm IONP coated with different mass ratios of coating particle (DSPE-PEG:Iron). C) Average diameter as a function of the initial ratio of DSPE-PEG to core surface area for 8 and 15 nm iron oxide cores.

This value compares favorably with Tong et al[149], who calculated that 6.5 nm iron oxide cores coated at a 1:1 DSPE-PEG:Fe ratio had a surface coverage of ~1.6 DSPE-PEG molecules per nm^2 for singly-dispersed nanoparticles. The formation of empty micelles during coating is likely a competing process, which reduces the nominal amount of DSPE-PEG available for coating the iron oxide cores, such that an initial loading ratio of ~2 DSPE-PEG molecules per nm^2 is unlikely to be the final density of DSPE-PEG on the nanoparticle surface. It appears that if the amount of DSPE-PEG available for coating is insufficient to reach that particular surface coverage, the particles cluster together to reduce their exposed surface area. The fewer DSPE-PEG molecules present initially, the greater the extent of clustering when the solution reaches equilibrium.

Next, we sought to examine how IONP clusters created with our technique could be used as MRI contrast agents. Iron oxide nanoparticles generate MR contrast by shortening the transverse relaxation of water protons in their vicinity. This can be quantified by the relaxivity r_2 (defined as the decrease in the characteristic relaxation time T_2 per concentration of iron). As expected, 15 nm cores showed higher relaxivity values compared to 8 nm cores, consistent with previous results[152]. For 8 nm cores, singly-dispersed cores (4:1 and 2:1 coating ratios) showed similar r_2 values (94 and 89 $mM^{-1}s^{-1}$, respectively), while the clusters showed higher r_2 values up to 165 $mM^{-1}s^{-1}$ (0.75:1 coating ratio) (Figure 3-3). The same trend was observed for 15 nm cores (Fig. 3B), with r_2 values ranging from 269 $mM^{-1}s^{-1}$ for singly-dispersed cores (2:1 and 1:1 coating ratio), up to 634 $mM^{-1}s^{-1}$ for the largest clusters (0.5:1 coating ratio).

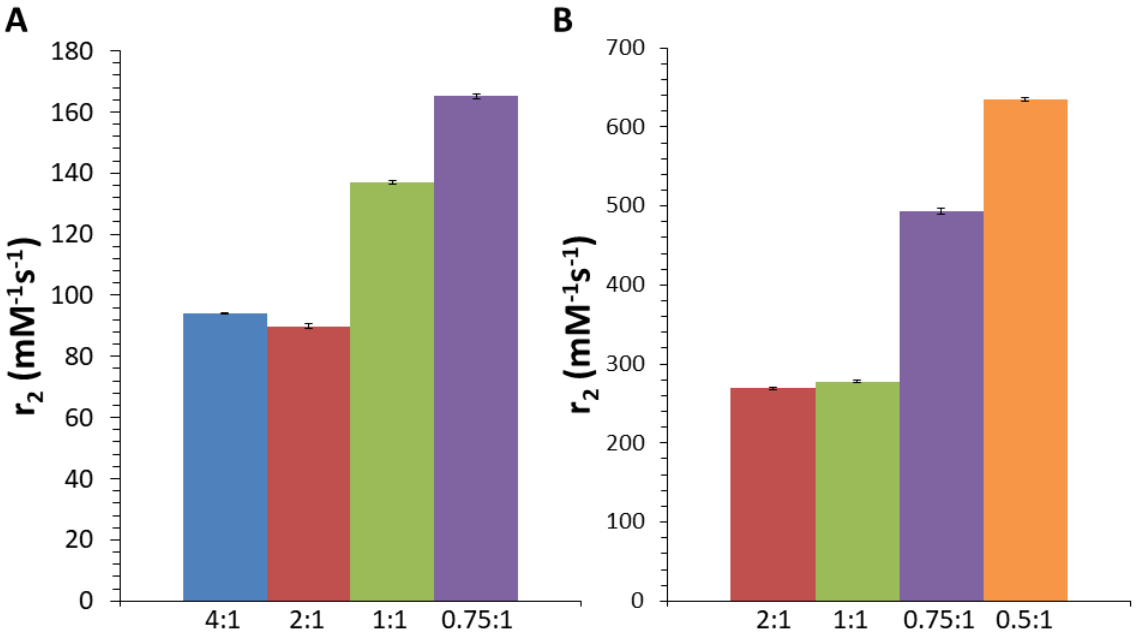

Figure 3-3: T_2 Relaxivity of Iron Oxide Nanoparticle Clusters. Calculated T_2 relaxivity for (a) 8 nm and (b) 15 nm IONP cores coated with different DSPE-PEG:Fe ratios (mean ± s.d., n = 3).

Outer sphere theory predicts that r_2 values increase as particle size increases, known as the motional averaging regime (MAR), due to an increase in the local magnetic field homogeneities that lead to dephasing of water protons in the vicinity of the particles. Monte-Carlo simulations of magnetic nanoparticle clusters by Matsumoto et al. demonstrate increased R_2 with increasing aggregate size, as these clustered particles are believed to behave magnetically as single large spheres[84]. The increase in R_2 due to nanoparticle clustering has been achieved experimentally by other groups, but the techniques utilized to drive self-assembly involve the use of di-block or tri-block copolymers synthesized in-house[85-87]. This increases the complexity of the method,

decreasing the accessibility for other labs and increasing potential regulatory hurdles. The technique presented here uses commercially available and FDA-approved DSPE-PEG, which simplifies the overall process. Furthermore, the R_2 value of 634 $mM^{-1}s^{-1}$ for the largest cluster of 15 nm IONP cores is among the highest ever reported.

Finally, we investigated the potential of the clustered IONPs to act as mediators for magnetic fluid hyperthermia. When placed in an alternating magnetic field, superparamagnetic nanoparticles experience relaxation losses (either Néelian or Brownian) which dissipate heat into the surrounding environment[153]. This heat generation can be quantified by the specific absorption rate (SAR), which describes the power output per mass of particles. The SAR was calculated by measuring the temperature increase of an aqueous solution of particles over time when exposed to AMF (355 kHz, 23.77 kA/m) (Fig. 4). As with T_2 relaxivity, we found that 15 nm cores showed higher SAR values compared to 8 nm cores, consistent with previous work[154].

For 8 nm cores, SAR values decreased with increasing cluster size from 147 W/g to 67 W/g for coating ratios of 4:1 and 0.75:1, respectively (Figure 3-4). 15 nm cores showed a similar trend, with SAR values decreasing from 616 W/g to 133 W/g for coating ratios of 2:1 and 0.5:1, respectively. While there is still debate about the effect IONP clustering has on SAR, the results here are consistent with the majority of those in the literature using similar systems[155, 156]. Both experimental and theoretical work have demonstrated that increased dipole-dipole interactions, which is likely to occur in clustered nanoparticle systems, lead to decreased heat output[157, 158]. Urtizberea et al found that increasing nanoparticle concentration (and thus increasing dipole-dipole interactions) decreased Néelian relaxation time and increased initial susceptibility, leading to a decrease

in SAR[159]. While more work is needed to fully elucidate the exact cause of SAR reduction in our present system, it appears that these clustered IONPs provide no clear benefit over singly-dispersed cores for hyperthermia applications.

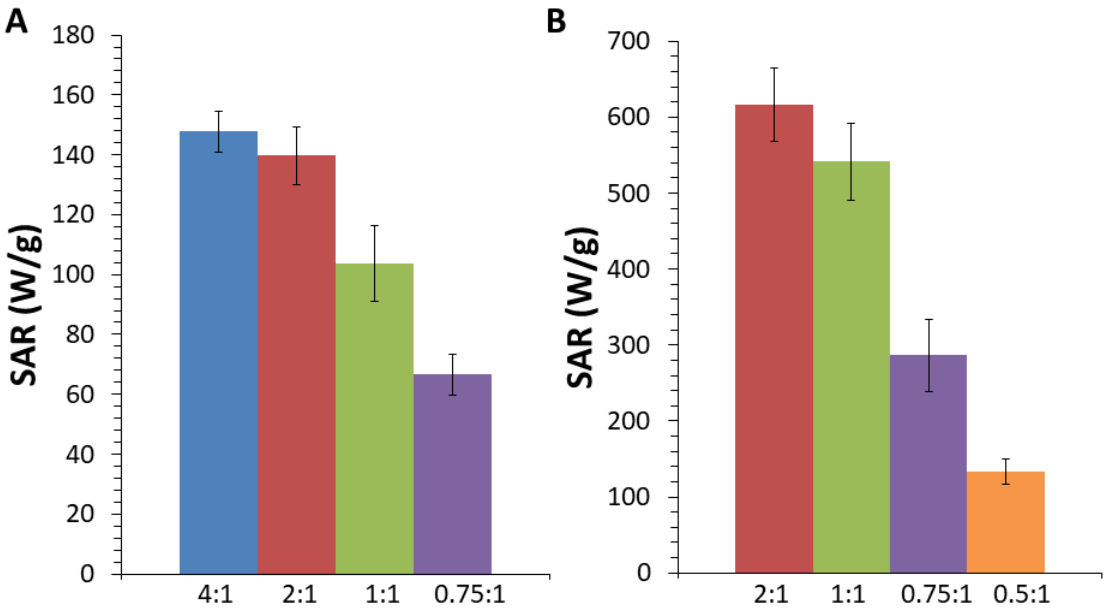

Figure 3-4: Heat Generation from Iron Oxide Nanoparticle Clusters. Calculated SARs for (a) 8 nm and (b) 15 nm iron oxide cores coated with different DSPE-PEG:Fe ratios exposed to an alternating magnetic field (23.77 kA/m, 355 kHz) (mean ± s.d., n = 3)

CHAPTER 4. PRECISE CONTROL OVER SPATIAL ORGANIZATION AND T_2 RELAXIVITY OF IRON OXIDE NANOPARTICLES USING DNA ORIGAMI

4.1 Abstract

The assembly of iron oxide nanoparticles into clusters is a promising avenue for the development of the highly efficient contrast agents for molecular imaging applications using MRI. Current techniques for inducing clustering are relatively crude, producing heterogeneous populations of primarily spherical arrangements with minimal control over the spatial organization of individual particles. In contrast, structural DNA nanotechnology has emerged as a promising technology for the organization of materials into arbitrary, prescribed shapes at the nanoscale. We have developed a DNA origami nanorod that is capable of precisely arranging DNA-coated iron oxide nanoparticles into prescribed patterns and use this system to investigate how parameters such as particle number and inter-particle spacing effect enhancement in MRI contrast generation. We demonstrate independent control over the number and spacing of iron oxide nanoparticles using the underlying DNA nanostructure as a scaffold. Furthermore, we find that discrete variations in the number of particles lead to significant increases in T_2 relaxivity, with a maximal enhancement of 140%. In contrast, variations in particle spacing between 40 and 100 nm appears to have little to no effect. This system is a promising platform to interrogate the effects of iron oxide nanoparticle self-assembly on MRI contrast, facilitating the creation of the next generation of magnetic nanoparticle-based molecular imaging contrast agents.

4.2 Introduction

Magnetic resonance imaging (MRI) has emerged as a staple of modern diagnostic medicine with a wide variety of uses. However, there are some instances in which native contrast between regions of the body with similar chemical/magnetic properties makes it difficult to identify and diagnose a variety of pathologies. In these instances, an exogenous contrast agent can be used to artificially alter the MRI signal and thus enable the identification of contrast agent biodistribution and its interactions with native tissues. Superparamagnetic iron oxide nanoparticles (IONPs) are one class of contrast agent which has demonstrated clinical success and generated considerable pre-clinical research interest as molecular imaging agents. One major focus of these research efforts is to synthesize more efficient IONP-based contrast agents, which can generate stronger MRI signals at lower delivered doses. One particularly appealing option is the assembly of individual particles into larger clusters, which has been demonstrated to produce significant enhancements in T_2 relaxation. The majority of techniques used to induce this self-assembly leverage hydrophobic-hydrophilic interactions between hydrophobic IONPs and amphiphilic polymers to cluster IONPs inside a polymer shell[85-87, 145]. These techniques are limited to producing heterogeneous populations of isotropic spherical clusters with minimal control over the spatial organization of particles within the assemblies. Other studies have demonstrated the use of anisotropic scaffolds such as bacteriophages[160] and DNA[109] to direct the assembly of IONPs, but in-depth studies using these systems is still limited. Theoretical simulations of this clustering-induced T_2 enhancement have been used to predict how fine changes cluster organization alter MRI contrast, but the lack of experimental control over these parameters has hindered model

validation [66, 83, 84, 105]. A new technology is needed to facilitate control over the spatial organization of IONPs in order to better understand cluster-induced T_2-contrast enhancement and engineer the next generation of iron-based MRI contrast agents. Over the past decade, structural DNA nanotechnology has emerged as one of the premier platforms for the precise organization of matter at the nanoscale. DNA nanostructures have been used for the organization of a diverse range of materials, including gold nanoparticles, quantum dots, fluorescent dyes, and proteins[1]. However, the use of this technology to direct the assembly of IONPs has been extremely limited, with only one previously published study demonstrating minimal control over spatial organization and no functional effects[161]. In this work, we demonstrate the ability to precisely control the spacing and number of DNA-modified IONPs using a custom-designed 130 nm DNA origami rod, allowing us to investigate how these parameters affect T_2 relaxivity. This work represents a novel method for controlling the clustering of IONPs with high precision, opening up the possibility for the precise engineering of MRI contrast agents that can be used for sensitive molecular imaging applications.

4.3 Materials and Methods

4.3.1.1 Materials

All short synthetic oligonucleotides were purchased from IDT, using desalting purification where available (and HPLC-purification for modified strands where necessary). All strands were used without further purification, unless otherwise noted. M13 bacteriophage and E. Coli were obtained from collaborators. OligoTex beads were purchased from Qiagen. Freeze'N'Squeeze Columns were purchased from BioRad. NAP-

5 columns were purchased from GE Healthcare. Dibenzocyclooctyne-ester (either N-hydroxysuccinimide or sulfo-tetrafluorophenol) were purchased from Click Chemistry Tools. 15 nm hydrophobic IONPs and 10 nm streptavidin-modified IONPs were purchased from Ocean Nanotech. Poly(maleic anhydride-octadecene)-azide (PMAO-N_3) and 10 nm DNA-coated IONPs were provided by collaborators (Chuan Zhang). All other chemicals were purchased from Sigma Aldrich or Fisher Scientific and used as received.

4.3.1.2 Scaffold Preparation

The p7560 scaffold was prepared following a published protocol[162]. All solutions and tubes were autoclaved prior to use. K91endA E. Coli cells were grown overnight in LB media in a shaking incubator (37C, 280 rpm) until proper density was reached, as determined by absorbance at 600nm. An aliquot of the LB/bacteria solution was then transferred to 2xYT media and allowed to grow for an additional 1.5 hours (37C, 280rpm) until proper density was reached (~0.5OD). 1mL of 1M magnesium chloride ($MgCl_2$) was added, followed by the addition of p7560 bacteriophage diluted 8x in 10mM Tris buffer. Bacteria were allowed to grow in the incubator for another 2 hours, and then the growth media was transferred to 500mL centrifuge flasks. The solution was centrifuged (8,000xg, 4°C, 15 minutes) to pellet bacteria and the supernatant was removed. 400mL of supernatant was added to 12 grams sodium chloride (NaCl, 3% w/v final concentration) and 16 grams of poly(ethylene-glycol) with 8000 molecular weight (PEG-8000, 4% w/v final concentration) and placed in an ice bath for 10 minutes. Bottles were centrifuged again with same conditions to precipitate phage. The supernatant was decanted and the pelleted phage was resuspended in 4mL 10mM Tris buffer. Next, 8mL of 0.2M sodium hydroxide (NaOH)/1% SDS solution was added and incubated for 2 minutes, followed by

the addition of 6mL 3M potassium acetate, pH 5.5 and incubated for 20 minutes on ice. The tubes were centrifuged and the supernatant containing the p7560 scaffold was removed. EtOH precipitation was then used to concentrate DNA and remove excess salt, and DNA concentration was normalized to 200nM with dilution in ultra-pure water.

4.3.1.3 DNA Origami Design and Synthesis

DNA origami structures were designed using the caDNAno software[14] on a square lattice with a 4x4 double-helix grid (16 helix bundle, 16HB). To synthesize the structures, staples were mixed with p7560 DNA scaffold (10-30 nM) in 10-fold molar excess in aqueous buffer (5 mM Tris base, 1 mM EDTA, and 10mM $MgCl_2$) with a total volume of 50 µL. The solution was annealed in a thermocycler over 18 hours, following the protocol: 85°C for 10 minutes to denature strands, then 60 to 24 °C, at 30 min/°C. Additional details about designing and synthesizing DNA origami structures can be found elsewhere [9, 163].

4.3.1.4 Agarose Gel Electrophoresis and 16HB Purification

Crude DNA origami/staple mixtures were run on native agarose gel electrophoresis with varying percentages (typically 1.5% for analytical gel and 0.67% for high yield purification gel) for 1-2 hours (gel prepared in 0.5 × TBE buffer - 45 mM Tris, 45 mM Boric acid, 1 mM EDTA, 10 mM $MgCl_2$ and 0.005% (v/v) EtBr) at 50-60V, depending on the size of gel box. Then, the target bands were excised and placed into a Freeze 'N Squeeze column. The gel pieces were crushed into fine pieces by a microtube pestle and the column was then centrifuged at 7000 rcf for 5 minutes. Samples that were eluted through the column were collected for subsequent experiments. The concentration of 16HB samples

was estimated by measuring the weight-concentration of dsDNA using a NanoDrop spectrophotometer at 260nm and dividing by the approximate molecular weight (4.6MDa).

4.3.1.5 PEG Precipitation Purification

High yield recovery of 16HB was obtained using a PEG precipitation method, as described elsewhere[163]. Briefly, crude DNA origami mixtures obtained directly after annealing were adjusted to a final volume of 200uL and a final concentration of 20mM $MgCl_2$ using 1xFoB (5mM Tris, 1mM EDTA, 5mM NaCl) and 100mM $MgCl_2$. 0.7uL of a .01% EtBr was added to the solution, along with 200uL of the precipitation solution (15% w/v PEG-8000, 5mM Tris, 1mM EDTA. 505mM NaCl). The mixture was centrifuged (16,000xg, 4°C, 25 minutes), and the supernatant was decanted under UV-irradiation to assist in pellet identification. The pellet was resuspended to 200uL 1xFoB+20mM $MgCl_2$ and then precipitation process was repeated again. The final pellet was resuspended in 1xFoB+10mM $MgCl_2$ for further use.

4.3.1.6 Transmission Electron Microscopy (TEM) Sample Preparation

3 to 8 μL of samples were deposited onto glow-discharged, carbon-coated copper TEM grids for 30 seconds – 5 minutes, depending on approximate 16HB concentration. Residual solution was wicked away using filter paper and grids were then stained for 30 seconds using a 1% aqueous uranyl formate solution containing 25 mM NaOH. Imaging was performed using a Hitachi HT7700 microscope operated at 80 kV.

4.3.1.7 IONP Concentration Measurements

Iron concentrations were measured using the colorimetric ferrozine assay. 50 µl IONP solution (approximate concentration ~40 µg/mL) was mixed with 50 µl of 12 M HCl and incubated at room temperature for 30 minutes. 240 µl of 2 M NaOH, 50 µl of 4 M ammonium acetate, 110 µl 5% hydroxylamine HCl, and 500 µl water were then added sequentially to the mixture in that order. A low volume protocol for use with small quantities of samples was also developed, using $1/5^{th}$ volumes (10uL sample, 10uL 12M HCl, 48uL 2M NaOH, 10uL 4M ammonium acetate, 22uL hydroxylamine HCl). After 1 hour of incubation, 50 µl of the solution were mixed with 0.02% ferrozine solution in a 384 well plate and left for 1 hour on mixer. Light absorption was read at 562 nm with 810 nm as the reference wavelength using a microplate reader. The absorption was compared to a molecular iron standard to determine the concentration. Molar IONP concentrations were calculated from iron weight concentrations by calculating the mass of a single particle assuming perfect spherical geometry, an Fe_3O_4 density of 5.15 g/cm_3, and a Fe_3O_4 weight concentration 38% higher than Fe weight concentration. For example, a 100ug/mL Fe concentration would give 25nM for 15nm IONP cores and 85nM for 10nm IONP cores.

4.3.1.8 DNA-IONP Synthesis – IONP Coating

IONP were coated with PMAO-N_3 using a previously published protocol[164]. Briefly, a 20mL scintillation flask and stir bar were washed with deionized water, dried overnight in an oven at 90°C, and then washed with anhydrous chloroform stabilized with amylene (Note: VERY important to use amylene-stabilized chloroform, rather than ethanol-stabilized chloroform). Anhydrous amylene-stabilized chloroform and IONPs

(25mg/mL Fe, 6.3μM IONP) were mixed together in the vial to a final concentration of 50nM IONP in 5mL of chloroform. To this mixture, 200mM (monomer concentration) PMAO-N_3 was added dropwise into the mixture under stirring until the ratio of polymer monomer units to IONP surface area was 300:1 (corresponding to ~210,000 molar excess for 15nm IONPs). This solution was allowed to incubate at room temperature on a stir plate for 2 hours. The tube was then placed in a ~55°C water bath for 2 minutes with gentle mixing, and then allowed to cool to room temperature over 15 minutes. Chloroform was removed using a rotary evaporator, and the thin IONP film was hydrated in 2 mL of 75mM sodium borate, pH 9 solution via sonication for 1 hour. The resuspended IONP were filtered using a 0.2μm syringe filter and then purified using ultracentrifugation on a sucrose gradient (20-50% sucrose, 100,000xg, 2.5 hours, 4°C). The band containing the well-dispersed coated IONPs was removed using a syringe, and excess sucrose was eliminated using 3 rounds of washing in a VivaSpin (GE Healthcare) tube with 100 kDa molecular weight cut-off filter using deionized water. Coated particles were then stored at room temperature in deionized water until further use.

4.3.1.9 DNA-IONP Synthesis – DNA-DBCO Synthesis

In a typical synthesis, 50uL 1mM Amine-modified ssDNA was mixed with 50uL 30mM DBCO-STP Ester, 50uL 10x PBS, 50uL 1M sodium bicarbonate (prepared fresh), and 300uL deionized water, to give a final solution of 500uL, 100μM DNA, 30-fold excess DBCO-STP Ester, 1x PBS, 100mM sodium bicarbonate. The tube was covered in foil and placed on mixer and left at room temperature overnight. For purification, the mixture was run through 3 rounds of ethyl acetate extraction, in which 1mL of ethyl acetate was added, the mixture was vortexed for 1 min, centrifuged at low speed, and then the ethyl acetate

was removed (Note: This part of the protocol was based on using DBCO-NHS esters which are more hydrophobic, and it is not clear if the ethyl acetate extraction is really need to remove excess DBCO-STP esters). 1mL of ethanol was added, and the mixture was stored at -20C for ~30 minutes, and then centrifuged (16,000xg, 4C, 30 minutes). The supernatant was decanted, the pellet dried and then resuspended in 500uL H2O, and then the mixture was desalted using a NAP-5 desalting column. The flow through was collected and the water removed using a speed-vac, followed by resuspension of the dried DNA in H2O. The use of DBCO-NHS esters was also used and worked well – 50mM DBCO in DMSO was used, and the 300uL of water was replaced with 250uL DMSO, 50uL water (for 60% DMSO final volume). In this case, a precipitate formed during overnight incubation, though this did not appear to impact the quality of the final product. Finally, HPLC could also be used to purify the DBCO-DNA and is theoretically better because it removes unreacted amine-DNA. However, there was no significant difference in either method when testing IONP conjugation, so ethyl acetate extraction and desalting was primarily used due to the fact that it is simpler.

4.3.1.10 DNA-IONP Synthesis – DNA Conjugation

DNA strands were conjugated to PMAO-N_3-coated IONPs using a copper-free click chemistry reaction, based on a previously published protocol (Zhang 2013). DBCO-modified ssDNA was mixed with PMAO-coated IONPs with a final ratio of 1 DNA/nm^2 IONP surface area (for 15nm IONPs, this corresponded to 700x molar excess). Reactions were typically run in 100uL deionized water with 50nM IONPs – larger volumes led to issues with reaction efficiency. The DNA/IONP mixture was allowed to incubate overnight at room temperature on mixer. A salt-aging protocol was then used to increase density of

DNA on the IONP surface - titrated additions of 5M NaCl were added to the DNA/IONP solution over 8 hours, with new NaCl additions every hour. Volumes of NaCl were added to raise concentration to 50mM with first addition, 100mM for second addition, and then in 100mM steps up to 700mM after 8 hours. The final mixture was then left overnight at room temperature on mixer, followed by purification using 3 rounds of centrifugation (18,200xg, 1 hour) and resuspension in 1xFoB.

4.3.1.11 DNA-IONP Characterization

DNA-IONPs were characterized using both dynamic light scattering (DLS) and agarose gel electrophoresis. 50µL of a DNA-IONP solution (~5nM IONP) was added to a glass-bottom 384 micro-well plate and light scattering was measured using a DynaPro III plate reader (Wyatt Technologies). The hydrodynamic size and polydispersity index were calculated using cumulants analysis, while the regularization size distribution results were reported as the intensity-weighted distribution. For agarose gel electrophoresis, DNA-IONPs were loaded into a 1% agarose gel made with 1xTBE buffer and ran for 30 minutes. Ethidium bromide staining and UV illumination was used to visualize excess PMAO-N_3 polymer present in solution.

4.3.1.12 16HB-IONP Binding

Many different conditions were tested for optimizing binding of DNA-IONP to 16HB, and a general method is presented here. A 5-fold excess of IONP relative to the number of IONP binding sites was added to 1 - 2.5nM of 16HB in a final volume of 20-200uL. For example, for a 1nM solution of 16HB containing 3 binding sites would have a final DNA-IONP concentration of 15nM. The reaction was run in 1xFoB10 (5mM Tris,

1mM EDTA, 5mM NaCl, 10mM $MgCl_2$) and left to incubate for a specific time (15 minutes to overnight) at room temperature on a shaker. Agarose gel electrophoresis was used to monitor binding efficacy, and bands were excised and purified for TEM analysis. Binding yields were calculated by counting each 16HB in the field of view and binning based on the number of bound IONPs.

4.3.1.13 16HB-IONP Bead Purification

While the exact volumes and concentrations were varied based on the needs of the experiment, a general method for purification of 16HB-IONP from excess IONP is presented here. 4uL of Oligotex beads were washed via 1 round of centrifugation (7,000xg, 2 min) in 400uL of FoB10 (5mM Tris, 1mM EDTA, 5mM NaCl, 10mM $MgCl_2$) containing 0.01% Pluronic F-127 in a tube that had been blocked with a 5% Pluronic solution. A 16HB-IONP mixture (typically 200uL at around 1-2nM 16HB) was added to a tube containing the washed beads, and the mixture was left at room temperature for 3 hours on a rotary mixer. In general, 1uL of beads was used for every ~0.1pmol of 16HB (e.g. 4uL of beads for a 200uL, 1.5nM solution). After the 3-hour incubation step, the mixture was centrifuged (7,000xg, 2 min) and the supernatant was collected/discarded. The pellet was resuspended in 200uL of FoB10+F-127 and the process was repeated 2x more, for a total of 3 centrifugation steps. The use of buffer containing Pluronic was critical to prevent beads from adhering to the plastic tube, leading to a substantial loss of product. 4uL of release strand (containing a 25 polyA sequence and sequence complementary to 16HB connector toehold) was added to the bead/bound 16HB mixture and the tubes were left to incubate at 37°C in a rotary mixer, typically for ~16 hours. The amount of release mix added was not particularly important as long as it was in a large enough excess. In general, an equivolume

amount of 100uM release strand mix was added as Oligotex beads. After overnight incubation, the mixture was centrifuged again, and the release product was collected from the supernatant. Secondary centrifugation steps were occasionally needed to remove any excess beads that were left in supernatant. The quality of the release products was analyzed via agarose gel electrophoresis and TEM. Yield of release was calculated using ImagePro software by comparing relative band intensity of release and supernatant steps to a control impure sample.

4.3.1.14 T_2 Measurements

After collecting 16HB-IONP following bead purification, the samples were diluted 1:2 and 1:4 times in 1xFoB10+.01% F-127 to a final volume of 600uL each. Samples were then transferred to a 10mm NMR tube and T_2 was measured using a Resonance Maran Ultra NMR. T_2 values were extracted by fitting an exponential decay to data obtained from a standard CPMG pulse sequence. The measurement parameters include: 0.55 T, 30°C, Number of Echoes: 1024, Time delay between echoes: 1ms, pulse length - 3μs, receiver delay: 10s. The T_2 values at 3 different concentrations were obtained, and a linear fit was used to calculate r_2. Samples were then heated at 85°C for 10 minutes to denature the 16HB support, left to cool to room temperature for 1 hour, and then T_2 values were measured again and r_2 was calculated. Data was presented as percent change relative to heating

$$\%\ Change\ r_2 = 100 \times \frac{r_{2\ before\ heat}}{r_{2\ after\ heat}}$$

For dynamic T_2 Measurements, T_2 values for 2 identical samples were measured. 1μL of 6.25μM dimerization strands were added to one tube (600uL) and both samples were

left at 35°C on heating block. T_2 values for both were measured again at 1 hour, 3 hours, and 24 hours. Samples were then denatured as above and T_2 was measured again. Values are presented as T_2 normalized to either initial measurement (t = 0) or to the control sample without dimerization strands at each time point.

4.4 Results

4.4.1.1 16HB Design and Synthesis

The DNA origami rod used in this work was designed using caDNAno on a square lattice and consisted of 16 double helices bundled together on a 4x4 grid, with each helix ~396 bp long, or roughly 133 nm. ~20bp long free scaffold loops were included on each end to prevent base-stacking interactions, but also served as anchoring points for attaching additional strands used for incorporating elements on the ends of the structure. Individual staple domains were either 8 or 16nt long (3 or 4 domains per staple) with ~23nt between cross overs. Staple break points were designed in a way to produce 36 3'/5' ends on each face of the rectangular prism, arranged in 3 groups of 12. Using this system, additional domains could be appended to each of these break points, providing "capture" sequences extending from the faces of the 16HB structure that could interface with heteroelements labeled with complementary DNA. In this way, there are a maximum of 48 3-strand binding sites, with 12 located on each side of the rectangular prism. The caDNAno design files and strand list can be found in the appendix.

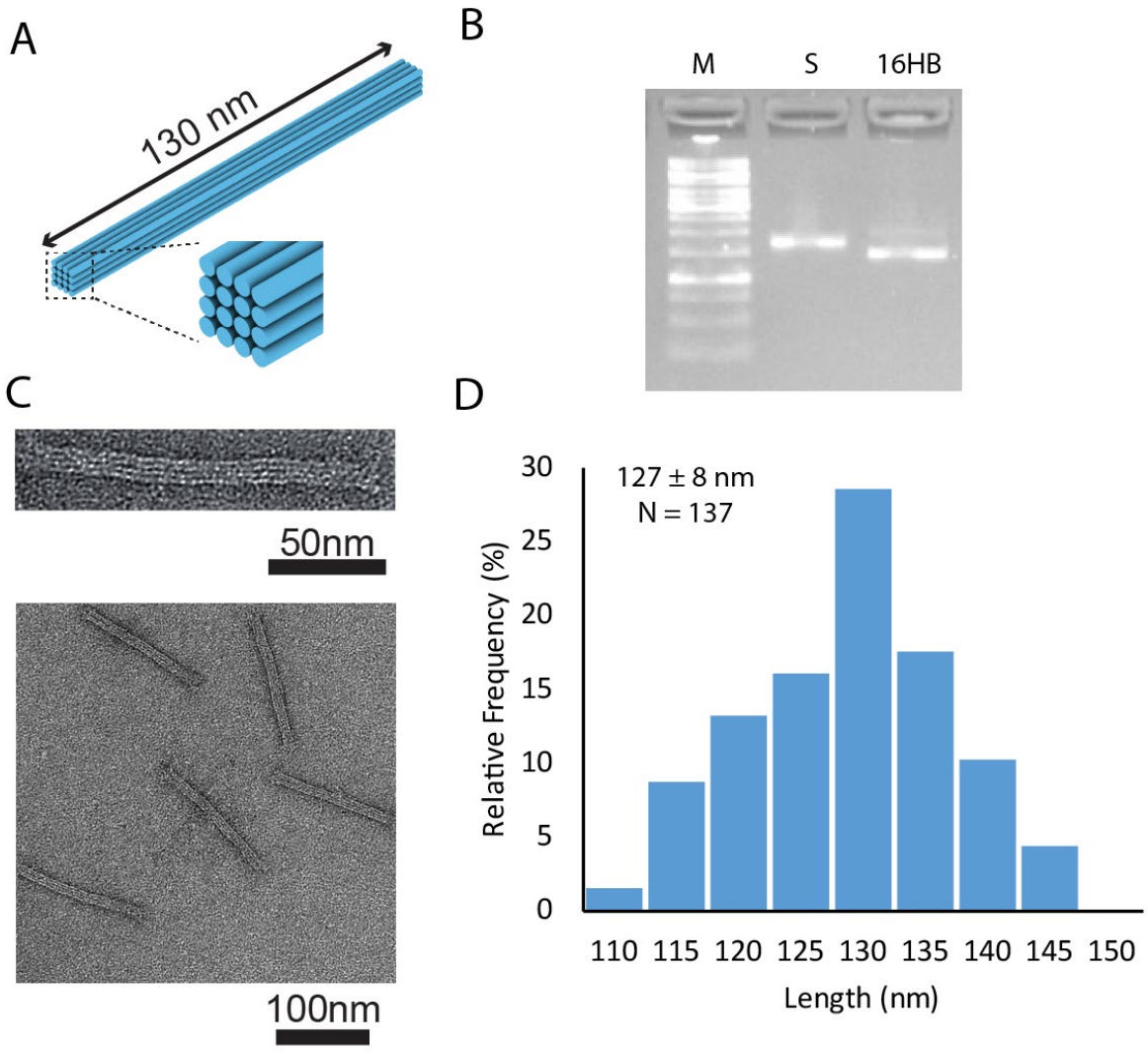

Figure 4-1: Characterization of 16HB DNA Origami Rod A) Model of 16HB B) AGE of 16HB; M - 1kB marker, S - p7560 scaffold C) Negative-stain TEM images of 16HB D) Length distribution of 16HB as measured from TEM.

The 16HB structure was synthesized using a thermal annealing protocol with a mixture of p7560 scaffold strand and excess staple strands and was then characterized using agarose gel electrophoresis and transmission electron microscopy (Figure 4-1). The 16HB assembles with high yield and migrates faster than the free scaffold on 1.5% agarose gels due to its compact geometric form. There does appear to be some minor dimerization/oligomerization as observed by a slower moving band. However, these byproducts do not appear to interfere with downstream applications. Negative-stain TEM imaging of the structures reveals well-formed rectangular prisms, with high magnification images showing the 4 parallel helices stacked together. Analysis of these structures gives an average length of 127 ± 8 nm, which matches well with the designed geometry (133 nm). While DNA origami structures are ideally highly monodisperse, the small variability in lengths observed here could be due to several factors: broken or damaged structures in which some of the length is lost can contribute to shorter 16HBs, while staining phenomenon which accentuate the free scaffold loops or human error during measurement could contribute to structures measured as larger than 135 nm.

In order to optimize assembly of the 16HB, we annealed structures in buffers containing variable amounts of $MgCl_2$ (8-18mM). Based on agarose gel mobility, the 16HB forms with high yield between 8 and 14mM, with assembly in 18mM magnesium leading to a decreased yield due to the appearance of large aggregated byproducts (data not shown). In order to further optimize assembly conditions, we varied a number of different parameters (magnesium concentration, assembly time, annealing temperature, and p7560 scaffold source) and analyzed the resulting 16HB using TEM imaging (Figure 4-2). We then classified each observed structure as either correct (green circle), damaged/broken

(red circle), or containing defects (yellow circle). In this instance, 16HB with defects were identified due to the presence of punctate areas of excess stain, which is typically indicative of minor abnormalities in DNA structure at that location. Statistical analysis of these populations reveals some minor trends in regard to assembly conditions which minimize the formation of abnormal structures – lower magnesium concentrations and lower annealing start temperatures corresponded to slightly higher yields of correctly folded structures, while annealing time and scaffold source had minimal to no effect (Figure 4-3). It should be noted that this kind of analysis is very qualitative and requires judgement calls over minor aspects in order to categorize structures, limiting the ability to draw really significant conclusions based on this data. However, we did choose to move forward with using 10mM magnesium, 60°C annealing temperatures, and 18-hour annealing times for all future experiments. It is also helpful to note that, while the use of a commercially available scaffold strand (IDT) did not produce notably better monomeric structures compared to scaffolds produced in the lab, the use of this commercial scaffold did limit the assembly of dimer/oligomer structures. While these structures are typically removed during purification and thus not particularly relevant to the work, this does point to there being some potential issue with the scaffold used in this study.

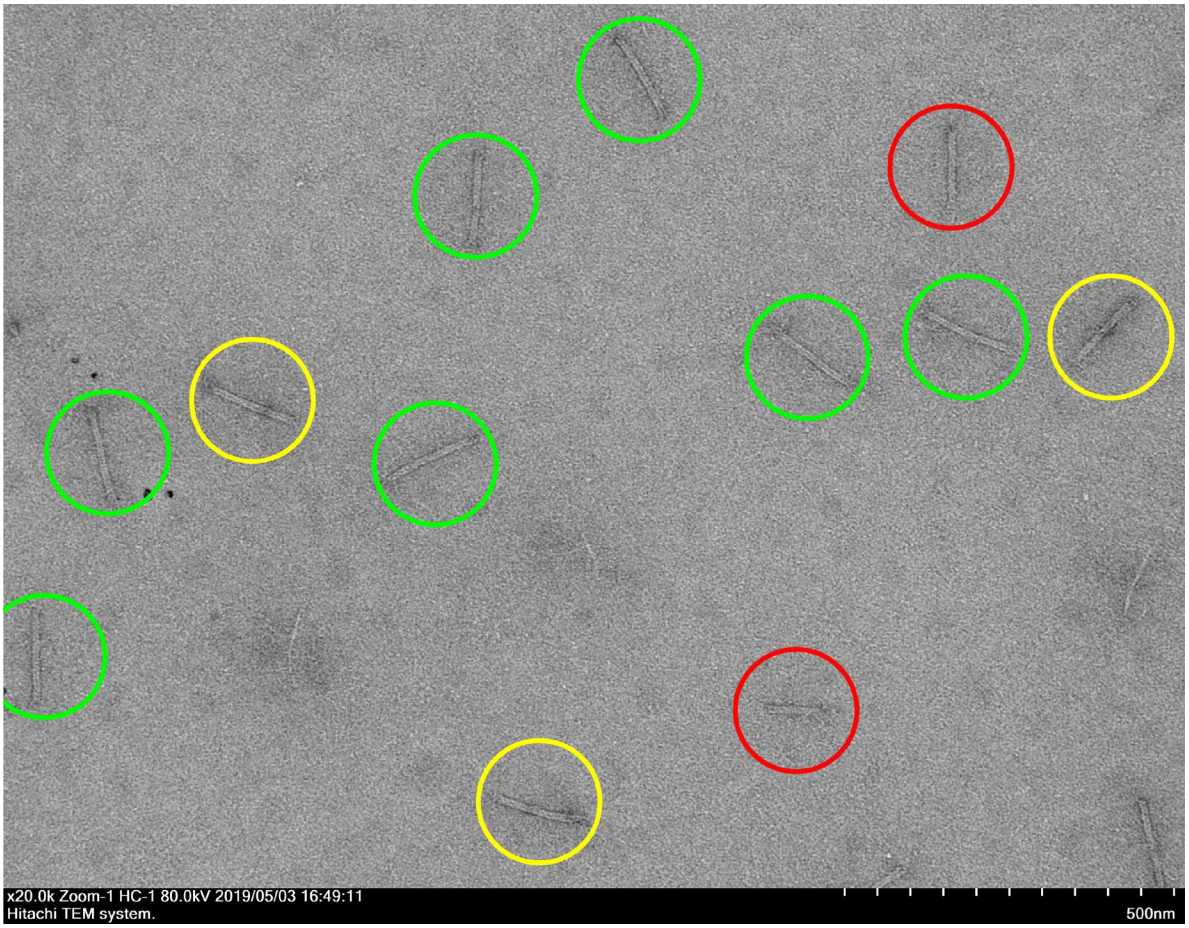

Figure 4-2: TEM Image Binning of 16HB Populations. Representative TEM image of 16HBs from defect analysis experiments. All 16HBs were binned based on their morphology: well-formed structures (green circles), structures with defects (yellow circles), and broken/damaged structures (red circles).

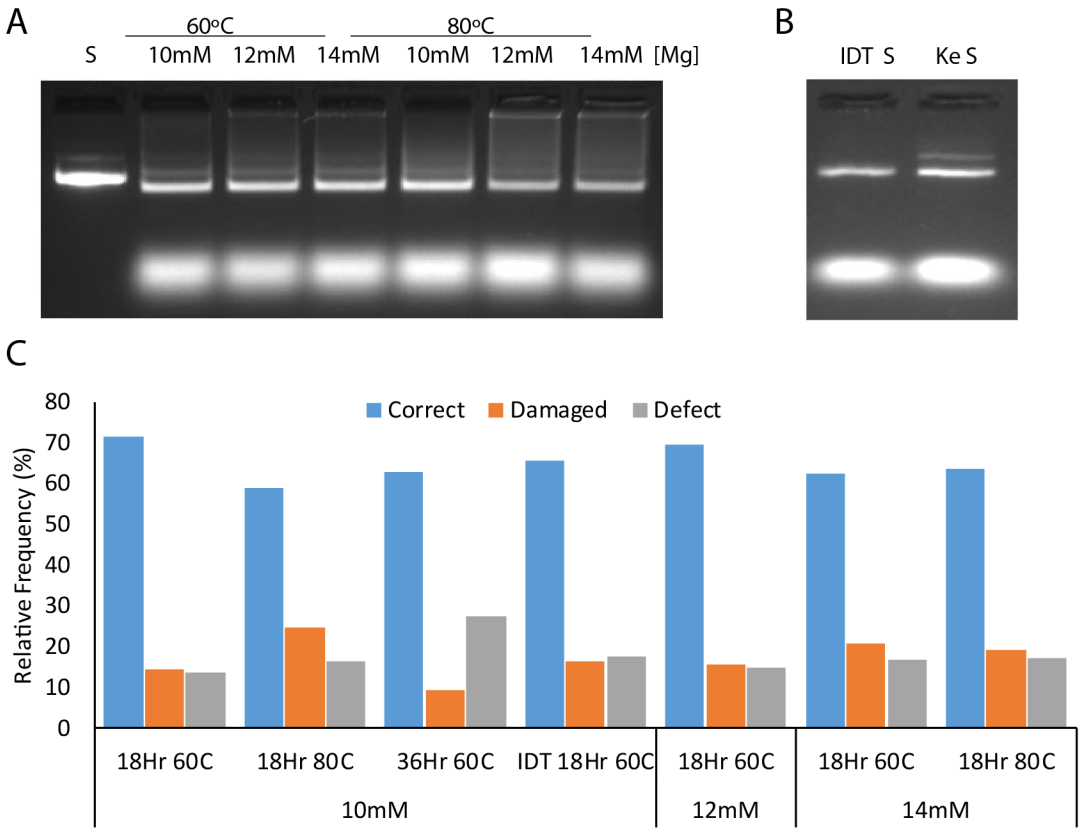

Figure 4-3. Analysis of 16HB Fidelity A) AGE showing assembly of 16HB with different annealing temperatures and $MgCl_2$ concentrations; S- p7560 scaffold. B) AGE of 16HB annealed with p7560 scaffold obtained commercially (IDT S) or produced in house (Ke S). C) Statistical analysis of 16HB populations annealed using different conditions from TEM image analysis.

Finally, we were also interested in testing dynamic 16HB assembly as a means of potential driving dynamic MRI signal changes. We designed dimerization strands that would bind to the free scaffold loops at the tail end of the 16HB in a manner that would link to different 16HBs together in a tail-to-tail orientation. This system produced DNA origami rods that were approximately 280 nm long with narrow size distribution, matching the expected dimensions of a 16HB dimer (Figure 4-4). Our first dimer strand design utilized 3bp sticky-end overhangs to drive dimerization and a 2nt ssDNA gap in between the dimerization strands and a filler strand – however, this design only induced ~40%

dimerization even after 18-hour reaction times. In order to improve on the dimerization efficiency, we redesigned the connecting strands to contain a 5bp sticky-ends with no gap, which should improve dimerization efficiency by increasing connection strength via longer complementary regions and base-pair stacking. This new design did indeed lead to much higher dimerization efficiencies approaching 100%. We then systematically evaluated several parameters which would likely influence dimer formation in an effort to identify optimal conditions. We found that adding a larger excess of connecting strands (up to 10-fold excess) led to increased dimer formation, with only modest improvements seen above 1-fold excess. Increasing the reaction temperature also led to improved dimerization efficiency. Finally, we monitored the kinetics of dimer formation, finding that at least 1 hour is needed at 35°C to produce dimers, and that times longer than 3 hours are needed to achieve the new quantitative conversion seen in previous overnight incubations.

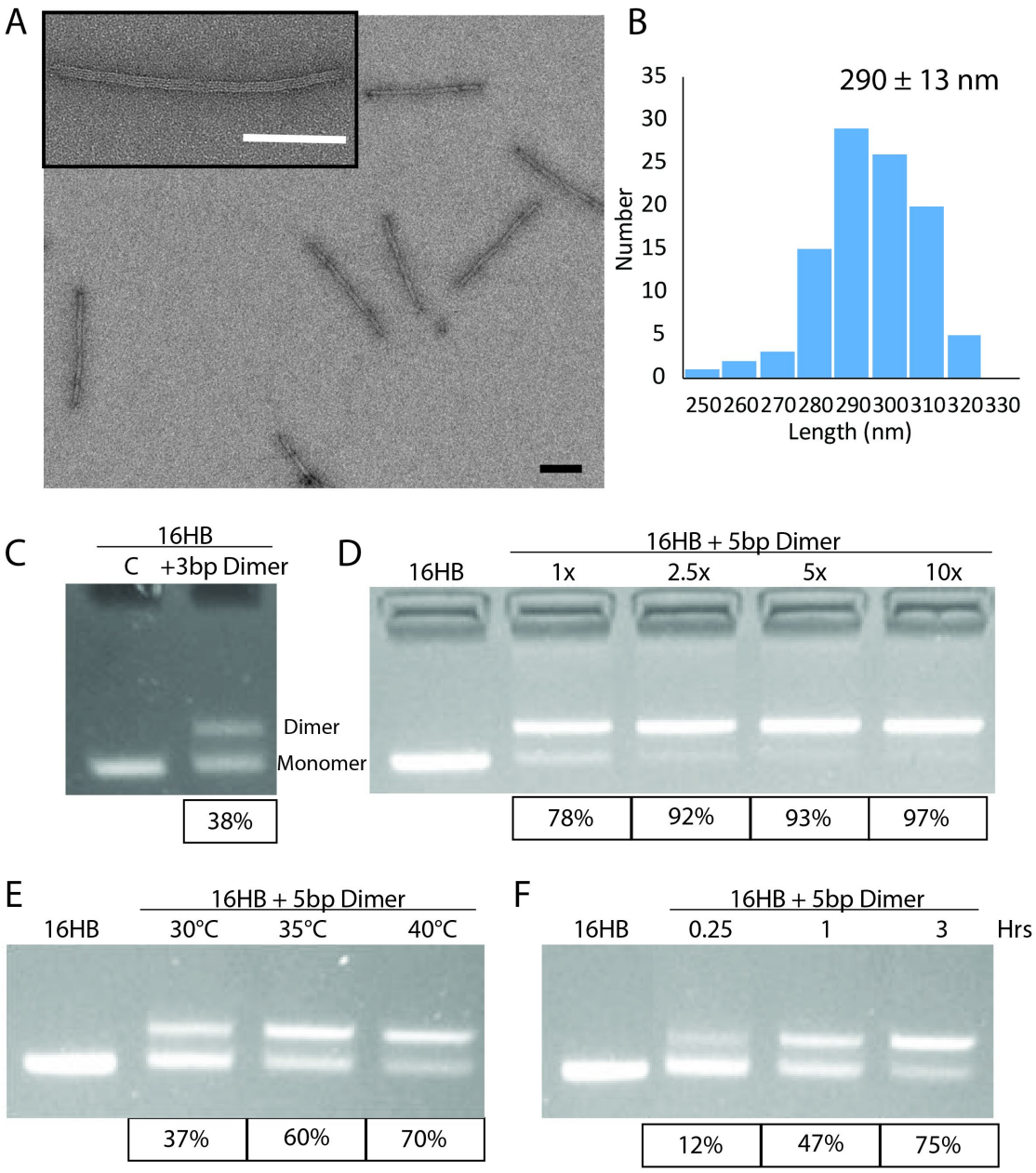

Figure 4-4. Formation of 16HB Dimers. A) Negative-stain TEM image of 16HB dimer structures. Scale bars - 100 nm. B) Distribution of 16HB dimer lengths calculated from TEM images (N = 112). C) AGE of 16HB dimer formed with 3bp overhang, including dimerization efficiency based on relative band intensity; C - Control 16HB without dimer strands. D) AGE of 16HB dimers formed with 5bp overhang at different dimer strand:16HB ratios (18 hour, 25°C). E) AGE of 16HB dimers formed at different temperatures (10x excess, 1 hour). F) AGE of kinetics of DNA origami dimer formation (35°C, 10x excess).

4.4.1.2 DNA-IONP Synthesis

In order to interface IONPs with our DNA origami structures, we needed to develop some form of interaction between the two species. Previous work by our group and others using other nanoparticles, such as gold and quantum dots, have established two different common methods: hybridization between complementary DNA on the DNA origami and nanoparticle surface[165-167], or biotin-streptavidin interactions between biotinylated DNA and streptavidin-modified nanoparticles[55, 168]. We investigated both avenues to identify which would work best for our IONP system.

We used commercially available streptavidin-modified IONPs for our initial studies. While this system worked, we found that overall yields were relatively low (vide infra) and thus sought to find a technique that would work better. Next, we worked on synthesizing DNA-modified IONPs. One major challenge in working with IONPs is that high-quality, monodisperse iron oxide cores must be synthesized in polar organic solvents using hydrocarbon-based stabilization agents such as oleic acid. While these particles are highly stable in solvents such as chloroform, their surface chemistry must be altered before they can be transferred into aqueous solutions for reaction with DNA. This aqueous transfer is done using two different techniques – ligand exchange, in which the hydrocarbon stabilizing ligands are replaced with water-soluble groups, or polymer-coating, in which amphiphilic polymers are used to coat the hydrophobic nanoparticles and present hydrophilic groups on the surface. Our attempts at ligand exchange using catechol-based ligands such a dopamine, nitrodopamine, and caffeic acid, which are known to have a high

affinity for iron oxide surfaces[169], were unsuccessful due to low stability of the particles after exchange (data not shown).

For the polymer-coating avenue, we first attempted to use commercially available IONPs coated with polymers containing reactive groups, such as carboxylic acids and primary amines. For IONPs functionalized with carboxylic acid, we used N-(3-Dimethylaminopropyl)-N′-ethylcarbodiimide (EDC)/ N-Hydroxysulfosuccinimide (Sulfo-NHS) crosslinkers to form covalent bonds between the IONP carboxylic acids and amine-functionalized DNA. Unfortunately, we were unable to synthesize DNA-coated IONPs using this technique. While the mobility of IONPs changed during AGE following reaction with EDC/NHS, no further changes were observed in mobility or in hydrodynamic diameter evaluated with DLS following addition of DNA (data not shown). For IONPs functionalized with primary amines, we used the heterobifunctional crosslinker sulfosuccinimidyl 4-(N-maleimidomethyl)cyclohexane-1-carboxylate (Sulfo-SMCC) in order to react with thiol-functionalized DNA. We were able to demonstrate shifts in electrophoretic mobility of IONPs following reaction with DNA and clear binding to 16HB bearing complementary capture sequences (data not shown). However, the samples were very messy and controls utilizing Amine-IONPs without reacting to DNA showed binding as well, which points to potential electrostatic interactions that complicate the use of this method.

Given these troubles, we turned to a 3rd conjugation chemistry using a ‘Click’ chemistry protocol. Click chemistry reactions, particularly those involving reactions between alkynes and azides, are widely used due to their reliability, specificity, high yield, and mild reaction conditions[170]. The synthesis of DNA-coated hydrophobic IONPs

using a click chemistry technique was accomplished by Chad Mirkin's group, in which a wide variety of hydrophobic nanoparticles could be decorated with DNA[164]. The general scheme of synthesizing these 'programmable atom equivalents' can be seen in Figure 4-5. Hydrophobic IONPs are coated with an amphiphilic polymer, poly(maleic anhydride-alt-octadecene) (PMAO) covalently modified to contain pendant azide groups (PMAO-N3). After purification from excess polymer, these particles can be conjugated to ssDNA containing a dibenzocyclooctyne (DBCO) group through a copper-free strain-promoted alkyne-azide cycloaddition (SpAAC) reaction with the azides on the IONP surface. Synthesizing these DNA-coated IONPs (DNA-IONPs) occurs in three steps – IONP coating with PMAO-N3, synthesis of DBCO-ssDNA, and conjugation of ssDNA to coated IONPs.

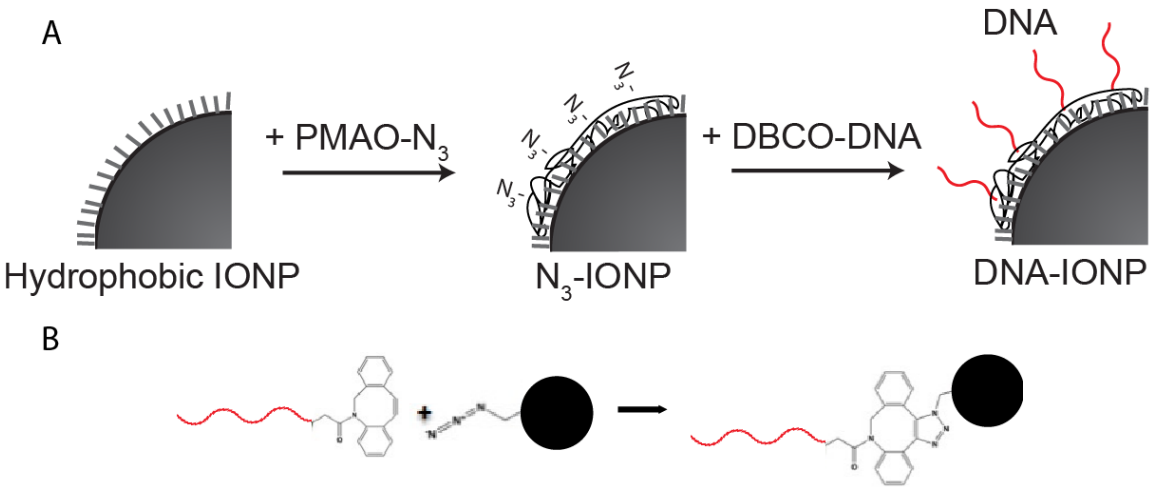

Figure 4-5. Scheme of DNA-IONP Synthesis A) Hydrophobic IONPs are mixed with azide-functionalized poly(maleic anhydride-octadecene) (PMAO-N_3) to create azide-coated IONPs, and then mixed with DBCO-modified DNA to create DNA-IONPs. B) Strain-promoted Azido-Alkyne Cycloaddition (SpAAC) reaction of DBCO-modified DNA and azide-functional IONPs leading to stable triazole formation.

IONP Coating

In order to coat IONPs with the reactive polymer, a thin film of IONPs and polymer is created by evaporating the solvent from a mixture of hydrophobic IONPs and polymer. Hydration of the film in an aqueous buffer using sonication produces polymer-coated IONPs (either single cores or aggregates) suspended in water. Ultracentrifugation of the crude mixture on a sucrose gradient produces 3 bands: a free polymer band visible under UV light (with ethidium bromide staining), a well-dispersed IONP band, and a pellet consisting of highly aggregated IONPs (Figure 4-6). AGE of IONPs extracted from this second band reveal a single product without excess polymer (seen with EtBr staining under UV light). Dynamic light scattering measurements show a single peak around 40 nm for 15 nm IONP cores, though sometimes a multi-modal peak distribution is apparent (with no impact of downstream DNA conjugation). The decrease in size following purification is likely due to the removal of the large aggregates and clusters during the purification process. Finally, negative-stain TEM imaging of the samples reveal well dispersed IONP crystals with a thin polymer shell surrounding them.

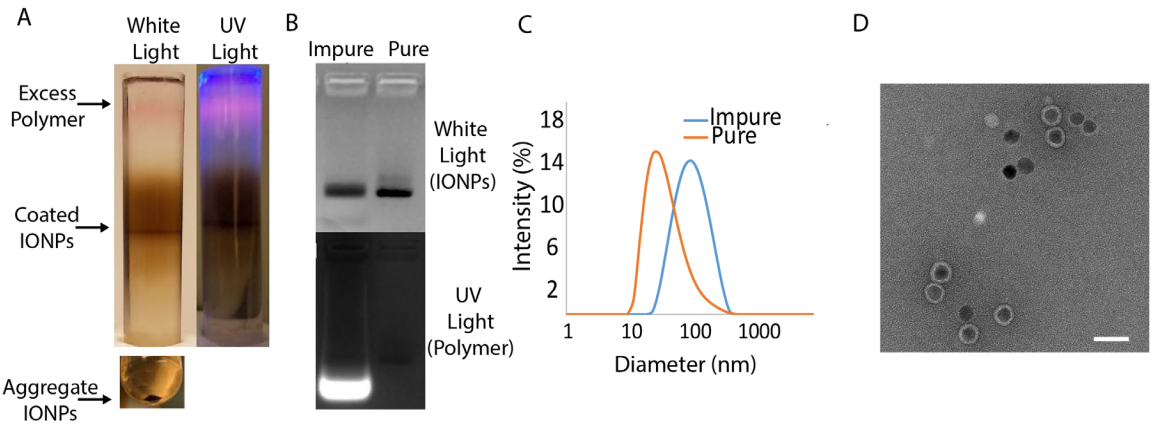

Figure 4-6. Characterization of Coated IONPs. A) Image of sucrose gradient ultracentrifugation columns under both white light and UV illumination showing the separation of free polymer from coated IONPs from aggregated IONPs. B) White light (top) and UV light (bottom) AGE of coated IONPs before and after sucrose gradient purification. C) Intensity-weighted size distribution of coated IONPs before and after sucrose gradient purification obtained via DLS. D) Negative-stain TEM image of coated IONPs after purification. Scale bar - 25 nm.

Further investigation into the coating process revealed several considerations. First, and most importantly, we found that the nature of the base solvent used during the coating procedure is critically important. The chloroform needs to be free of any polar species, so anhydrous chloroform stabilized with molecules other than ethanol is a necessity. Our initial attempts at coating using ethanol-stabilized chloroform produced large precipitates that would not resuspend in aqueous solutions (Figure 4-7), presumably due to the increased polarity of the solution adversely affecting the polarity-driven association of the hydrophobic polymer component and hydrocarbon ligands of the particles. Secondly, we observed that the underlying quality of the IONPs plays a significant role. We found that the same product obtained from the same company but in different lots produced particles which had significantly different coating yields, as evidenced by the banding during

ultracentrifugation purification. Additionally, we were unable to successfully coat 13 nm IONPs synthesized in-house. It is unclear exactly what differences in the particles leads to this change – based on conversations with the commercial supplier, the presence of excess ligands in the IONP solution could differ and thus purity of the particles could play a role in successful coating. Analysis of particles obtained from different bands within the sucrose gradient revealed that IONPs which migrate further in the column appear to be clustered together, as evidenced by slower electrophoretic mobility and TEM imaging. We tested variations in IONP concentration (50 nM vs 100 nM) and polymer excess (300, 450, and 600 monomer units/nm^2 IONP surface area) during coating in order to improve recovery yields - no differences were observed within the range of values tested (data not shown).

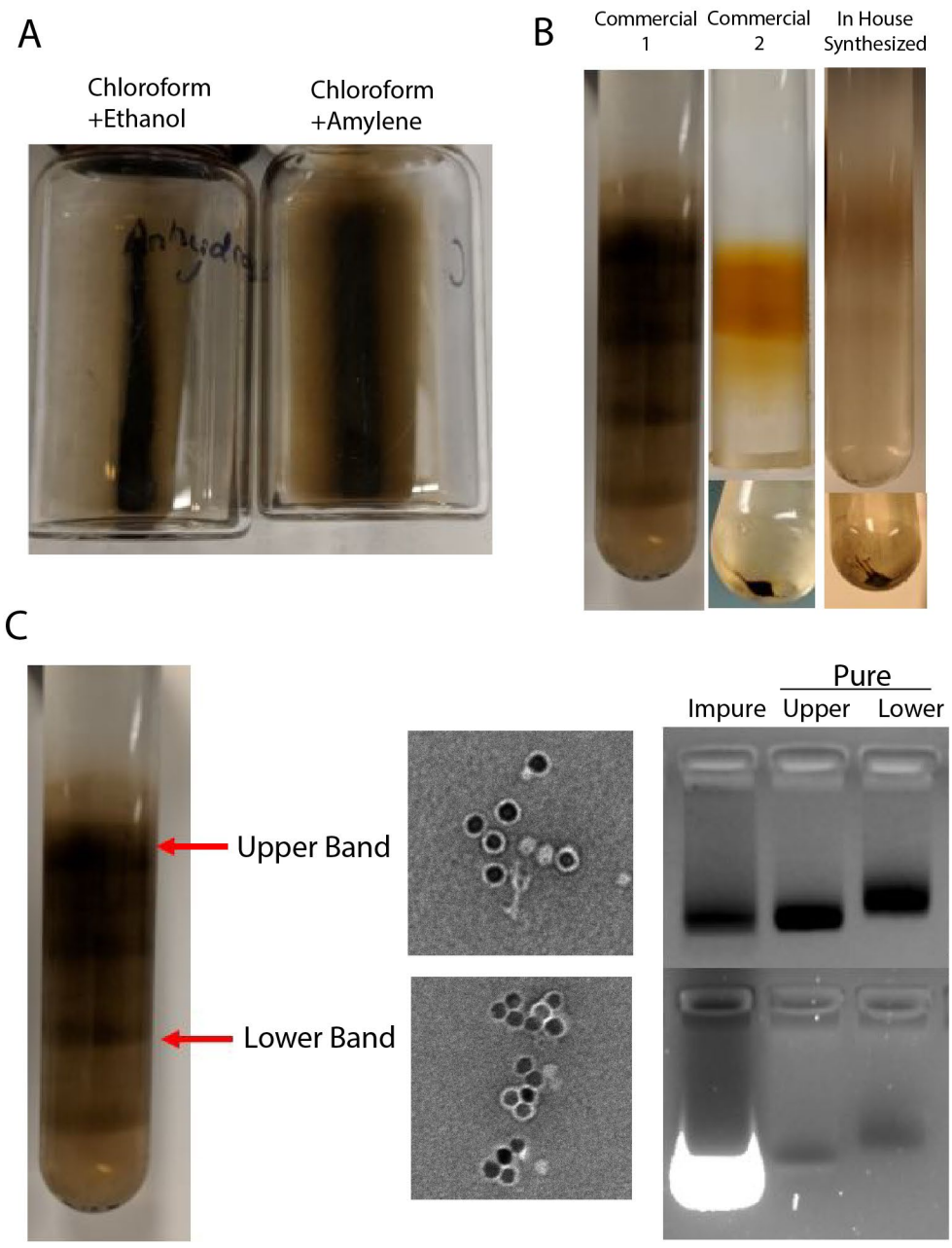

Figure 4-7. Troubleshooting of IONP Coating Procedure A) Images of IONP following coating in chloroform with two different stabilizing agents, showing aggregation in presence of ethanol. B) Image of sucrose gradient columns following ultracentrifugation of 3 different populations of coated IONPs, including commercial IONPs purchased from same company in different lots (Commercial 1 and 2) and IONP synthesized in-house. C) Image of sucrose gradient column (left), negative-stain TEM image (middle) and AGE (left, top - white light, bottom - UV light) showing differences in IONP populations recovered from different regions of sucrose gradient column.

DBCO-DNA Synthesis

The SPAAC click reaction used to attach ssDNA to the coated IONP surface necessitates the use of a strained alkyne group chemically conjugated to the ssDNA. Dibenzocyclooctyne (DBCO) is one such alkyne which is highly stable and participates in the cycloaddition reaction with high yield and fidelity. While commercially available DBCO-tagged DNA is available from suppliers like IDT, the DNA was very expensive. As such, we sought to synthesize this modified DNA ourselves using a reaction between amine-labeled DNA and DBCO-labeled reactive esters (Figure 4-8). We successfully used both N-hydroxysuccinimide (NHS) and Sulfo-2,3,5,6-tetrafluorophenol (STF) leaving groups in this reaction. While no clear differences in the quality of the final DBCO-DNA conjugate was observed between these two esters, the use of NHS-esters and a necessary DMSO-co-solvent did lead to the formation of a white precipitate during overnight reaction. In contrast, the increased hydrophilicity of the STF-DBCO ester allowed this reaction to be run entirely in aqueous solution without the need for DMSO and eliminated the formation of this precipitate. While the results shown are from experiments using of NHS esters, we recommend the use of STF-esters where possible just in case the precipitate we observed does have some effect for other sequences/applications.

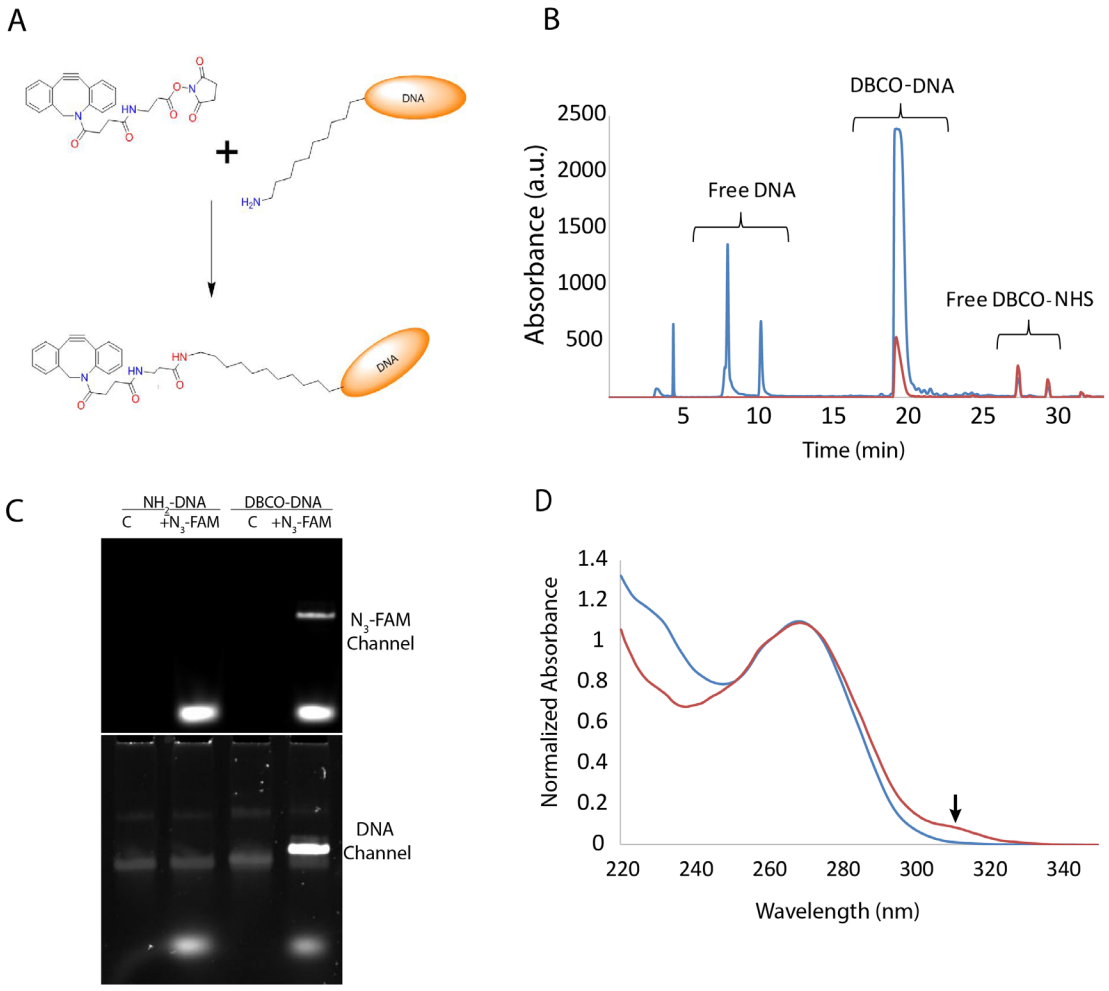

Figure 4-8. Synthesis of DBCO-modified DNA A) Schematic of reaction between activated DBCO-ester and amine-functionalized DNA. B) HPLC trace of eluent at different times monitored via absorbance at 260 nm (blue - DNA) and 309 nm (red - DBCO) showing separation of 3 different components. C) PAGE gel of amine-DNA (NH-DNA) and DBCO-DNA with and without the addition of azide-functionalized FAM fluorophore (N_3-FAM) without (top) and with (bottom) ethidium bromide staining for DNA. D) UV-Vis absorbance of amine-DNA (blue) and DBCO-DNA (red) showing characteristic DBCO peak at 309 nm.

Amine-terminated DNA and DBCO-ester were mixed with a 25-50-fold excess of DBCO to DNA and reacted in a solution containing PBS and sodium bicarbonate used to adjust the pH to optimize the amine-ester reaction. Depending on the ester used, the reaction mixture could be entirely aqueous, or 60% DMSO (High concentrations of DBCO-NHS precipitates at ratios lower than 60%). After an overnight reaction, the resulting product can then be purified by HPLC to remove free DBCO and unmodified DNA. Purification using ethyl acetate extraction and standard desalting was also sufficient – while this technique does not remove any unmodified DNA, we did not find that this hindered downstream reactions significantly. In one instance HPLC-purified DBCO-DNA appeared to work slightly better in IONP conjugation, but there were not significant enough differences to draw firm conclusions. If HPLC purification is available we would recommend using that: if not, the extraction/desalting technique works sufficiently and does not require any sophisticated equipment.

HPLC traces of the crude mixtures reveal the presence of three different populations: unmodified DNA strands which are eluted at early time points and only show up in the 260nm absorbance channel, DBCO-DNA which elute around 20 minutes and show both 260nm absorbance (characteristic of DNA) and 310 nm absorbance (characteristic of DBCO), and free DBCO esters, which elute much later with absorbance predominately at 310 nm. It is unclear why the unmodified DNA elutes as two separate peaks – one hypothesis is the formation of DNA dimers during solid phase synthesis, which has some supporting evidenced based on secondary bands during polyacrylamide gel electrophoresis (PAGE). To verify activity of the DBCO-DNA, the purified product was mixed with azide-functionalized fluorescein (N3-FAM). A PAGE gel of the resulting

products reveals the presence of a sharp band in the FAM channel only in the DBCO-DNA sample, corresponding to the successful reaction between a model azide and the DBCO-DNA. Finally, UV-Vis absorbance measurements of the DNA before and after conjugation with DBCO reveal the appearance of a shoulder at 310nm, which corresponds to attached DBCO.

DNA-IONP Synthesis

The protocol for conjugating DBCO-modified DNA to N3-PMAO-coated IONPs was based on the original publication by Chad Mirkin's lab and follows closely the protocols established for conjugating thiolated-ssDNA to the surface of gold nanoparticles. In both cases, the reactive nanoparticles are mixed with the reactive DNA at a sufficient excess and the reaction between the two is allowed to proceed overnight. Sodium chloride is subsequently added to slowly increase salt concentration – the so called 'salt-aging' process. High salt concentrations are beneficial for increasing the loading density of DNA onto the particle surface by shielding the electrostatic repulsion between neighboring DNA strands. However, unmodified particles are typically not stable in very high salt concentrations, and thus sodium chloride needs to be added gradually in order to preserve nanoparticle stability.

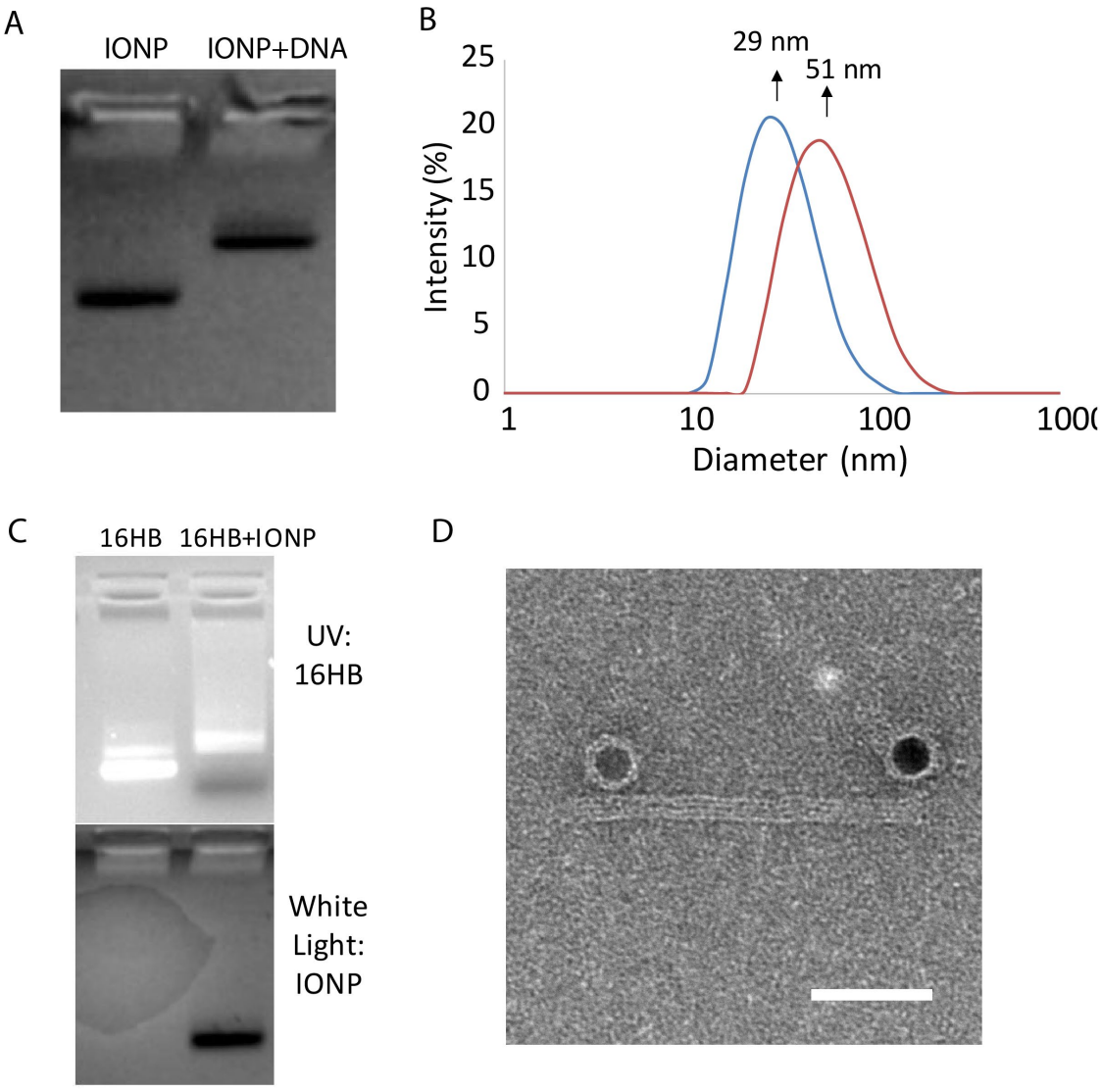

Figure 4-9. Characterization of DNA-modified IONPs A) White light AGE of coated IONP before and after reaction with DBCO-DNA. B) Intensity-weighted size distribution of coated IONPs before (blue) and after (red) reaction with DBCO-DNA. C) UV (top) and white light (bottom) AGE of DNA-IONPs mixed with 16HB bearing complementary capture strands. D) Negative-stain TEM image of DNA-IONPs bound to 16HB with 2 binding sites at either end. Scale bar – 50 nm.

The resulting DNA-IONP conjugates were characterized using agarose gel electrophoresis and dynamic light scattering. Following conjugation, the particles exhibited a sharp decrease in mobility consistent with increased size (Figure 4-9). Furthermore, a large shift in the hydrodynamic size was observed following DNA conjugation using DLS. Most importantly, we were able to successfully attach DNA-IONPs to 16HB DNA origami bearing complementary 'capture' sequences, as observed by both a shift in gel electrophoretic mobility and via TEM imaging. As synthesis of these particles had already been published, we did not spend much effort further characterizing or optimizing the synthesis. We did however investigate the effect of the final sodium chloride concentration reached during the salt aging process. We found that while increases in sodium concentration beyond 100mM did not have an observable effect on agarose gel mobility (Figure 4-10) or hydrodynamic size (data not shown) of the resulting DNA-IONPs, differences in DNA loading density became readily apparent while attempting to attach DNA-IONPs to the 16HBs in buffer containing magnesium. DNA-IONPs synthesized with final sodium chloride concentrations of less than 500mM lost stability in 10mM magnesium, leading to changes in 16HB mobility as well as smearing of free DNA-IONPs. It should also be noted that this reaction was very finicky – we found that different batches of IONPs or DBCO-DNA would occasionally produce lower quality conjugates, as observed by smearing on gel electrophoresis and poor quality of 16HB-IONP products. 'Repurifying' PMAO-IONPs to remove excess polymer using centrifugation typically helped, as well as increasing the ratio of DNA:IONP. We also found that conjugation reactions were not successful in 1mL volumes. Due to this, conjugation reactions were always run in 100-200uL volumes.

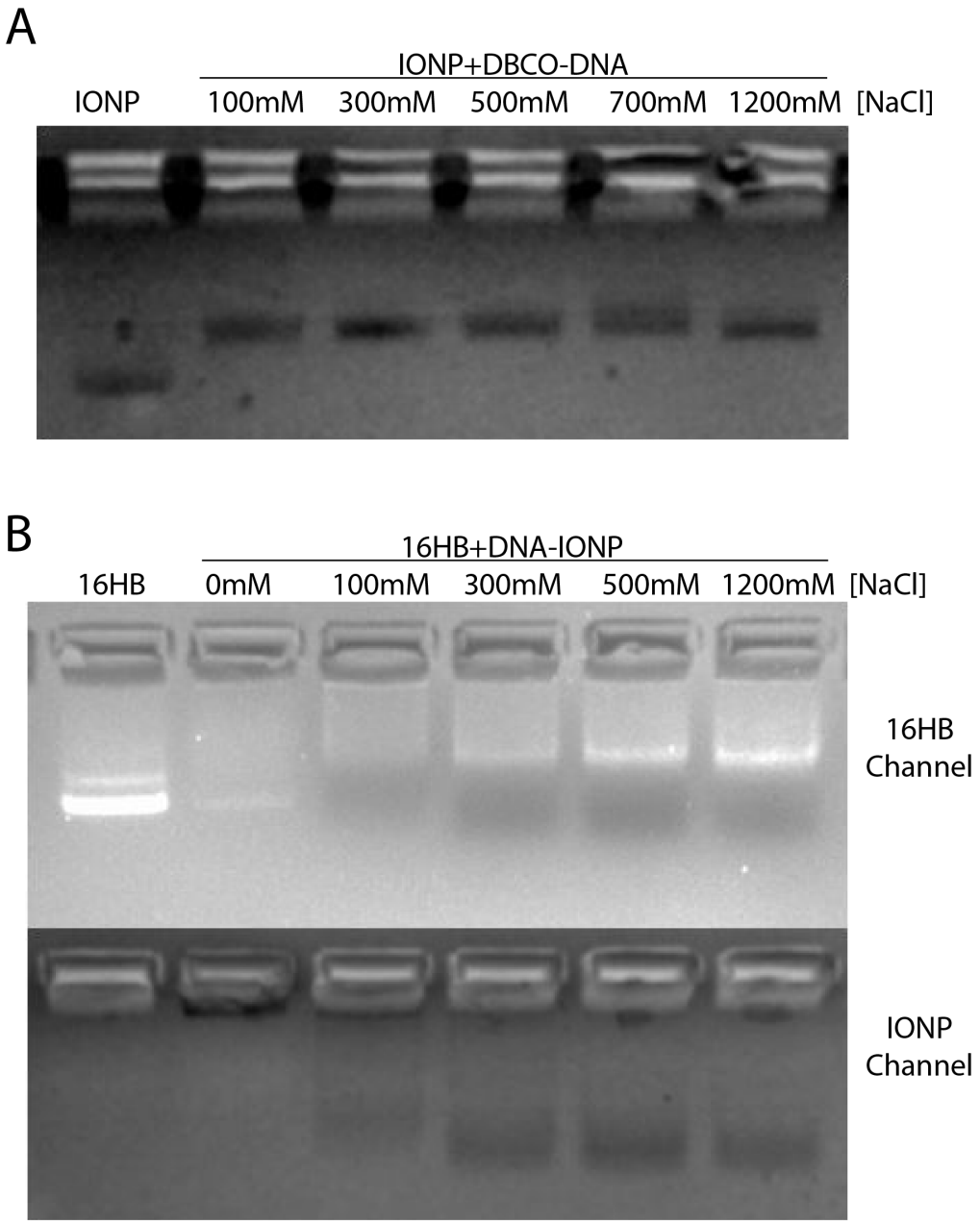

Figure 4-10. Effect of NaCl Titration on DNA-IONP Synthesis A) AGE (white light) of coated IONPs after reaction with DNA with the NaCl titration step stopped at different NaCl concentrations. B) UV (top) and white light (bottom) AGE images of 16HB with complementary capture sequences mixed with DNA-IONPs synthesized with different NaCl titration steps.

4.4.1.3 16HB-IONP Binding

In order to attach IONPs to our 16HB, we needed to find some way to engineer strong interactions between the DNA origami rod and the IONPs. Traditionally there are two main methods used to incorporate heteroelements: the use of streptavidin (STV)-biotin interactions and the use of complementary DNA hybridization. For STV-biotin interactions, binding of STV-modified heteroelements to biotin-labeled DNA strands on the DNA origami structure enable docking of the heteroelements to the prescribed location of the modified DNA (Figure 4-11). Commercial biotin-labeled ssDNA is easily obtainable, making this a popular choice for systems in which heteroelements can be readily conjugated to streptavidin. Core staple strands can be modified with biotin directly, or staple strands can contain ssDNA extensions which can hybridize to a separate biotinylated strand. While the first option produces more stable systems, the second is cheaper, as only one modified strand for all designs needs to be purchased. For complementary DNA hybridization, heteroelements conjugated to ssDNA 'cargo' strands can be attached to DNA origami structures in which staples have been extended with a complementary 'capture' DNA. This option is generally preferable for several reasons: no modified oligos need to be purchased for the DNA origami structure, so designs can be potentially cheaper, and different heteroelement populations can be attached to the same structure using multiple orthogonal cargo/capture DNA sequence pairs. In both cases, the spatial organization of the heteroelements is determined by the specific location at which the interacting element (either biotin or capture strand) is located. Careful choice in which staples contain these modifications allows for the precise control over heteroelement number, spacing, and geometric organization.

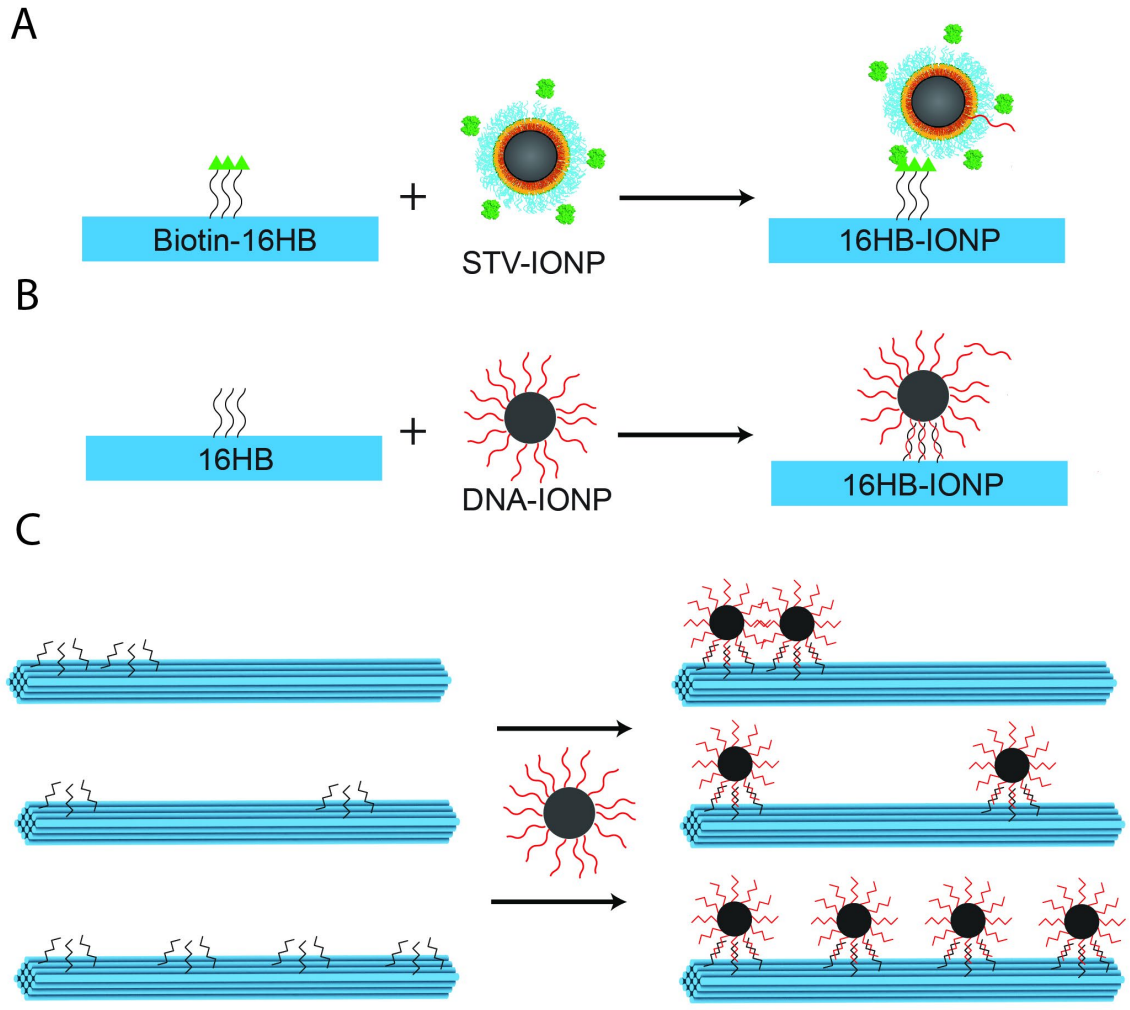

Figure 4-11. IONP-16HB Binding Schematic. Two different techniques were investigated for interfacing IONPs with the 16HB. A) Biotin-streptavidin interactions, in which streptavidin-modified IONPs bind to biotinylated DNA sequences on the 16HB. B) Capture-cargo DNA hybridization, where DNA-modified IONPs bind to complementary ssDNA extensions on the 16HB C) Spatial organization of IONPs is controlled by the location of ssDNA or biotin extensions from select staples on the 16HB.

The 16HB rod contains 36 staples on each face with break points amenable to modification with either a biotinylated strand or a capture sequence. We subdivided these 36 strands in 12 groups of 3, to provide a total of 48 possible binding sites (12 per face) for attaching IONPs. The nomenclature for identifying variant designs included the number of binding sites (16HB1, 16HB2, 16HB3 for 1, 2 and 3 binding sites), along with the position of each binding site labeled from 1-12 (i.e. 16HB2(1,12) refers to a design with two binding sites at positions 1 and 12). We chose 3 strands per binding site due to previous work demonstrating that multiple tethers per site increase binding yields[166]. We tested both streptavidin-biotin and complementary DNA binding strategies – either STV- or DNA-modified IONPs were mixed with corresponding 16HB structures and allowed to incubate under variable conditions. Successful binding was verified using agarose gel electrophoresis, due to a shift in 16HB mobility following attachment of IONPs, and TEM imaging of gel-purified structures. TEM imaging in particular allowed for precise interrogation of the binding process, as statistics on the number and spacing of IONPs on single 16HBs could be identified. In order to study the effect of various parameters on IONP binding efficiency, individual 16HBs were binned based on the number of bound IONPs or whether or not the 16HB were bridged by IONPs to form dimers or aggregates (Figure 4-12). 16HBs which were clearly damaged were omitted from these measurements. This allowed us to track which assembly conditions could optimize yields by maximizing the number of 16HBs with the correctly bound IONPs.

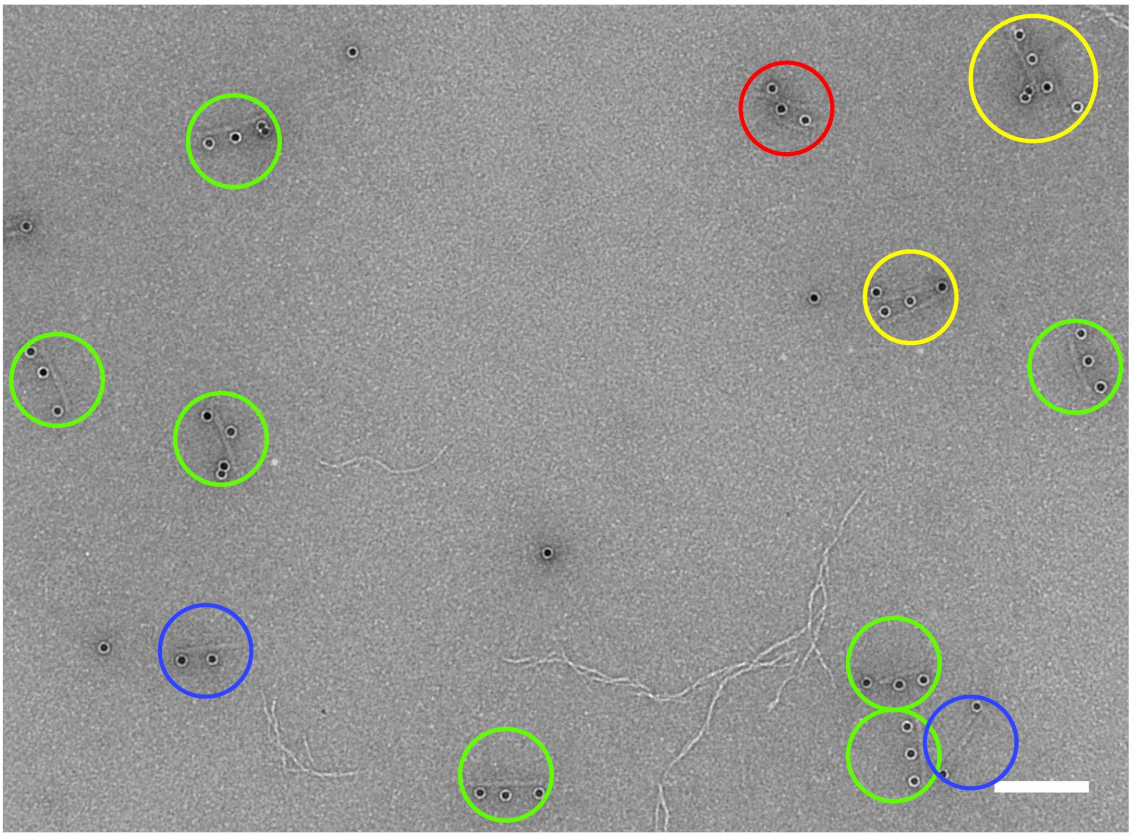

Figure 4-12. TEM Image of 16HB3+IONP Binning. To calculate binding statistics, TEM images were analyzed and each 16HB was binned to either correct structures (green), structures with fewer IONPs than designed (blue), and 16HB that had formed dimers/aggregates (yellow). Structures that were clearly broken (red) were omitted from the analysis. Scale bar - 200 nm

Streptavidin-IONP 16HB Binding

We first used commercially-available STV-modified IONPs with a diameter of 10 nm, as the availability of these particles made it easy to start with. Through this initial work, we also found that the quality of commercially available particles can be highly variable, and thus it is critical to verify the fidelity of materials received from outside sources. Our initial attempts to attach STV-IONPs to biotin-modified 16HB were unsuccessful and subsequent analysis revealed issues with the particles themselves, as determined by a lack of binding to biotin-modified surfaces (data not shown). We also found that the presence of excess free STV was highly variable in these purchased products, and thus purification via centrifugation and resuspension in fresh buffer was needed.

Using this system, we were able to verify STV-IONP binding and elucidate various factors that affected this binding. Incubation of 16HBs bearing biotinylated strands at either 1 or 3 binding sites led to significant reduction in the mobility of 16HB as monitored by gel electrophoresis (Figure 4-13). The relative mobility change per heteroelements number was significantly larger for these STV-IONPs than other heteroelements used in lab, such as gold nanoparticles and subsequent DNA-modified IONPs, which we attribute to the surface charge of the particles relative to DNA-coated particles. TEM imaging of purified 16HB3(1,6,12) samples revealed 16HB with attached IONPs in a mixed population containing origami structures bound to 1-3 IONPs and present in dimer or aggregate assemblies. Statistical analysis of these populations allowed us to track various assembly parameters to identify which produced the highest yield of correct structures – in the case of 16HB3(1,6,12) designs, those 16HBs bound to exactly 3 particles. First, we were able to show that the number of biotinylated strands at each binding location had a significant

impact, with binding yields much higher with 3 tethers per site compared to 1. This matches previous work with other nanoparticle heteroelements and is likely due to a combination of redundancy in protecting against binding site strand defects as well as increased binding cooperativity. We found that the ratio of IONPs per binding site added into the reaction also played a role, with excesses greater than 1-fold necessary for higher yields. Based on this data, it is unclear if there is much difference between higher-excesses (5x vs 20x) as this experiment was not repeated using this system. We also tested the sequence dependence of biotinylated-strands attached to the 16HB, finding that there was little to no difference based on DNA length. However, in all of these studies the yields were very low and highly variable, with the highest observed efficiency around 30%. This poor quality led us to pursue other avenues.

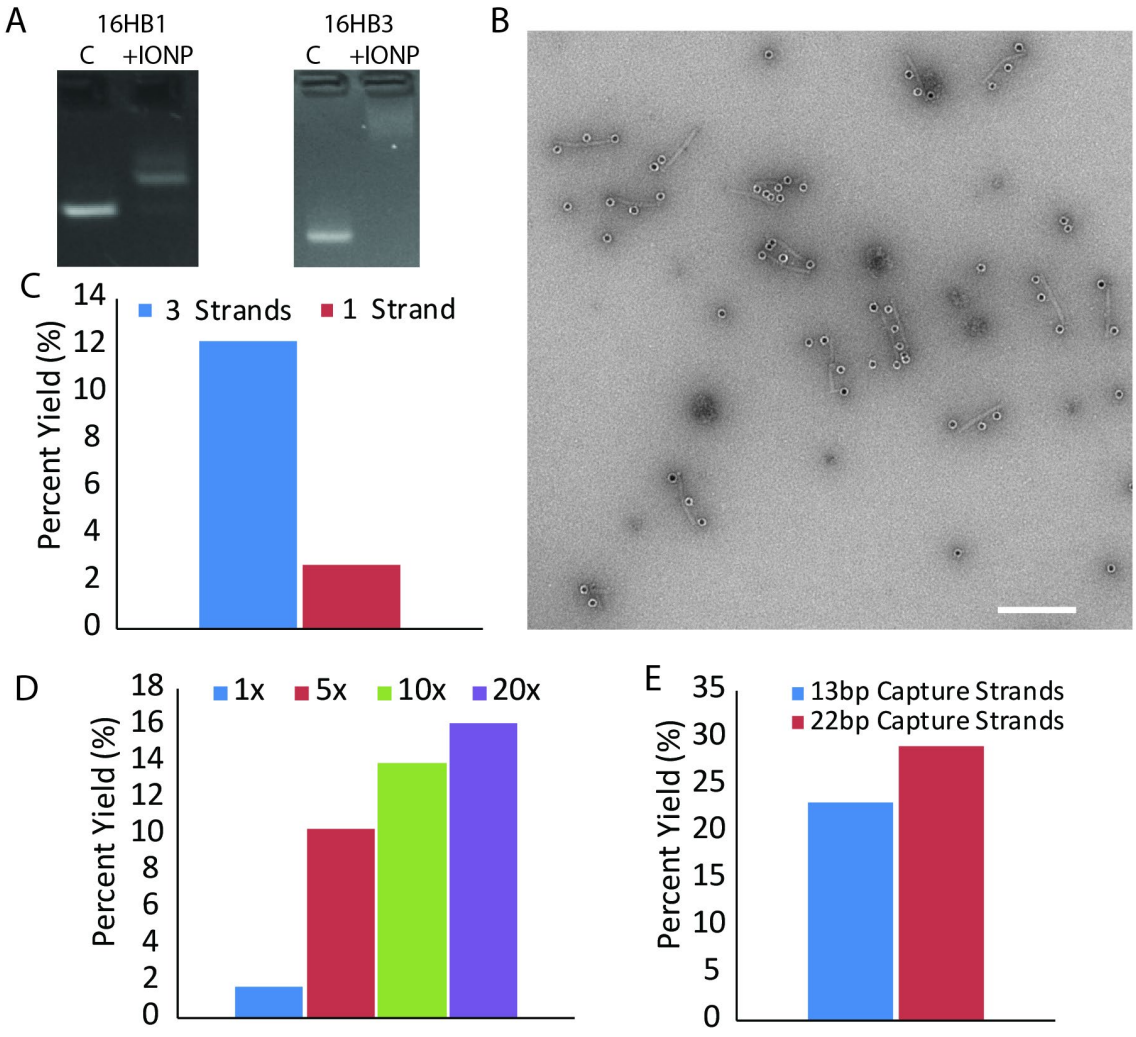

Figure 4-13. Commercial STV-IONP Binding Analysis. A) AGE images of 16HB with either 1 (left) or 3 (right) biotinylated sites before and after incubation with STV-IONPs. B) Representative TEM image of purified 16HB+STV-IONP conjugates. Scale bar - 200 nm C) Calculation of 16HB3-IONP yields on 16HB with either 3 (blue) or 1 (red) strands per binding site. D) Calculation of 16HB3-IONP yields with different ratios of IONP:16HB binding sites. E) Calculation of 16HB3-IONP yields with different capture sequence design, showing maximum yield achieved.

We next tried STV-IONPs produced in house (by Sheng Tong in the Bao lab), with the thought that these particles might be of higher quality and therefore show better binding characteristics. These 8-nm particles were synthesized by introducing reactive groups during the polymer coating process and subsequent bioconjugation strategies to attach streptavidin molecules to this coating. We were able to verify binding of these particles to 16HBs bearing biotin-groups using both agarose gel electrophoresis and TEM images (Figure 4-14). However, the quality and purity of the conjugates produced were relatively poor, as electrophoresis revealed the presence of multiple species within the populations as seen by smearing and extra band formation. TEM imaging also revealed significant heterogeneity and poor fidelity in the final constructs (data shown for 16HB4, but other designs had similar quality). While additional experiments showed that the binding was highly conserved across many different conditions, including rapid binding in as fast as 15 minutes and significant binding with only 1-fold excess of IONPs (data not shown), the quality of the assemblies did not ever improve. Based on both of these attempts, we decided to move away from utilizing biotin-streptavidin interactions to create the 16HB-IONP conjugated and instead moved towards using DNA-coated IONPs.

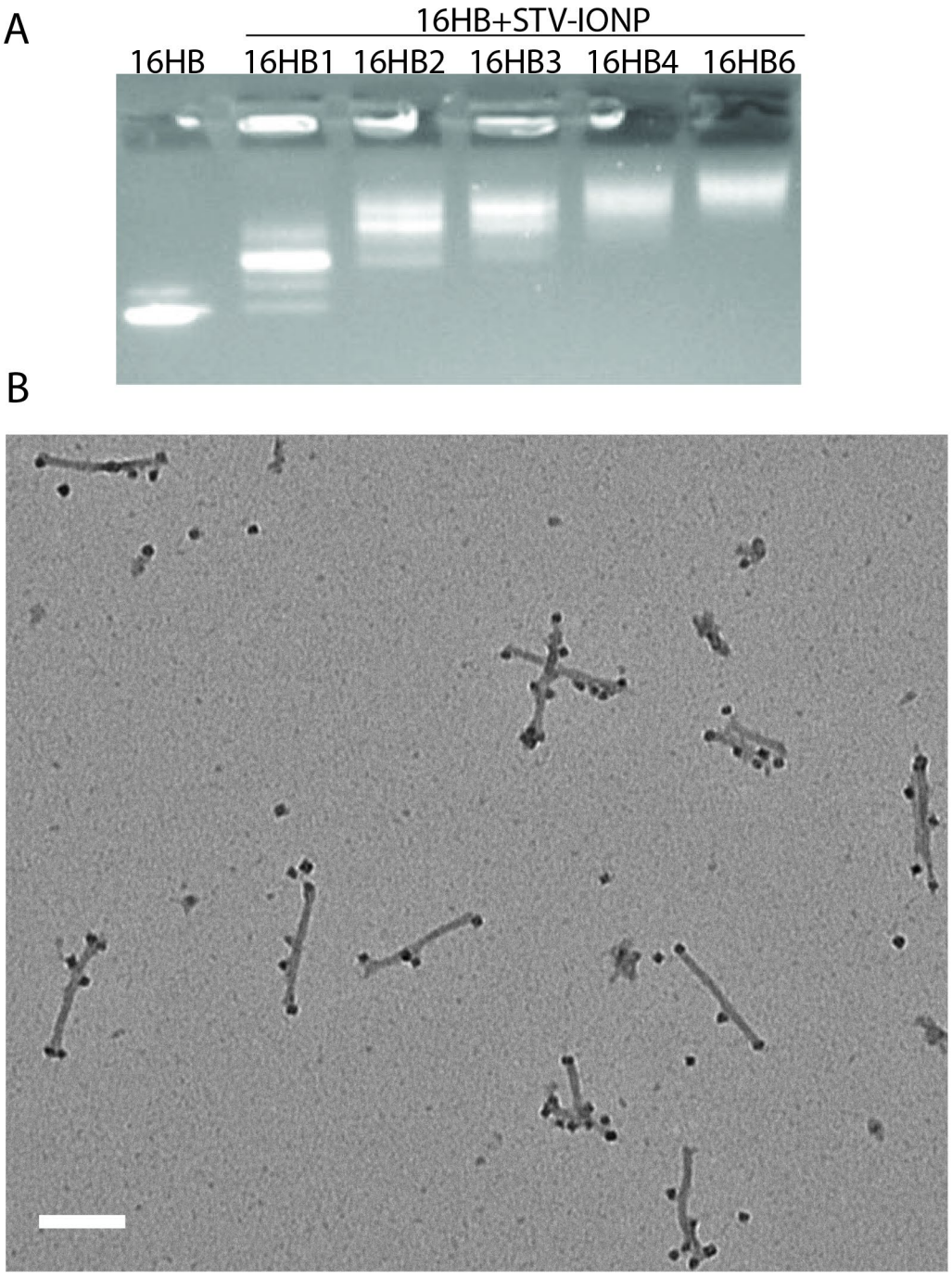

Figure 4-14. Synthesized STV-IONP Binding Analysis. A) AGE image showing 16HB with different numbers of biotinylated binding sites after incubation with STV-IONPs. B) Representative TEM image of 16HB3+STV-IONP. Scale bar - 100 nm.

DNA-IONP 16HB Binding

We used the method developed by Chad Mirkin's lab for creating 'Programmable Atom Equivalents' to synthesize IONPs coated with a dense player of DNA that showed excellent stability and homogeneity. Mixing these DNA-IONPs with 16HBs bearing complementary 'capture' staple extensions led to the formation of 16HB-IONP conjugates through hybridization-based interactions. We first assembled 10 nm DNA-IONPs synthesized by collaborators onto 16HB3(1,6,12) and found that these constructs displayed sharp bands with decreased mobility on agarose gel electrophoresis with significantly higher binding fidelity (>60% yields) based on TEM images relative to STV-IONPs (Figure 4-15).

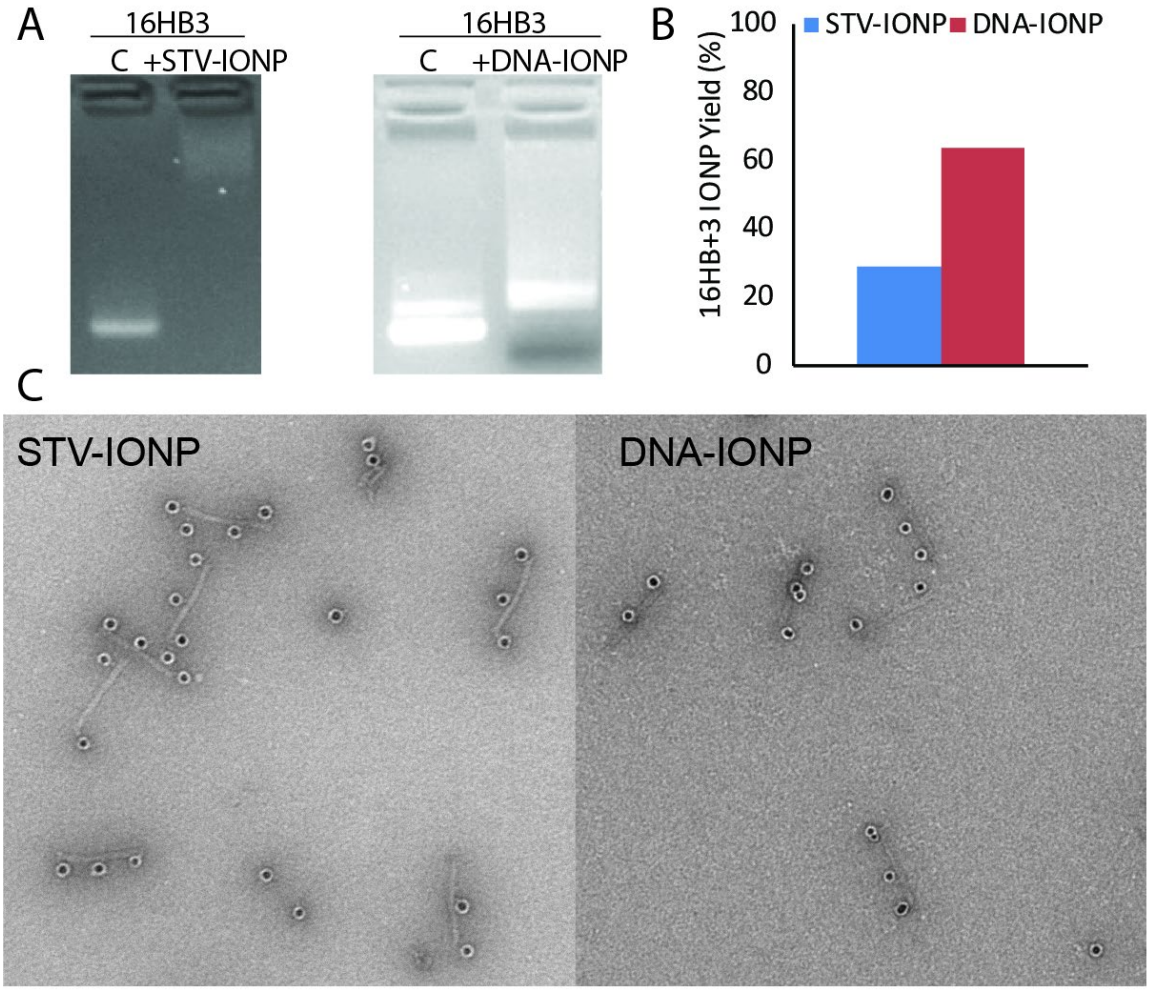

Figure 4-15. Binding Yields of DNA-IONPs Versus STV-IONPs A) AGE images of 16HB3 before and after incubation with STV-IONP (left) or DNA-IONP (right). B) Calculated yields of 16HB3-IONP with either STV-IONP (blue) or DNA-IONP (red). C) Representative TEM image of 16HB3 with either DNA-IONP or STV-IONP.

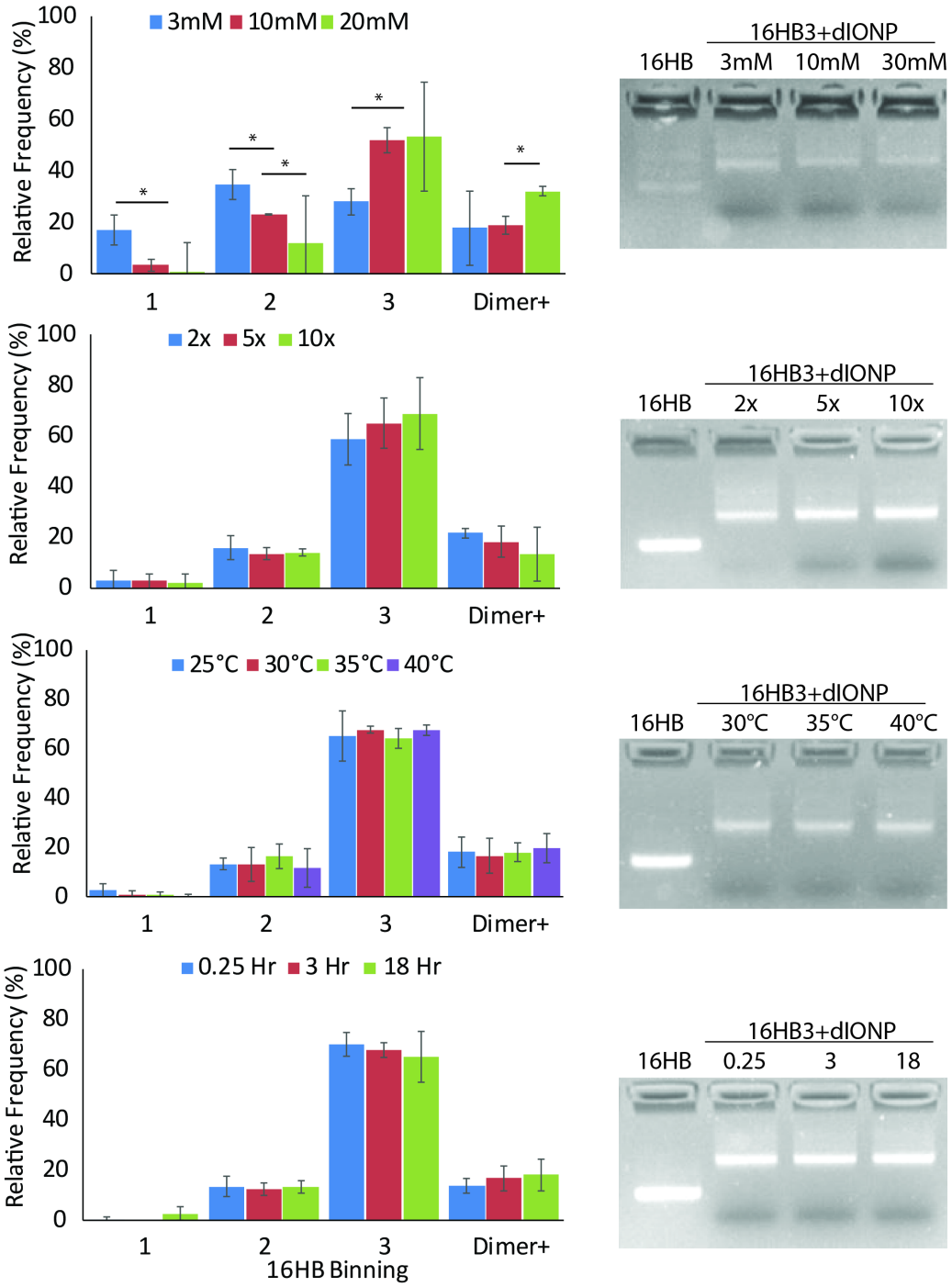

Figure 4-16. Optimizing Binding of DNA-IONP to 16HB3. Calculated binding yields of 16HB3+DNA-IONP (left) and AGE images of 16HB before and after IONP incubation (right) under a variety of conditions. A) Different magnesium concentrations B) Different IONP:16HB-binding-site ratios C) Different temperatures D) Kinetics of IONP binding. N=3, mean ± s.d. *p<.05

We next sought to optimize IONP binding fidelity - 15 nm DNA-IONPs were mixed with 16HB3(1,6,12) under a variety of conditions and gel electrophoresis and TEM imaging were used to quantify binding yields (Figure 4-16). In general, we found that the binding reaction is highly robust over the conditions tested, with binding happening rapidly (within 15 minutes), occurring with high efficiency even at low IONP fold-excesses (2x), and maintaining yields over a range of temperatures (25°C to 40°C). We did find that magnesium concentrations during the binding reaction play a role – an increase in 16HB with fewer than 3 particles were observed as magnesium concentrations dropped. This matches data obtained with other systems[166] and is likely due to enhanced electrostatic repulsion between DNA-IONPs and 16HB without sufficient cation screening. However, higher Mg concentrations also led to enhanced dimer and aggregate formation. Other experiments were conducted with 10-nm particles and showed similar results. In general, there was a decent amount of heterogeneity between samples which makes drawing narrow conclusions from these studies challenging – since the experiments were not repeated due to IONP shortages, the data is not presented here. The observed variability could come from several sources: the underlying binding reaction itself, damage to structures/IONP binding during gel purification and/or TEM grid preparation, or potentially other factors we have not thought of. Additionally, there is a chance this data overestimates total yields as images were collected from gel purified samples – while every effort was made to cut out all observable bands from the gel, there could be free 16HB or larger aggregates which were not retained and thus excluded from these statistics. We also were curious to see how close these IONPs could be placed together before steric/electrostatic effects limited

binding. We used a 16HB2 system with the 2 binding sites spaced at various distances and measured yields for both 15nm and 10nm IONPs, finding that binding yields dropped when 15 nm IONPs were placed closer than 45 nm (Figure 4-17). The use of smaller particles did enable closer spacing to be achieved, though a drop in binding yields closer 35 nm was still observed for 10-nm particles (data not shown) - it is possible to pack smaller particles closer together using this system, but there is a practical limit to how close particles can get before yields drop too severely.

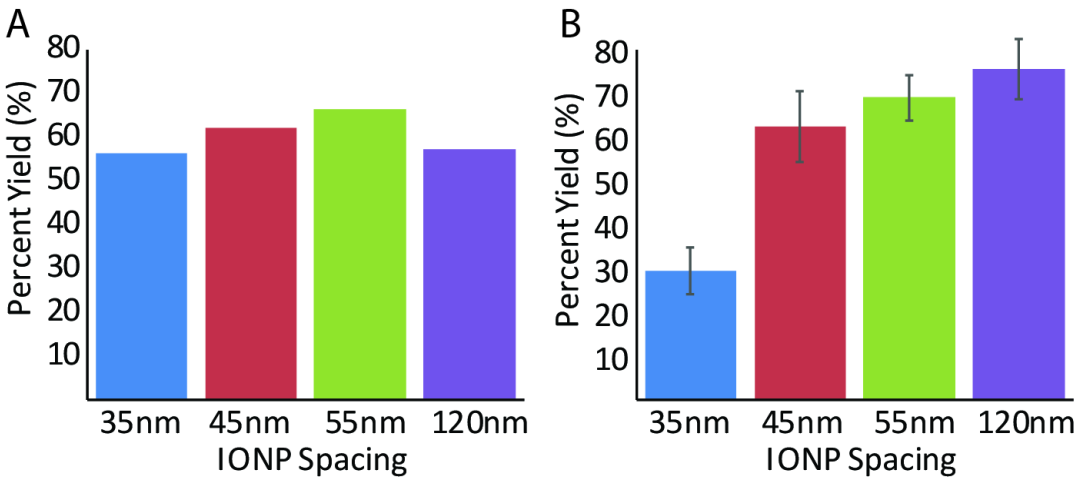

Figure 4-17. Binding Yields of 16HB2 with Different Spacing. Binding yields of 16HB2 with different IONP spacing A) 10 nm IONPs, B) 15 nm IONPs. N=3, mean ± s.d.

With this improved system, we sought to demonstrate precise control over IONP spatial organization. We designed numerous 16HB variants with different numbers of binding sites maintaining a constant spacing between each site. We were able to successfully bind up to 4 particles with a constant ~35nm spacing using both 10 nm and 15 nm particles, as well as bind up to 3 particles with a 55nm spacing (Figure 4-18). As the number of bound particles increased, the mobility shift observed in AGE also increased. We then designed a 16HB with extensions on all 12 binding sites on one face to determine maximum binding of 10 nm IONPs. We found that that between 4-5 IONPs could be attached – this limitation is likely due to both steric and electrostatic repulsion between IONP as well as the bridging of a single IONP across multiple binding sites (Figure 4-19). For the 15nm particles, we altered the 16HB design to contain 6 alternating binding sites spread across all 4 faces of the rod, giving a theoretical maximum of 24 possible binding sites. We found that the maximum number of 15 nm IONPs that could be attached using this method was between around 9-10 IONPs (Figure 4-20).

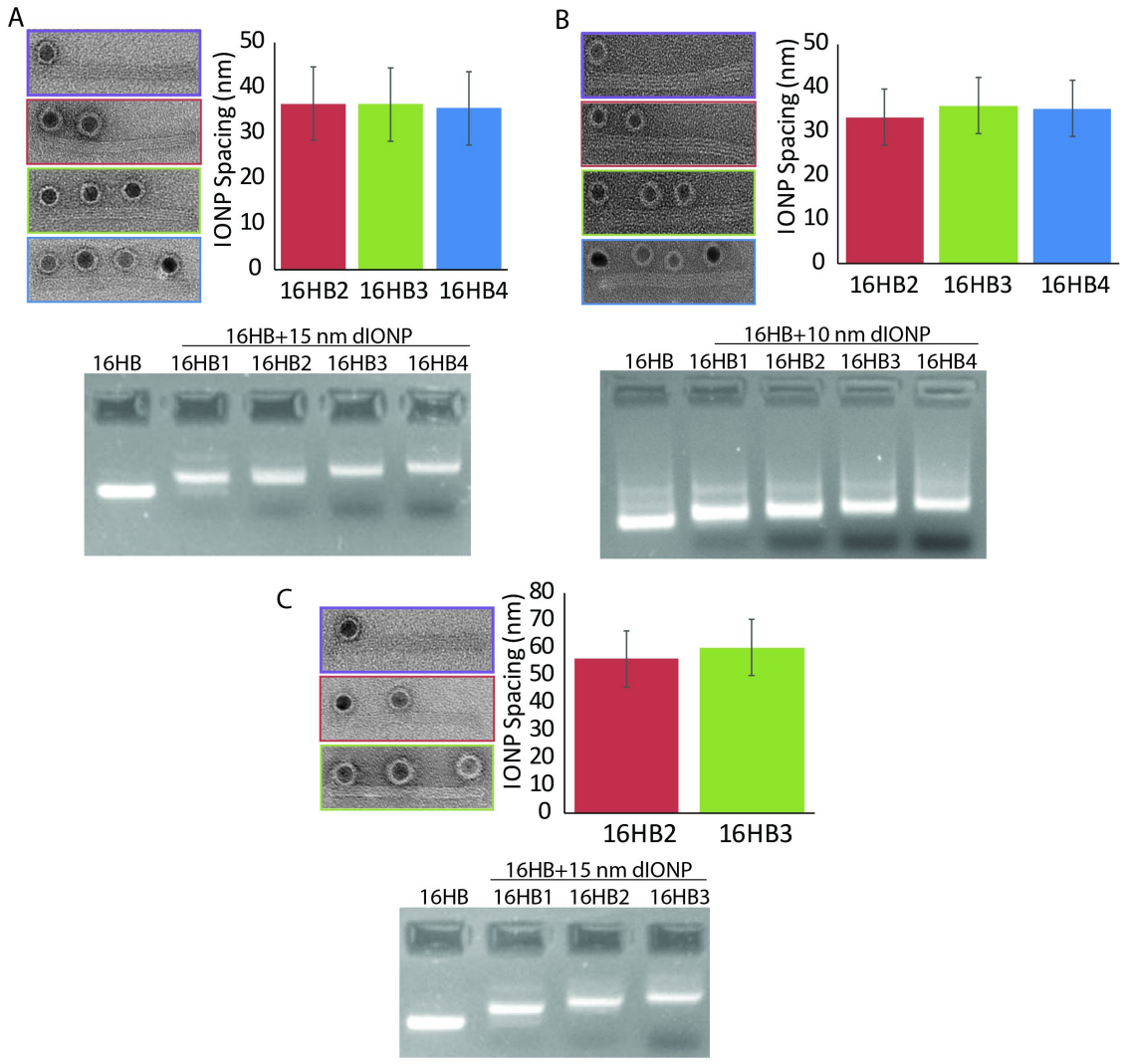

Figure 4-18. Control of IONP Number. Representative TEM images (left), measurements of center-to-center distance between IONPs (right) and AGE of different 16HB before and after IONP incubation. A) 15 nm IONPs with ~35 nm spacing B) 10 nm IONPs with ~35 nm spacing C) 15 nm IONPs with ~55nm spacing. N>100, mean ± s.d.

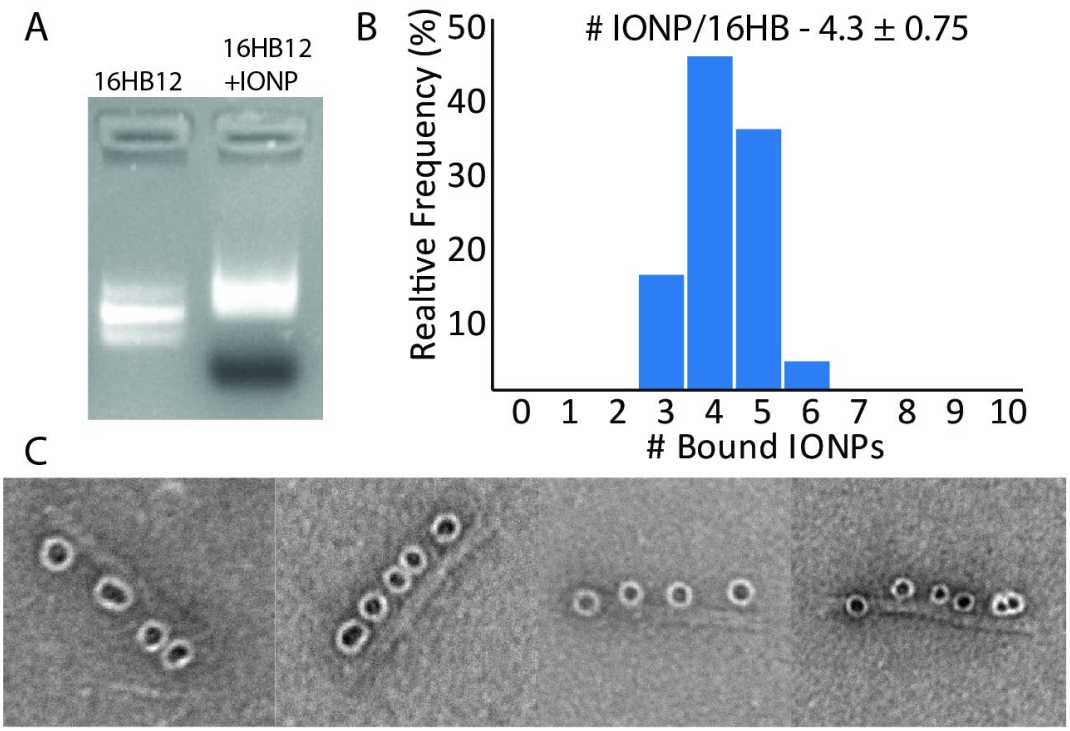

Figure 4-19. Saturated Binding on 1 Face with 10 nm IONPs. A) AGE of 16HB12 with and without addition of 10 nm DNA-IONPs B) Frequency distribution of 16HB12 based on number of bound IONPs. C) Representative TEM images of 16HB12+10 nm DNA-IONPs.

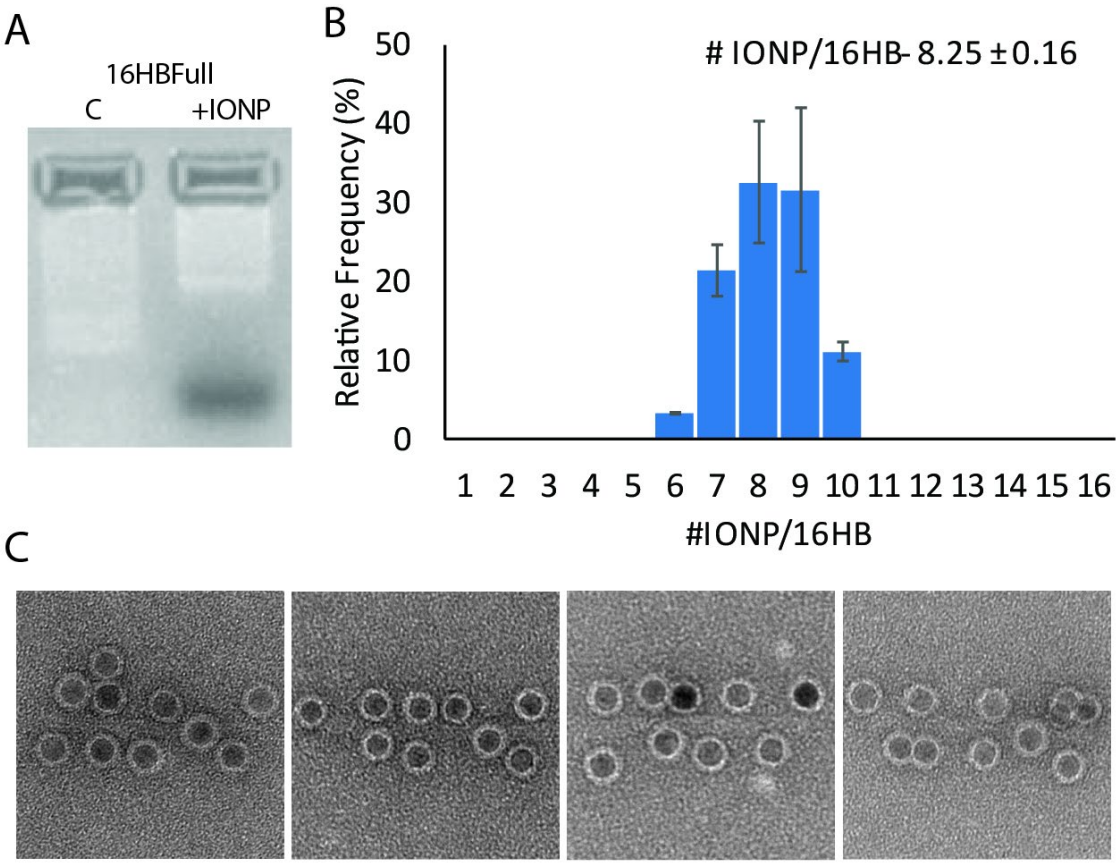

Figure 4-20 Saturated Binding on 4 Faces with 15 nm IONPs A) AGE of 16HB-Full with and without addition of 15 nm DNA-IONPs B) Frequency distribution of 16HB12 based on number of bound IONPs. C) Representative TEM images of 16HB12+10 nm DNA-IONPs. N=3, mean ± s.d.

We then wanted to demonstrate that we could maintain a constant number of IONPs while varying the spacing between particles. We designed 16HB variants in which the spacing between binding sites was varied. We found that the spacing between 2 DNA-IONPs could be tuned between ~20 nm and ~120 nm with ~10 nm spacing using both 10 nm and 15 nm IONPs, and that the center-to-center spacing between IONPs was identical regardless of IONP using the same 16HB2 design (Figure 4-21). One thing that is interesting is the variability of the spacing within each design, as measurements had standard deviations of around 8-12 nm. This could be due to general flexibility in the dsDNA tethers holding the IONP, the fact that each binding site consists of 3 strands spaced over a set area and particle location within that area can be variable, as well as measurement error.

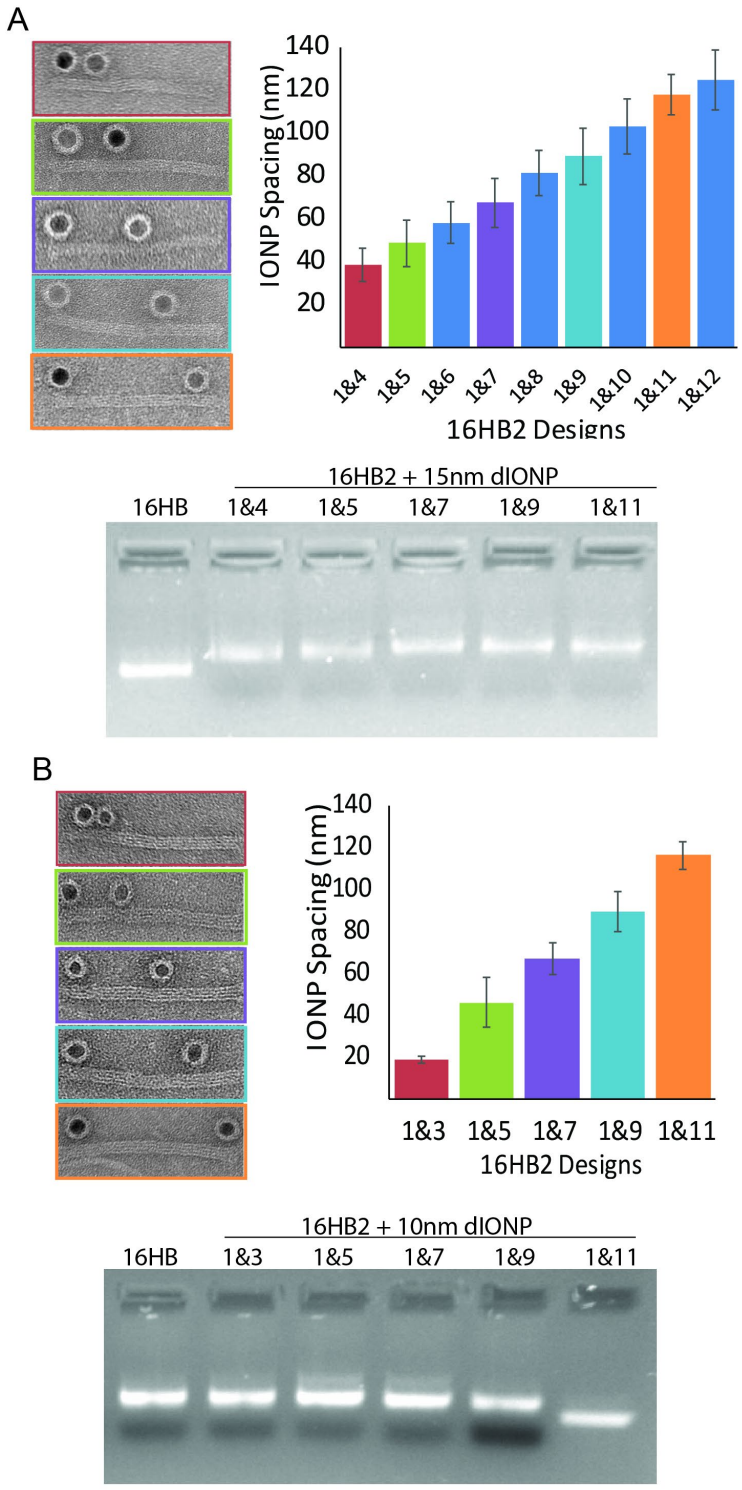

Figure 4-21. Control of IONP Spacing. Representative TEM images (left), measurements of center-to-center distance between IONPs (right) and AGE of different 16HB designs with 2 binding sites before and after IONP incubation A) 15 nm IONPs B) 10 nm IONPs. N>100, mean ± s.d.

The yields obtained in this work are lower than those obtained with other nanoparticle systems. For example, Takabayashi et al found ~97% binding yields for 10-nm gold particles attached to a DNA origami rod [166] - these yields are comparable to our own work using gold nanoparticles. It is not entirely clear why yields with our DNA-IONPs are considerably lower – one likely cause is the increased complexity of the nanoparticle due to the presence of the hydrophobic ligands and amphiphilic polymer. There is a chance that these extra layers might inhibit or complicate binding to complementary DNA sequences, though at this point this is mere speculation. The use of this polymer layer also limits the inter-particle spacing that can be achieved compared to gold particles as the hydrodynamic diameter of the IONPs is larger relative to their core diameter. Regardless, the results presented here represent a significant improvement over previous studies that have attempted to pattern the assembly of IONPs. Rafati et al decorated DNA origami nanotubes with IONPs, but the authors did not demonstrate any modulation over the number and spacing of the IONPs[161]. Ryu et al were able to control the number of IONPs bound to a single dsDNA using Zinc-finger binding proteins – however, their system produced clusters with much higher polydispersity and they did not demonstrate any ability to modulate inter-particle distances[109].

4.4.1.4 16HB-IONP Purification

In order to measure the effect of IONP spatial organization on T_2, excess IONPs used during assembly need to be removed. As such, we needed to develop a method for purifying the assembled IONP-16HB from the free IONPs before conducing the measurements. Purification using gel electrophoresis is the typical method used for purifying excess heteroelements and works well for small-scale purifications used for

studies such as binding yield analysis. However, a large quantity of sample (~1mL of 1-2nM 16HB) is needed for NMR measurements, and gel electrophoresis has neither the throughput nor the yield to be sufficient for this kind of preparation. We investigated the use of PEG precipitation as a method for removing excess IONPs, but free IONPs also pelleted in the same conditions as the 16HB (data not shown). Other techniques, such as ultracentrifugation and ultrafiltration, are also insufficient due to the large size of the IONPs. We tried using size exclusion chromatography, but this technique proved to be very challenging and time consuming (data not shown). Finally, we used a modified version of a technique first reported by Shaw et al in which magnetic beads are used to separate bound origami structures from free heteroelements[171]. Due to concerns regarding the use of magnetic beads and magnetic nanoparticles, we altered the technique to use non-magnetic polymeric beads.

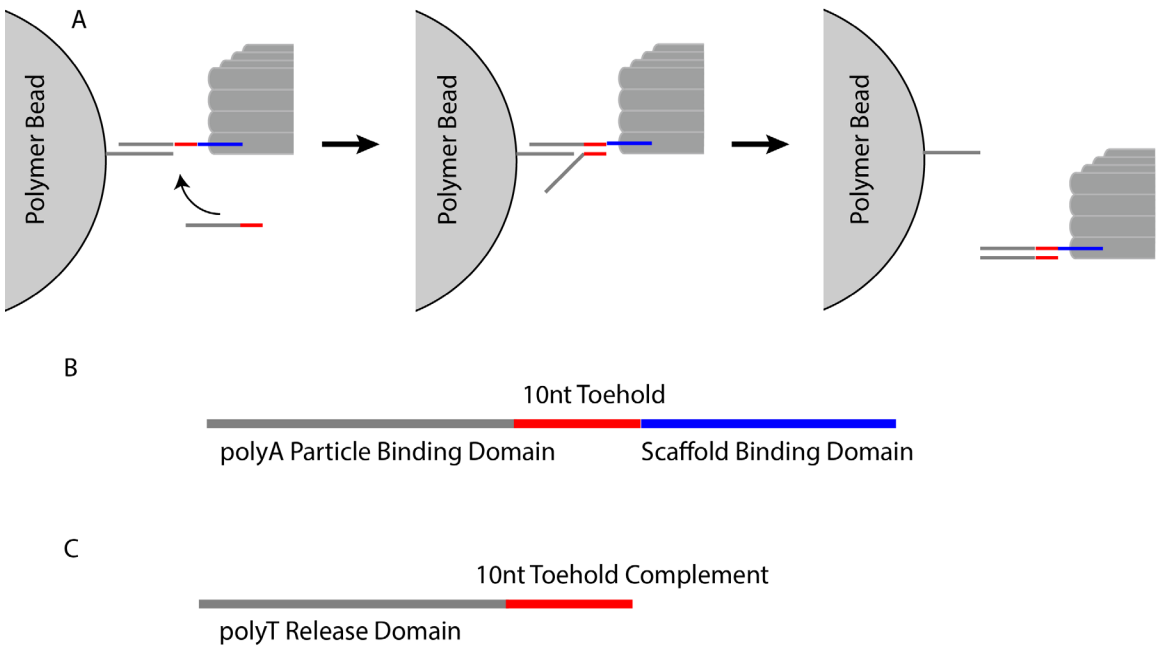

Figure 4-22 Schematic of Bead Pulldown Purification Method. A) Method for release of 16HB from polymeric beads where 16HB is initially bound (left) and addition of a release strand binds to available toehold (middle) with subsequent branch migration displacing 16HB from bead (right). B) General design of anchoring strand, containing a polyA particle binding domain (grey), a 10-nt toehold region (red) and a domain complementary to DNA origami scaffold (blue). C) General design of release strand, containing 10-nt toehold complement (red) and polyT release domain (grey).

In this technique, DNA origami structures contain a sacrificial 'anchoring' strand which can hybridize to DNA-functionalized micron-sized polymer beads (Figure 4-22). These polymer beads could then be isolated from particles in solution through low-speed centrifugation, leading to the formation of a pellet consisting of DNA origami/polymer beads. Species without an anchor DNA strand (i.e. all unbound heteroelements) are left in the supernatant and can be removed. Repeated washing/pelleting steps can be conducted in order to remove a large portion of free heteroelements. The second step involves the release of the captured DNA origami-heteroelement conjugates from the polymer beads

through the use of a strand displacement reaction. The anchoring strand contains 3 different domains – a scaffold binding domain, a particle binding domain, and a single-stranded toehold domain. A 'releasing' strand is then designed with a sequence complementary to both the toe-hold domain and the particle binding domain. Hybridization of the release strand to the anchoring strand via the toe-hold domain subsequently leads to strand displacement via a branch migration process and a release of the DNA origami from the polymer beads. A final pelleting step is then used to isolate the free polymer beads from the released DNA origami conjugates, which can then be collected. We designed an anchoring strand to contain a scaffold-binding domain complementary to free scaffold loops on the ends of the 16HB, a 10-nt toe-hold domain, and a 25bp particle binding domain, along with a release strand containing a 10-nt toehold complement domain and a domain identical to the sequence on the polymer beads. We made use of commercial polymeric beads designed for use in purifying mRNA from cell lysate via hybridization to the polyA caps of mRNA – thus, our particle binding domain was a polyA sequence complementary to the polyT on the polymeric beads, and our release strand consisted of a polyT sequence.

In a traditional experimental set-up, 16HB (with and without bound IONPs) were incubated with polymer beads, washed several times, and then released. In order to quantify recovery yields using this method, aliquots from the first supernatant (S) and the released mixture (R) were run on an agarose gel alongside an aliquot of the original solution and the relative intensity of each band could then be compared in order to estimate relative concentrations. Thus, yields were calculated as the percent of the original concentration that was in each aliquot. It should be noted that calculations of yields in this matter are only

semi-quantitative, and thus the numbers presented represent a general overview of the efficiency of recovery and differences between similar numbers are likely meaningless. Furthermore, the recovered quantities in both the supernatant and release aliquots rarely added up to 100%, which implies that some portion of structures remained bound to the beads even after addition of the releasing strand. Whether this is due to non-specific binding or incomplete strand-displacement reactions is not known.

Initial studies were conducted using cellulose-based polymeric beads. Unfortunately, significant non-specific binding of DNA in the presence of magnesium was observed, and thus yields of recovered 16HB structures was very low (data not shown). We then tried polystyrene-based beads, which showed significantly less non-specific binding and thus higher yield of recovery. We investigated the efficacy of the release step under different conditions using free 16HB and found that 37°C and at least 2 hours of incubation was required for sufficient release and subsequent recovery (75-100% recovery yields) (Figure 4-23). These limitations are likely due to the kinetics of the strand displacement reaction, which must reach completion in order for the 16HB to be released. By varying the number of polyA anchoring strands between 0 and 4, we were able to verify that the presence of anchor strands is required for purification, and that further increases in the number of strands leads to both higher initial binding (fewer 16HB in supernatant) but also less efficient particle recovery (fewer 16HB in release aliquot). We also found that the concentration of magnesium during binding and release had minimal effect on recovered yields, which imply that cation-mediated non-specific binding is likely not an issue leading to the low yields.

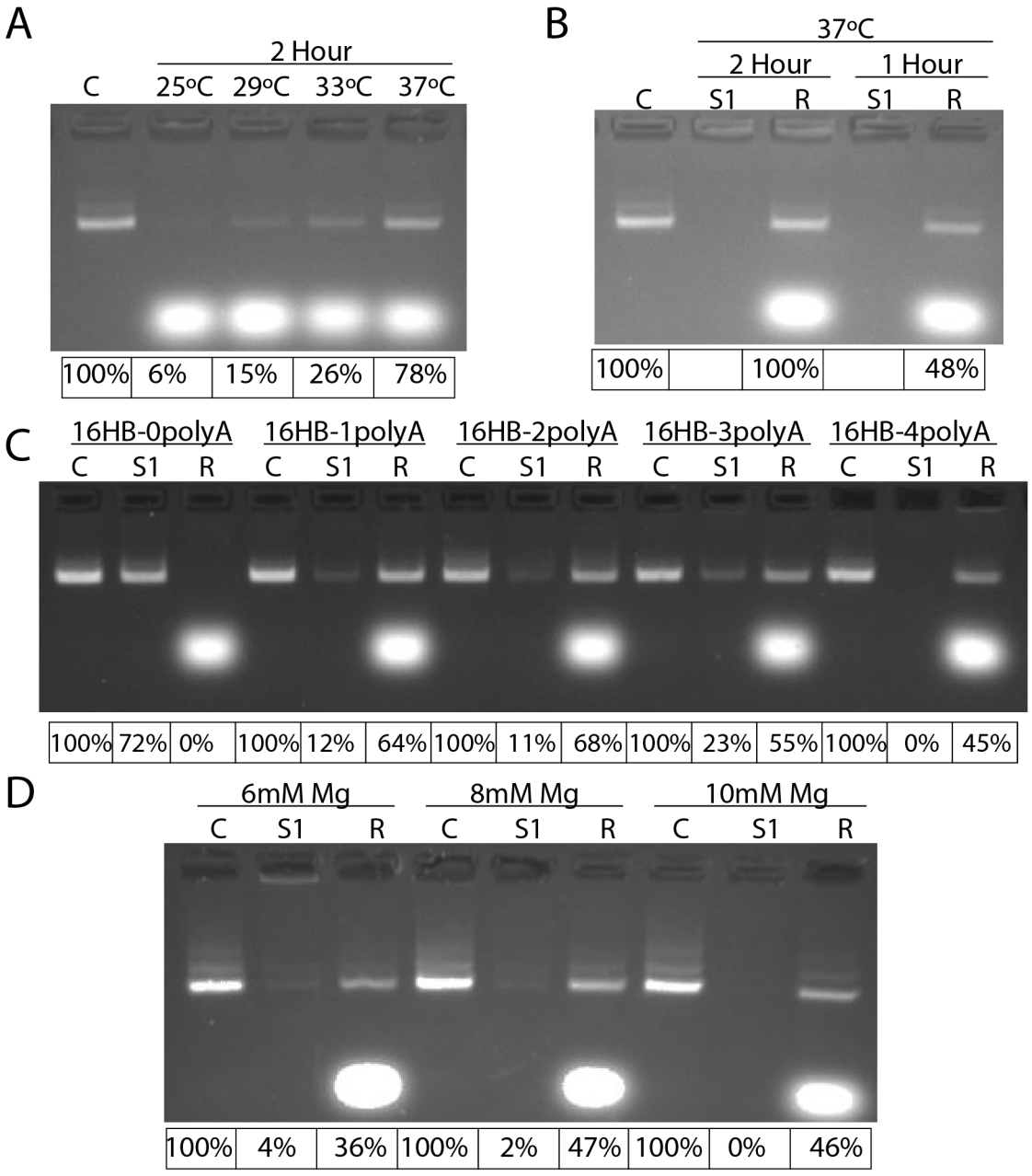

Figure 4-23. Factors Affecting 16HB Release from Polymer Beads. AGE of 16HB binding and recovery from polymeric beads along with band intensity analysis to estimate relative yields. C - Control, stock 16HB solution, S1 - Supernatant from first wash step, R - Supernatant following 16HB release. A) Only release supernatant after 2 hours at different temperatures B) Release kinetics at 37 °C C) Titration of the number of polyA anchor strands from 0 to 4 D) Effect of magnesium concentration during release step.

After initial tests using free 16HB were conducted, we then turned to testing to see how well 16HB bound with IONPs could be purified using this method. While initial attempts were successful, we did find that yields with particles were lower than yields without particles. More importantly, we found that the position and number of IONPs attached had a significant effect on the recovery yields from purification (Figure 4-24). Yields were practically non-existent when attempting to purify 16HB bound to 3 IONPs. Furthermore, yields also decreased when IONPs were placed closer to the site of 16HB-bead binding and the strand displacement reaction (site 1 vs site 6). Based on these results, why hypothesize that steric effects from local IONPs hinders the strand displacement reaction from occurring.

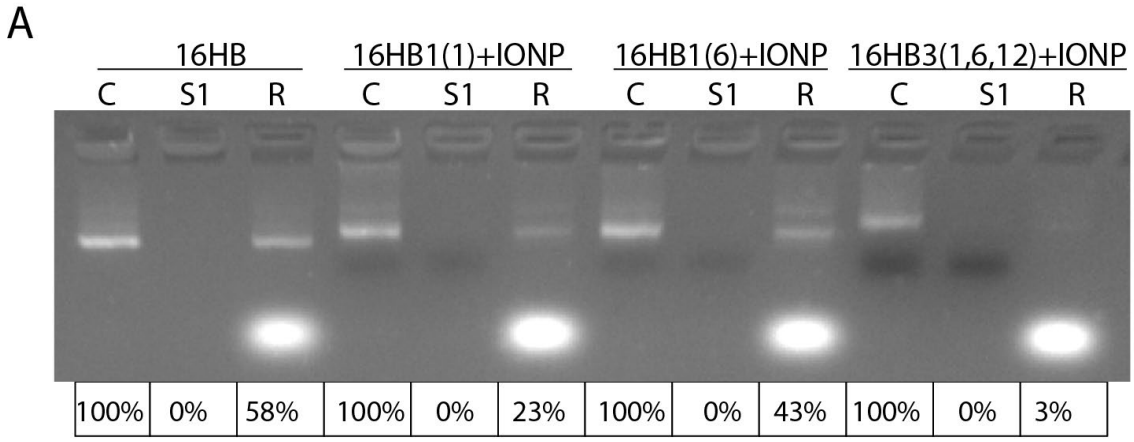

Figure 4-24. Effect of IONP Placement on 16HB Recovery - 25pA Binding. AGE of 16HB binding and recovery from polymeric beads along with band intensity analysis to estimate relative yields. C - Control, stock 16HB solution, S1 - Supernatant from first wash step, R - Supernatant following 16HB release. 16HB designs with different binding locations for IONPs were tested.

We next investigated other anchor-strand designs in order to see if a new strategy could lead to higher recoveries of 16HB bound with higher numbers of IONPs. We first investigated decreasing the length of the polyA domain of the anchor strand, with the hypothesis that shorter domains would lead to higher yields. In particular, we chose lengths with estimated melting temperatures in between the temperature used for binding (25°C) and the temperature used for release (37°C): 13-nt (30°C), 14-nt (34°C), and 15-nt (36.5°C). We also tried putting either 2 or 4 copies of the 25pA binding domain on the remaining free scaffold loop protruding from the middle of the structure. When testing free 16HB, we found that all the shorter domains gave comparable yields with high binding, while full length domains on the free scaffold loop had lower binding efficiency and slightly worse release efficiency (Figure 4-25). During these experiments, we also noticed that the beads were sticking to the side of the tubes and sample was lost during pipetting. In order to remedy this, we started using the 1xFoB10 buffer supplemented with 0.01% Pluronic-F-127 in an effort to minimize non-specific binding to the tube, which led to a further improvement in yield. Since the new mechanism for release using the 13-nt polyA binding domains was theorized to be based on temperature induced melting rather than strand displacement, we conducted an experiment in which 16HB release was monitored both with and without the addition of release strands. We found that while some release does occur without the presence of release strands, consistent with thermally-induced DNA melting, the use of release strands did still have a significant effect. We hypothesize this is due to release-strand/anchor strand binding that occurs immediately upon removal of the sample from the oven but prior to centrifugation, which could prevent rebinding of 16HB to beads and thus improve yields.

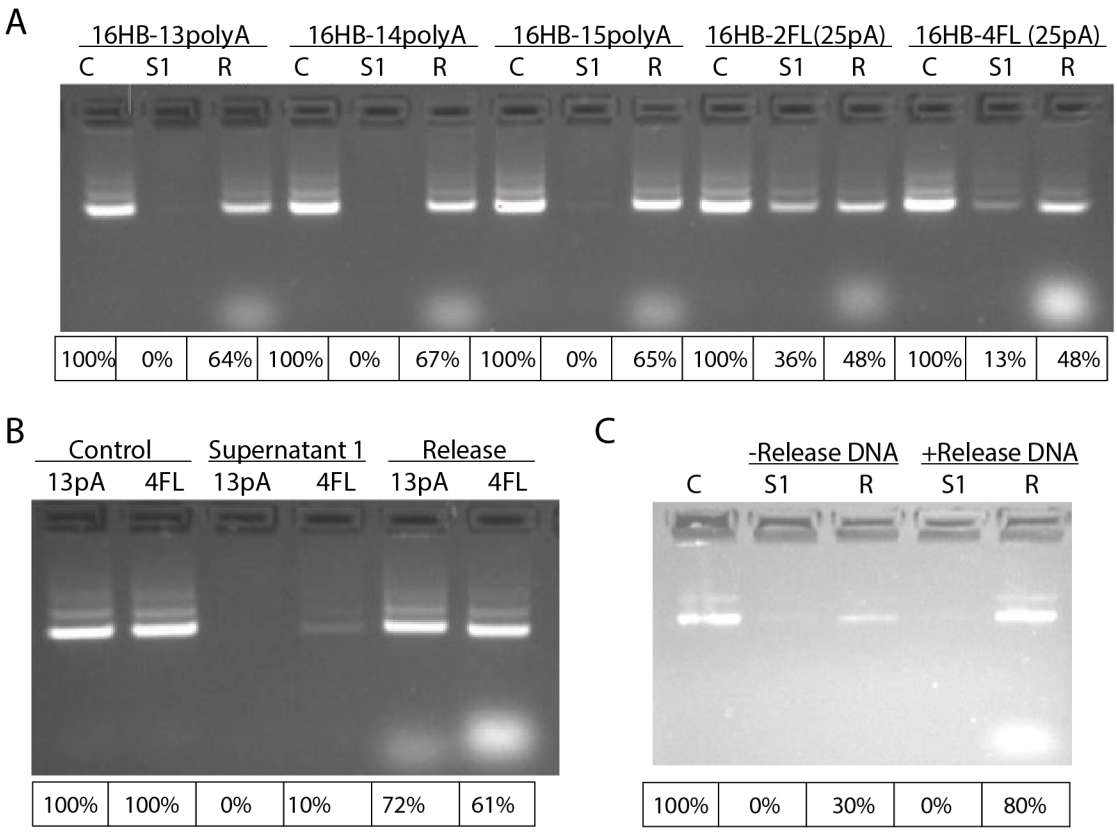

Figure 4-25. New Anchor Strand Design for 16HB Recovery. AGE of 16HB binding and recovery from polymeric beads along with band intensity analysis to estimate relative yields. C - Control, stock 16HB solution, S1 - Supernatant from first wash step, R - Supernatant following 16HB release. A) Recovery of 16HB from polymer beads using different anchor strand designs, including different length polyA domains or anchor domains attached to free scaffold loop (FL). B) Recovery of 16HB with two different anchor strand designs in the presence of Pluronic F-127. C) Recovery of 16HB using 13pA anchor design with and without the use of release strand.

Based on these results, we moved forward with using the 13-nt polyA binding domain located on the free scaffold loops at the end of the 16HB. We tested this new design with 16HB bound to a wide range of particles and found that reasonable recovery yields (>50%) could be obtained with all designs, including structures with IONP bound adjacent to anchor strands and structures with large numbers of IONPs (16HB12, with ~4-6 IONPs) (Figure 4-26). It should be noted that large scale purification using this bead pulldown method (I.e. 200uL at 1.5nM) does induce some degree of aggregation/dimerization of 16HB's relative to gel purification, with around 20-25% of 16HBs found to be in some higher-order network. This is compared to aggregate yields in the 5-10% range for gel purified structures. We hypothesize that this is due to the significant concentration of 16HB-IONP constructs that occurs during the pelleting procedure, which could be leading to enhanced inter-structure interactions.

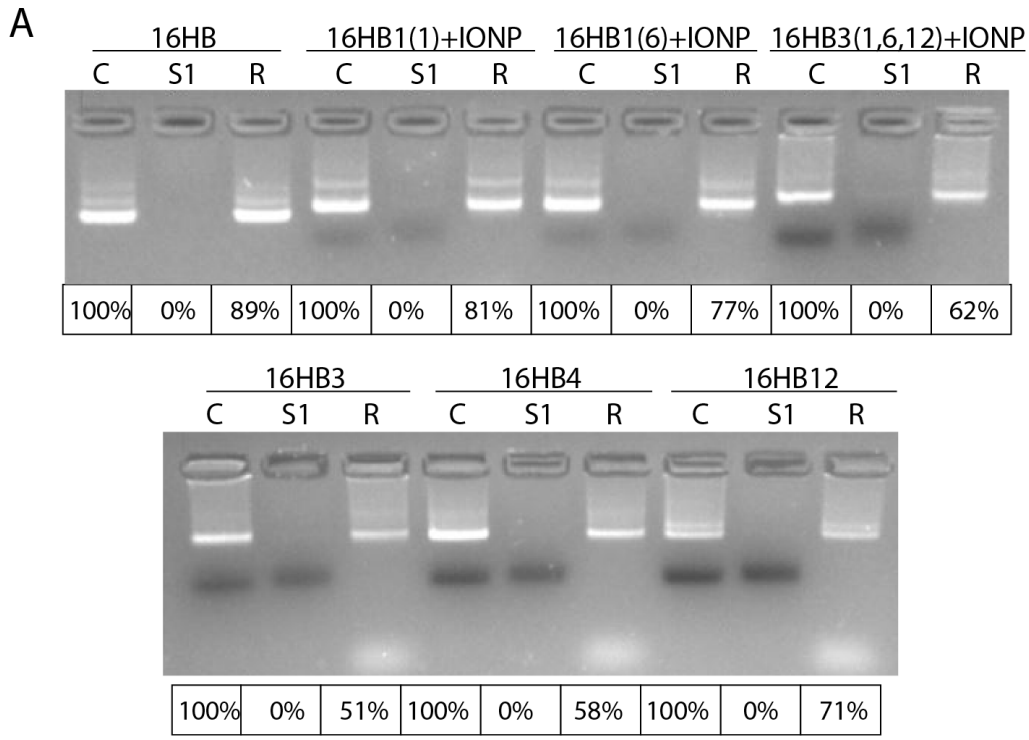

Figure 4-26. Effect of IONP Placement on 16HB Recovery - 13pA Binding. AGE of 16HB binding and recovery from polymeric beads along with band intensity analysis to estimate relative yields. C - Control, stock 16HB solution, S1 - Supernatant from first wash step, R - Supernatant following 16HB release. 16HB with different numbers and positions of bound IONPs were analyzed.

4.4.1.5 T_2 Measurements of 16HB-IONP Assemblies

After IONPs have been assembled on the 16HB and purified from excess IONP using the bead pull-down method, the next step was to monitor the effect of assembly on T_2/r_2 measurements. We used a time-domain 1D nuclear magnetic resonance machine, which can be programmed to run through a CPMG pulse sequence mimicing that used in traditional T_2-weighted MRI imaging to calculate signal intensity vs echo time, allowing T_2 to be extracted from the curve using an exponential fit. By calculating T_2 at several different concentrations (i.e. serial dilutions) of the same sample, r_2 can be calculated

through a linear fit of $1/T_2$ vs concentration.. There is some concern over the reliability of these measurements primarily due to the specifics of the NMR machine that was available for use at Georgia Tech, as the machine was very old with suboptimal temperature control. Significant effort went into to identifying optimal operating procedures to minimize measurement variability (data not shown), and comparisons to measurements made with a more appropriate instrument (Bruker MiniSpec) show that data collected in this manner is reliable enough for this work.

In order to calculate r_2 values and compare the effect of assembly across multiple different samples, the exact concentrations of each sample must be known. While this is typically not a problem for traditional IONP contrast agents, which can be prepared in large quantities and are easily manipulated, the nature of the 16HB-IONP preparation and purification made accurate concentration measurements very challenging. The buffer necessary for 16HB-IONP assembly and stability (Tris, EDTA, and Magnesium) was not compatible with the standard colorimetric assay used in our lab to measure iron concentrations. Furthermore, the concentrations of samples immediately following purification were below the detection limit of this assay. As such, post-processing involving the heat-induced degradation of 16HB, centrifugation, and resuspension/concentration in pure water was needed. This process introduced its own variability, which combined with the native variability of the ferrozine assay by itself and the small sample volumes preventing repeat measurements, made the accurate determination of concentration unreliable. We also tried to use inductively coupled plasma-optical emission spectroscopy through the use of a core facility at University of Georgia, but test measurements on our samples revealed significant variability here as well. As such,

we developed a concentration-independent method for monitoring the effect of IONP-assembly. Because these structures are not stable at high temperatures due to melting of the DNA double-helices, heating of the structures destroys the underlying assembly, freeing the particles to behave like individual, un-assembled IONPs (Figure 4-27). By measuring T_2 before and after heating of the samples, we can directly probe the effect of assembly on T_2 irrespective of concentration, as the concentration of particles stays the exact same before and after heating. Furthermore, we can calculate the change in r_2 due to assembly by measuring T_2 values before and after heating of a serial dilution of 16HB-IONP samples and plotting the values before and after heating with arbitrary concentration values – since we are only looking at difference between r_2 values rather than the actual value itself, this process gives the exact same value (percent change following heating) regardless of what concentration is used for the calculation. However, as a reference we were able to calculate the exact value of r_2 for 15nm IONP samples since the concentration of the stock mixture was known – 138 $mM^{-1}s^{-1}$ - thus r_2 values of the other assemblies can be estimated based on percent change from that value.

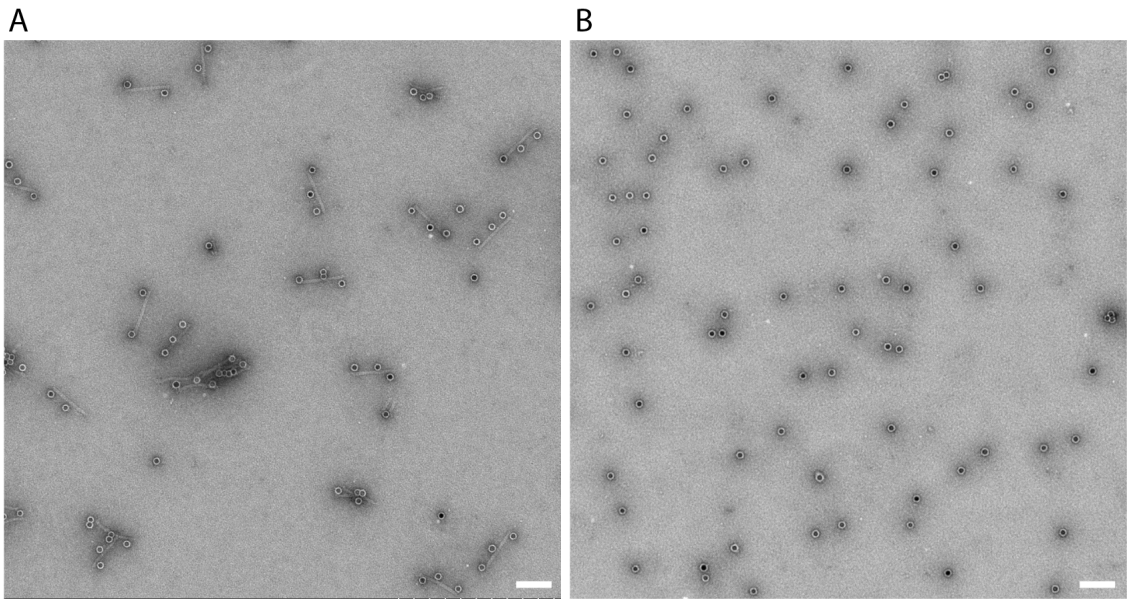

Figure 4-27. Effect of Heating on 16HB-IONPs. Representative TEM image of 16HB-IONP samples A) before and B) after heating to 85°C.

T_2 changes with Streptavidin-IONP

We first monitored the effect of 16HB-mediated assembly on T_2 using the commercial 10 nm STV-modified IONPs. Because yields of the assembly were so low, we were skeptical that any difference could be seen between small changes in IONP number. We thus compared 16HB designs containing either 3 binding sites or 12 binding sites. We found that assembly had a significant effect on T_2 relaxivity of the assemblies, where the 16HB3 design led to a ~20% increase in r_2 and the 16HB12 design led to a ~40% change in r_2 (Figure 4-28). Interestingly, we did find a small change in r_2 following heating of the free IONPs. However, this value is not statistically different than 0, and there are likely some measurement error or other small effects that could be leading to this change. Repeated measurements of the same sample did show a slight drift in T_2 values, so issues with the NMR machine are likely contributing to this effect.

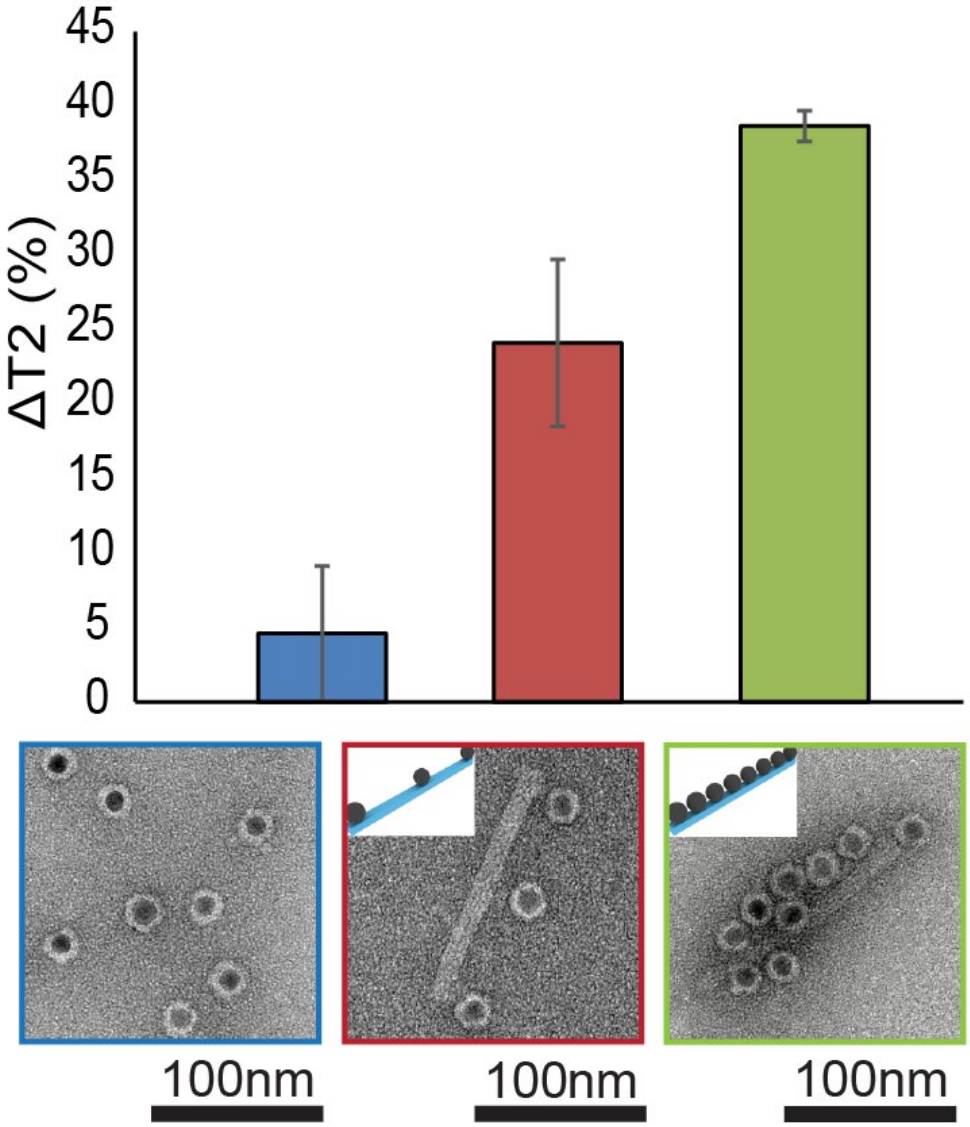

Figure 4-28. Effect of STV-IONP Assembly on T_2. Relative change in T_2 before and after heating of free IONP (blue), 16HB3+IONP (red), and 16HB12+IONP (green) along with representative TEM images. N=2, mean ± s.d.

T_2 changes with DNA-IONP

We then tested 16HB-IONP assemblies using DNA-IONP, which produced conjugates with much better yields. We also switched to use 15 nm IONPs, allowing us to use lower 16HB concentrations during measurements and thus made the sample preparation for these experiments easier. In order to investigate the effect of IONP number on T_2 relaxivity enhancement, we used 16HB designs with either 1, 2, or 3 binding sites with ~50nm spacing between particles (16HB2-1,6 and 16HB3-1,6,12). We found that these small changes in the number of IONPs led to significant alterations in r_2, with 2 bound IONPs producing a ~10% increase in r_2 and 3 bound IONPs producing a ~20% increase in r_2 (Figure 4-29). As with the previous experiment using STV-IONPs, we did find that there was a small change in 16HB with 1 bound IONPs following heating, though this change was not statistically different than 0%. In order to identify the maximum enhancement efficiency possible using the 16HB system, we also designed a structure in which the binding sites on all 4 faces were saturated. Using this system, we were able to observe a 140% increase in r_2 values for samples with an average 8 IONP/cluster (Figure 4-30). We also compared 16HB with 1 bound IONP to free IONPs and found that there was no significant difference, implying that the presence of the 16HB did not have any effect on the relaxivity of the particles (Figure 4-31). The samples used for NMR measurements were somewhat heterogeneous - we found that ~50% of all IONPs were present in the correct formation, with an average of 1.6 IONP/cluster for the 16HB2 assembly and 2.7 IONP/cluster for the 16HB3 design. Unfortunately, there was a significant number of free IONPs that were not purified, as well as aggregation induced during purification.

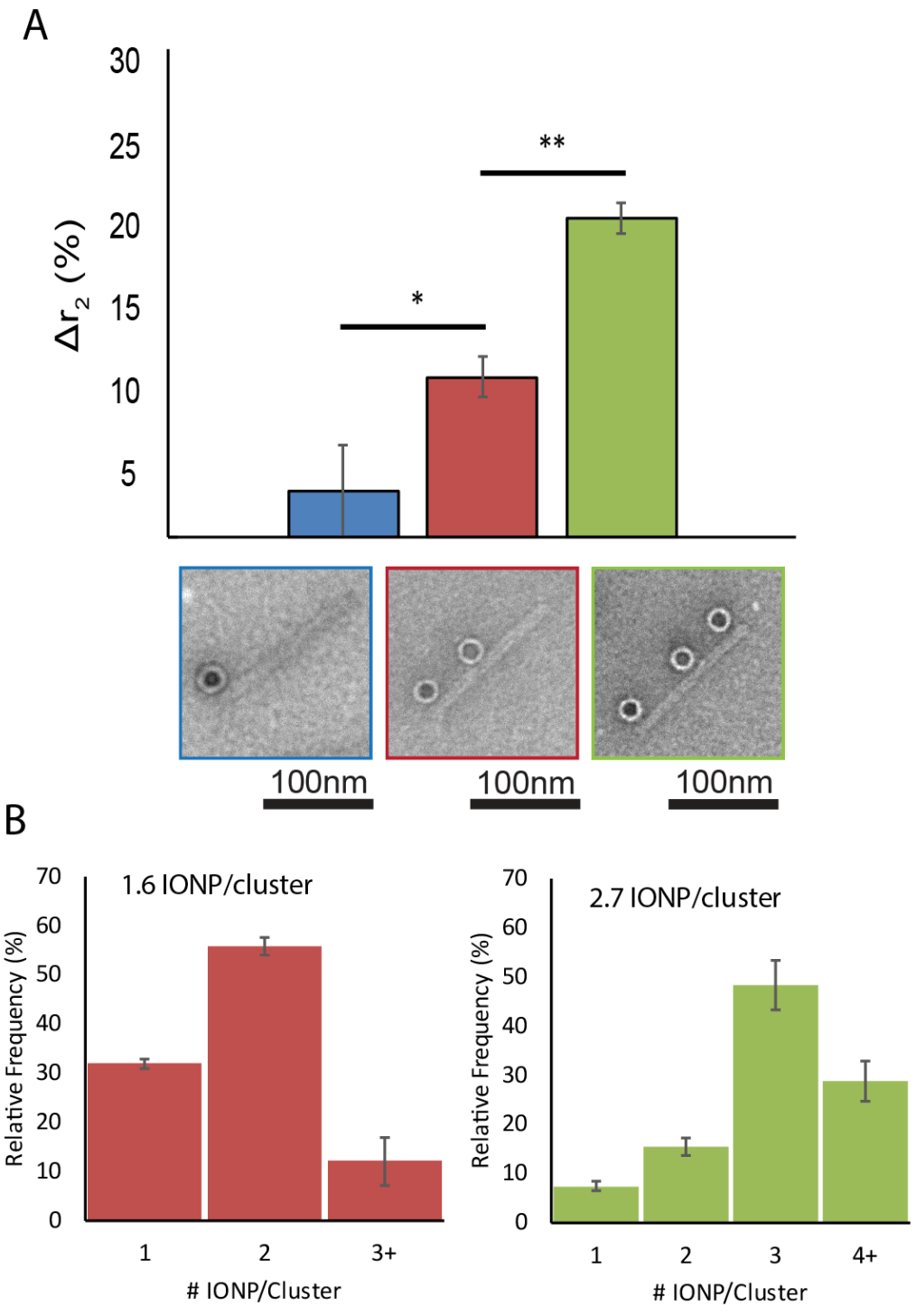

Figure 4-29. Effect of the Number of DNA-IONP Assembly on T_2 relaxivity. A) Relative change in T_2 relaxivity before and after heating of 16HB1 (blue), 16HB2 (red), and 16HB3 (green) with attached IONPs along with representative TEM images. N=3, mean ± s.d., * p<.05, ** p<.005 B-C) Distribution of IONPs based on cluster size for B) 16HB2 and C) 16HB3 along with average number of IONPs/cluster.

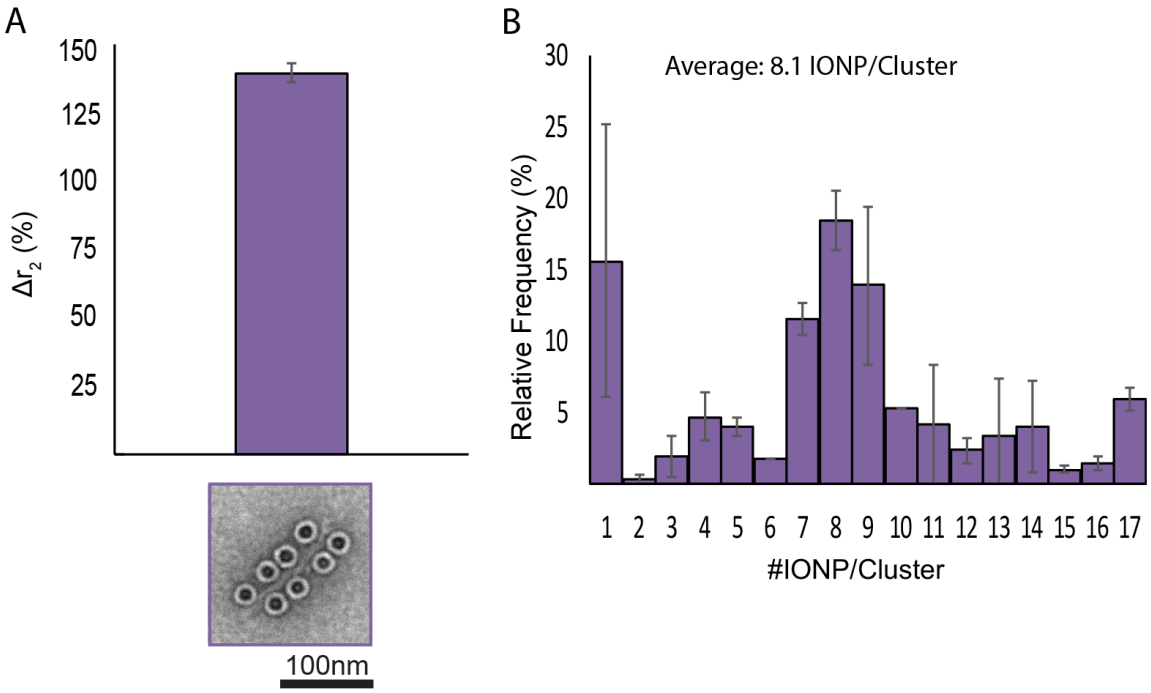

Figure 4-30. Effect of Maximizing DNA-IONP Loading on T_2 Relaxivity. A) Relative change in T_2 relaxivity before and after heating of 16HB-Full + DNA-IONP along with representative TEM images. B) Distribution of IONPs based on cluster size along with average number of IONPs/cluster. N=2, mean ± s.d.

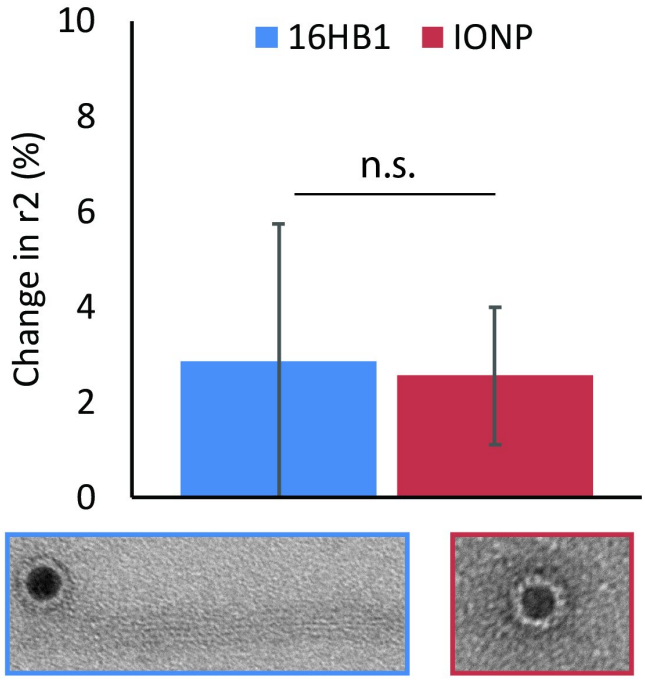

Figure 4-31. Effect of 16HB on T_2 Relaxivity of Single DNA-IONPs. A) Relative change in T_2 relaxivity before and after heating of 16HB with 1 IONP (blue) or free IONPs (red) along with representative TEM images. N=3, mean ± s.d. n.s. p> .05

Next, we investigated the effect of IONP spacing on r_2 enhancement. We designed three 16HB structures with 2 binding sites, spaced either 40nm (16HB2-1,5), 70nm (16HB2-1,8) or 100nm (16HB2-1,11) apart. Unfortunately, closer spacing than 40 nm was not feasible due to the significantly decreased yields at these distances. We found a minor effect, if any, on the modulation of r_2 in respect to spacing for these three samples. (Figure 4-32). There was no statistical difference between 40-nm and 70-nm spacing, and while there was a statistically significant difference between the 100 nm spacing and the others, this was still a relatively minor change. Differences in the yield of different populations across each sample could be shielding any effect due to spacing – for example, the 40nm

spacing sample had higher single IONP clusters and fewer aggregated IONP clusters, which could be artificially decreasing the observed r_2 enhancement relative to the 70nm spacing sample. There is a chance that changes due to IONP spacing could be observed if samples with higher purity and/or closer spacing could be produced. However, given the relatively small predicted enhancement at these spacing, it is likely that clear differences will be too difficult to observe experimentally.

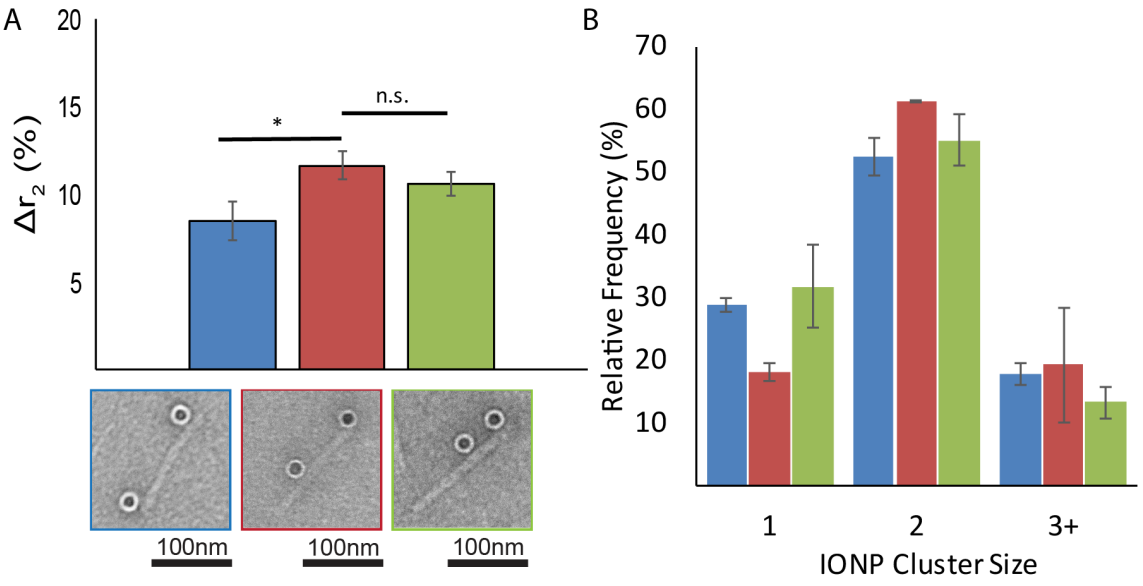

Figure 4-32. Effect of DNA-IONP Spacing on T_2 Relaxivity. A) Relative change in T_2 relaxivity before and after heating of 16HB-2 + DNA-IONP with different spacing (Blue - 115 nm, Red - 75 nm, Green - 45 nm) along with representative TEM images. B) Distribution of IONPs based on cluster size. N=2, mean ± s.d. * $p<.05$, n.s. $p> .05$

In relation to previous experimental studies, the maximum r_2 increase we have observed is comparable to that observed using other clustering methods. For example, we found ~100-120% increases in r_2 in our previous work (Chapter 3) with both 8 and 15 nm IONPs[145]. Other groups have found similar increases between 150-160% for the largest clusters[86, 87]. Perhaps most interesting, the enhancement values we observed are significantly larger than those from the studies using the most similar clustering systems, namely the bacteriophage and dsDNA systems [109, 160]. Using the bacteriophage system, the researchers surprisingly showed no significant increases in r_2 despite an apparent large number of bound IONPs. Similarly, Ryu et al only showed a ~10% increase in r_2 when attaching ~11 IONP to their dsDNA template. It is unclear exactly why these studies showed such small changes in r_2 enhancement relative to our work and others. One potential explanation could be the large r_2 values of the free IONPs used by Ryu et al, which started at 288 $mM^{-1}s^{-1}$ relative to our 130 $mM^{-1}s^{-1}$, and that the large percent increases only occur with less efficient single IONPs.

In relation to the previous theoretical studies, direct comparisons are challenging due to both the reported parameters (R_2 for theoretical work vs percent change in r_2 here) as well differences in spacing/number combinations. For example, Brown et al found a power law relationship of $R_2 = N^{0.44}$, which predicts a ~35% increase with 2 particles and a 62% increase in a system with 3 particles[105], much higher than that found in our system (10% and 20%, respectively). This difference could come from several factors – in their simulation Brown et al used particle clusters with much closer inter-particle distances, which is predicted to also lead to increases in relaxivity. Furthermore, the presence of heterogenous sub-populations in our system, including free IONPs and 16HB with only 2

bound IONPs, could leave to a diminished observed signal in our system. Our work also shows a much larger effect for 8 particles than would be predicted based on changes in 2 and 3 particles, which also does not match the predicted power law relationship: again, this comparison is complicated by the simultaneous change in IONP distance in our experiments. However, the 8 particle system with closer spacing did match the predicted enhancement. Our results also matched a 3 particle simulated system with 40 nm spacing. Similarly, the predicted change in a 2-particle system from this work is larger than what we observe at a given spacing. Work by Matsumoto et al show changes in R_2 to be 23%, 15%, and 11% at the 40nm, 70nm, and 100nm spacing used in our study[84]. However, these simulations were conducted using systems of 3 particles, which should produce larger relative changes compared to a system of 2 particles used in our experiments. Future work with larger DNA structures to facilitate construction of clusters with both higher numbers of evenly spaced particles and changes in spacing between 3 particle systems would be helpful in more closely matching these simulations.

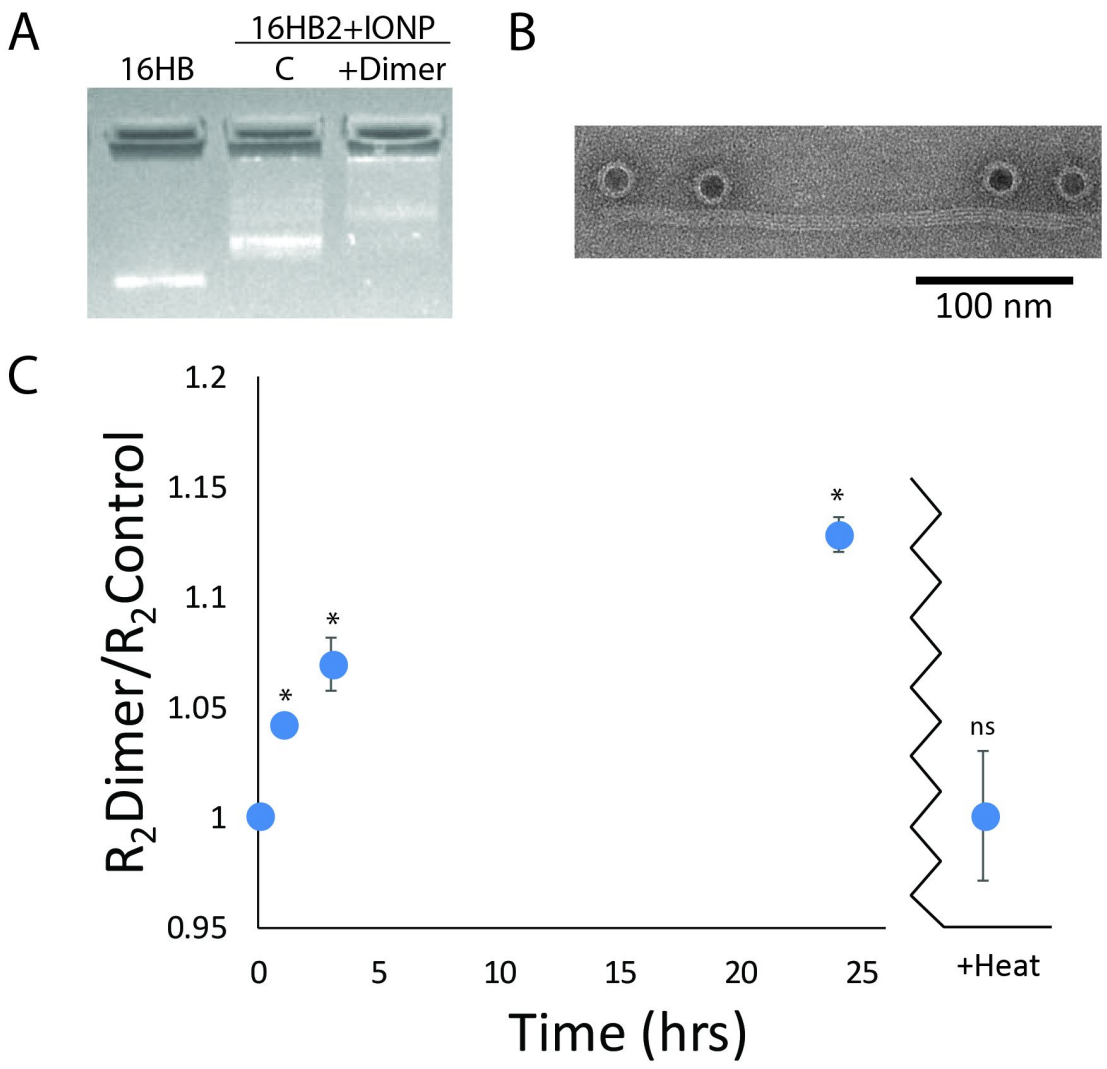

Figure 4-33. Dimerization and Dynamic T_2 Changes with 16HB-IONP. A) AGE image of 16HB2(1,6) with attached IONP before (C) and after (+Dimer) the addition of dimerization strands and incubation at 35°C for 3 hours. B) Representative TEM image of 16HB2(1,6)+IONP dimer. C) R_2 of 16HB2(1,6) samples after incubation at 35°C following addition of dimerization strands at different time points. R_2 values of samples were normalized to sample without the addition of dimerization strands. R_2 ratio was also calculated after heating at 85°C.

Dynamic Modulation of T_2 Enhancement

Finally, we were interested in using dynamic changes in the assembly of our 16HB to drive dynamic changes in T_2 relaxivity, much like the magnetic resonance switches developed by others. We used the 16HB dimer system developed previously – addition of connecting strands to a sample of 16HB-IONP should lead to dimerization of the 16HB, an increased in the number of IONPs per cluster, and a subsequent change in R_2 ($1/T_2$). We found that addition of connecting strands to solutions of 16HB2(1,6) with attached IONPs did lead to the formation of dimerized structures, as observed by a shift in AGE mobility, and TEM imaging validated the formation of 300 nm long 16HB rods containing 4 bound IONPs (Figure 4-33). For NMR measurements, we prepared two identical solutions of 16HB2+IONP and measured T_2 for each sample. We then added dimerization strands to one of these solutions and continued to measure R_2 values overtime for these solutions. We normalized R_2 values of 16HB-IONP + dimer to control samples, and found that R_2 increased over time, with a maximum enhancement of ~13% after 24 hours. When normalized to initial T_2 measurements, the R_2 value of the dimerized sample increased overtime while the control sample actually decreased – this phenomenon is likely the same as observed for r_2 changes in free IONPs after heating and due to issues with the NMR machine. After heating of the samples, the R_2 values returned to identical values which indicates that the IONP concentrations were the same between samples and that all R_2 increases were due to dimerization-induced increases in IONPs/cluster. Analysis of the sample after 24 hours by AGE and TEM revealed significant aggregation of the dimerized samples, which does raise some concern that this could be affecting R_2 changes (data not shown).

4.5 Conclusions and Future Directions

In this work, we've demonstrated a novel method for controlling the spatial organization of IONPs. This technique offers the unprecedented ability to modulate the spacing and number of IONPs with a high degree of precision and control. With this system, we demonstrated how single particle additions to clusters can lead to r_2 enhancement, with maximal enhancement on par with other clustering-based techniques. This system can now serve as a modular platform that can be further adapted and improved to allow for a number of other parameters to be investigated. Additionally, we have also demonstrated one of the first integrations of magnetic nanoparticles with DNA origami, and the first to demonstrate functionality using this system. These constructs can offer a new method for tracking the fate of DNA origami nanostructures *in vivo* using MRI, facilitating further studies into the use of DNA nanoparticles as drug-delivery vehicles.

Considering most of the experiments done in this thesis served primarily as a proof-of-concept demonstration of a novel technique, more work can be done to further understand the details of the DNA-origami mediated assembly of IONPs. For example, it would be interesting to see how the trends observed here would change if IONPs with different sizes are used. There are also a number of new parameters that can be evaluated by using different DNA origami nanostructures - for example, the use of a 400-nm long 6HB rod would facilitate the incorporation of larger numbers of IONPs with increased inter-particle spacing. We could then evaluate if continual increases in IONP number will follow a power law relationship with T_2 relaxivity as predicted by theoretical models, or identify a maximum inter-particle spacing at which the increase in r_2 is lost. More complex DNA origami nanostructures can also be used to vary the geometric arrangement – for

example, hexagonal tiles previously developed by our lab could be used to test circular and 2D planar assemblies, while polyhedral structures could be used to test spherical/shell orientations. More in-depth studies into the dynamic assembly to drive T_2 changes are also needed to optimize this procedure. Further improvements in the technical aspects of this work could be done. A better understanding of the synthesis of azide-PMAO is needed, as we were unable to replicate the synthesis and thus were limited in the quantity of particles we could synthesize – future work will require the ability to create this polymer in-house. Improvements in the yield of IONP binding could also help to provide a clearer understanding of the r_2 enhancement effects by eliminating side products that could dilute the signal, while alterations in the IONP themselves to allow for closer packing would be helpful for validating large r_2 increases predicted to occur at small inter-particle distances.

Finally, there is promise for these IONP-DNA constructs to be used as sensing elements based on the stimuli-directed assembly/disassembly of the 16HB. Dynamic changes linked to a specific stimuli such as pH or clinically-relevant mRNA would enable these structures to be used as *in vitro* sensing probes or *in vivo* molecular imaging contrast agents. The use of ultrasmall IONPs would potentially enable switching between T1 and T2-dominate contrast generation, which would have improved clinical relevance. As such, it would be especially interesting to try to evaluate the *in vivo* behavior of these nanostructures, though the technical requirements of sample preparation will likely be a significant hurdle.

CHAPTER 5. SYNTHESIS OF ROLLING NANOSCALE DNA MOTORS

5.1 Abstract

There is considerable interest in the development of synthetic molecular motors that can recapitulate the directed motion of protein machines within cells. DNA walkers have shown promise as molecular motors with highly tunable properties and simplified design. However, these walkers exhibit slow velocities and limited processivity relative to proteins, limiting further expansion of their applications. Here we demonstrate a nanoscale motor made entirely of DNA using the DNA origami technique that exhibits a unique rolling motion, enabling speeds of up to 200 nm/minute and total displacements on the micron scale. By leveraging the unique capabilities of DNA origami, we independently assess the impact of polyvalency, motor domain density, and rigidity on the behavior of these motors. We anticipate that the DNA origami machines presented here will have uses in a variety of applications, including biosensing, molecular robotics, and DNA computing.

5.2 Attribution of Effort

I would first like to note that the work presented in this chapter was the result of a collaboration with Dr. Khalid Salaita's lab at Emory University. The work done was shared equally between myself and Alisina Bazrafshan. Alisina was the one who did everything related to the microscopy work – he conducted the experiments, analyzed the data, and created the figures related to this part of the study. As such, he deserves major credit for a significant portion of this portion of the thesis. The results presented here

will likely be published soon, with many figures taken directly from the manuscript – given that this thesis will be submitted prior to that, I unfortunately am not able to cite the specific publication.

5.3 Introduction

Directed motion at the molecular level plays a critical role in a wide variety of biological functions, including intracellular transport and mitosis[110-112]. There has been considerable interest in developing synthetic motors inspired by these biological machines for use as model systems for studying natural processes as well as for technical applications, such as biosensing, molecular computing, etc. [113, 114]. Of the various types of synthetic motors that have been created, DNA walkers are some of the most studied – the precise programmability of DNA makes it an excellent material for constructing nanoscale motors and machines[2]. DNA-walkers have been designed using numerous different strategies for inducing motion along a track, and have been used to perform a variety of tasks [121, 122, 127, 132, 140, 144, 172, 173].

While DNA-based machines that walk along a track have shown the greatest promise in recapitulating the properties of biological motor proteins, these motors are limited to slow velocities, limited processivity, and limited programmability. Increasing the number of connection points between walker and track can limit spontaneous dissociation and improve motor endurance, but this increased polyvalency leads to a significant decrease in motor velocity[129]. One exception to this trade-off is the rolling behavior of highly polyvalent DNA-coated silica microparticles[130]. The process of rolling, which reduces DNA motor footprint by limiting unproductive sampling

interactions, represents a fundamentally distinct type of movement that overcomes the documented trade-offs inherent to other multivalent molecular motors.

We sought to engineer highly-tunable nanoscale motors exhibiting this rolling motion using DNA origami. DNA origami has emerged as one of the premier methods to precisely control nanoscale features and has been used to construct a wide variety of intricate one-, two-, and three-dimensional nanostructures and molecular machines[1, 8, 174]. To the best of our knowledge, dynamic DNA origami structures have only been used to construct machines which undergo local relative motion to apply work on their surroundings, or as a landscape to facilitate the movement of other molecular walkers [175]. We hypothesized that DNA origami could be used to create nanoscale motors with increased control over every aspect of the design process, facilitating the construction of faster, unidirectional nanoscale DNA motors with tunable motion. Furthermore, we can capitalize on the global addressability of DNA origami to experimentally determine the roles of polyvalency and distribution in DNA motor movement through precise engineering of the location of the DNA 'feet'[176].

Here we demonstrate for the first time a DNA origami nanostructure that acts as a DNA motor, processively converting chemical energy to mechanical motion. We designed a polyvalent 16 helix bundle (16HB) DNA origami nanostructure that moves thousands of nanometers via a rolling mechanism and can be programmed to carry cargo strands at multiple sites. These motors roll on a straight line for thousands of body lengths with velocities up to 200 nanometers per minute. Additionally, we are able to decouple the relationship between DNA leg density/polyvalency and demonstrate that tuning the density of the DNA legs maximizes the velocity and distance travelled of nanoscale rolling motors.

Finally, we show that the rigidity of the motor is an important driver of the super-diffusive motion of these DNA origami motors.

5.4 Materials and Methods

All chemicals were purchased from Sigma-Aldrich unless otherwise stated. Stock solutions were made using Nanopure water (Barnstead Nanopure system, resistivity = 18.2 MΩ), herein referred to as DI water. All oligonucleotides were purchased from Integrated DNA Technologies. RNase H was obtained from Takara Clontech. Ibidi Sticky-Slide VI 0.4 channels and Teraspek™ Microspheres were purchased from Thermofisher. NHS-PEG_4-azide was purchased from Click Chemistry Tools.

5.4.1.1 Optical Microscopy

The microscope was equipped with an Intensilight epifluorescence source (Nikon), a CFI Apo 100 × NA 1.49 objective (Nikon), and a TIRF launcher with three laser lines: 488 nm (10 mW), 561 nm (50 mW), and 638 nm (20 mW). The microscope also included a Nikon Perfect Focus System, which allows the capture of multipoint and time-lapse images without loss of focus. All of the reported experiments were performed using the Quad Cube (97327), TRITC (96321) filter cube set supplied by Chroma.

5.4.1.2 Super-resolution Imaging of the Fluorescence-Depletion Tracks

SIM images were acquired on a Nikon N-SIM system equipped with a CFI Apo ×100 1.49 NA objective and an Andor iXon EMCCD (60 nm per pixel). For each N-SIM image, nine images of a 3′-Cy3-RNA sample were acquired in different phases using a 561

nm laser as an excitation source and were reconstructed using the Nikon Element software package.

5.4.1.3 Fabrication of RNA monolayers

A No. 1.5 glass slide (25 × 75 mm) was cleaned by sonication in DI water for 15 minutes in 200 proof ethanol for 15 minutes and was subsequently dried under a stream of N_2. The silicon glass was etched by piranha solution (v/v = 3:7 hydrogen peroxide/sulfuric acid) for 30 min to remove residual organic materials and activate hydroxyl groups on the glass. The cleaned substrates were rinsed with DI water in a 200 mL beaker for at least 6 times and further washed with ethanol thrice. Slides were then transferred to a 200 mL beaker containing 2% APTES in ethanol for 1 h, washed with ethanol thrice, and thermally cured in an oven (~110ºC) for 10 min. The slides were then mounted to 6-channel microfluidic cells. To each channel, ~50 µL of 10 mg/mL of NHS-PEG_4-azide in 0.1 M $NaHCO_3$ (pH = 9) was added and incubated for 2h. The channels were washed with 1 mL DI water thrice and the remaining water in the channels was removed by pipetting. DNA-functionalized slides were prepared using a copper-catalyzed azido-alkyne cycloaddition reaction - after thoroughly rinsing the surface with deionized water, a solution of 10 µM alkyne-modified DNA (anchor strand), 500 µM THTPA, 200 µM $CuSO_4$ and 5 mM sodium ascorbate in 1 M potassium phosphate buffer was added to the surface. The surface was treated with water and PBS to remove excess amounts of DNA that were not conjugated to the surface. The chamber was then sealed by Parafilm to prevent evaporation. After incubation, excess DNA was removed from the channel using a ~5 ml DI water rinse. Lastly, the RNA substrate was immobilized to the surface through hybridization of 100 µl of a complementary RNA/DNA chimera (100 nM) in 1 × PBS for 12 hours. The wells were

sealed with Parafilm for each step to prevent evaporation and the resulting RNA monolayer remained stable for weeks, as determined by fluorescence imaging.

5.4.1.4 Determining RNA Surface Density

RNA surface density was determined by releasing the Cy3-tagged RNA from the surface by adding 100 µl of RNase A (100 µg ml^{-1} in 1 × PBS) and then quantifying the Cy3 fluorescence intensity in solution using a calibration curve obtained with the fluorescence microscope.

5.4.1.5 Synthesis, Purification, and Characterization of 16HB Origami Structures

Single-stranded scaffold p7560 was prepared from M13 phage using a previously reported method. A 16HB rod was designed in caDNAno, based on a 4x4 square lattice cross-section. To synthesize 16HB, a 10-fold excess of staple strands were mixed with p7560 scaffold strand (10nM) in folding buffer (5mM Tris, 1mM EDTA, 10mM $MgCl_2$) with a total volume of 50µL. The mixture was denatured at 85°C for 10 minutes, followed by a slow anneal from 60°C to 25°C over 18 hours (-1°C/30 minutes). 16HB were purified from excess staples using agarose gel electrophoresis (0.67%) in 0.5×TBE+Mg buffer (45 mM Tris, 45 mM Boric acid, 1 mM EDTA, 10 mM $MgCl_2$). AlexaFluor647 imaging strands were subsequently added at 32x excess and the mixture was incubated at room temperature for at least 3 hours before experiments. 16HB structures were characterized by agarose gel electrophoresis (1.5%) and negative-stain TEM imaging (1% Uranyl Formate).

5.4.1.6 Particle Translocation Powered by RNase H

Initially, RNA-substrate surfaces were washed with 5 ml of PBS to remove excess unbound RNA. Next, DNA Origami structures were hybridized to the RNA substrate. Briefly, 1 µl of purified DNA Origami particles were diluted with 1X RNase H buffer to 10pM concentration. 50 uL of that solution is was added to the RNA substrate. Hybridization between the particles and the complementary RNA monolayer occurred over an incubation period of 2 minutes. After hybridization, excess 16HBs and unbound imaging strands were washed using 1 mL of RNase H buffer. Then a solution of tetraspek beads was added. The unbound beads were washed with 1 mL of RNase H buffer. After, particle translocation was initiated by buffer exchange with 100 µl of RNase H reaction buffer (25 mM Tris pH 8.0, 8 mM NaCl, 37.5 mM KCl, 1.5 mM $MgCl_2$, 10% formamide and 0.75% (g ml^{-1}) Triton X, 1mM DTT) and different concentrations of RNase H from an enzyme stock of 7.2 µM enzyme.

5.4.1.7 Image Processing

Image processing was performed in MATLAB 2016a (MathWorks) and in Picasso [177], a software that is freely available via the Jungmann lab website. The bioformats toolbox enabled direct transfer of Nikon Elements image files (.nd2) into the MATLAB environment. The search area was set to 3 pixels (= 402 nm). The net movement of all fiducial markers in the field of view was subtracted from walker trajectories using a custom MATLAB script to account for *x–y* stage drift. A given trajectory was used in subsequent analysis only if the following conditions were met: was in range of cut off for detection as described by fluorescent signature of 16 helix bundles, lasted 30 minutes

(60 frames) without photobleaching, exhibited no sudden fluorescence intensity changes as determined by manual inspection of the output from PICASSO fitting, showed no evidence of multiple particles present in one trajectory, and fit to log-log equation with an R^2 greater than 90%. Calculation of MSD was performed as follows: the position of particle is defined as a moving average of 5 subsequent position measurements to reduce lateral noise, and the distance of each lag time was then calculated and average and fit to a log-log function only taking into account 80% of the data in each trajectory.

5.5 Results and Discussion

5.5.1.1 Design and Synthesis of DNA Origami Motors

The DNA origami motor was designed on a square lattice, consisting of 16 double-stranded helix bundles (16HB) linked together to produce a rectangular prism with dimensions ca. 10 nm x 10 nm x 130 nm, and was assembled by annealing a mixture of short synthetic 'staple strands' with a long 'scaffold' strand (Figure 5-1). More details about the design and synthesis of this structure can be found in Section 3.4. We incorporated 16 cargo-carrying strands on the ends of the 16HB, which we used here to bind AF647 fluorescent dyes to facilitate single-particle tracking. Staple strands with break points on the surface of the rectangular prism were extended with ssDNA legs containing ‘motor domains’ capable of hybridizing to RNA strands attached to a glass surface. There are 36 staples on each face, providing a maximum of 144 motor domains which can bind to RNA footholds and facilitate adherence to the surface and subsequent locomotion. We can selectively modify which staples contain the motor domains, providing unprecedented control over anisotropic binding behavior of these motors. For example, we can place

motor strands only on specific faces of the 16HB, allowing for control over the distance between footholds around the circumference of the motor (geometric mutants). This facilitates testing the hypothesis that rolling is the primary mechanism of locomotion, as an increased distance between bound footholds on one face and free footholds on other faces should inhibit new strand binding and subsequent rolling. We can also selectively modify staples on the DNA origami motors in order to understand how the density and polyvalency of motor domains impacts rolling behavior. For example, we can eliminate select motor domains along the length of the 16HB to alter the local density – by moving from a total of 36 strands down to 24 and 12, we can tune the density from 6 to 4 to 2 strands/200 nm^2.We can also alter the number of motor domains while maintaining a constant density by decreasing the number of staples along the length of the 16HB which contain motor domains, maintaining a constant motor domain density (6 strands/200 nm^2) but varying polyvalency from 36 strands/face down to 18 and 9 strands. We also were able to create variations within these groups – for example, separating the 18-strand design into 2 9-strand regions. We developed a nomenclature for identifying these variant structures in which the number of sides containing extensions is listed first (i.e. $16HB_1$ for 1 side, $16HB_4$ for 4 sides), followed by the number of strands on each face (i.e. $16HB_{4-36}$ for full coverage or $16HB_{4-18}$ for structures with half the number of binding domains).

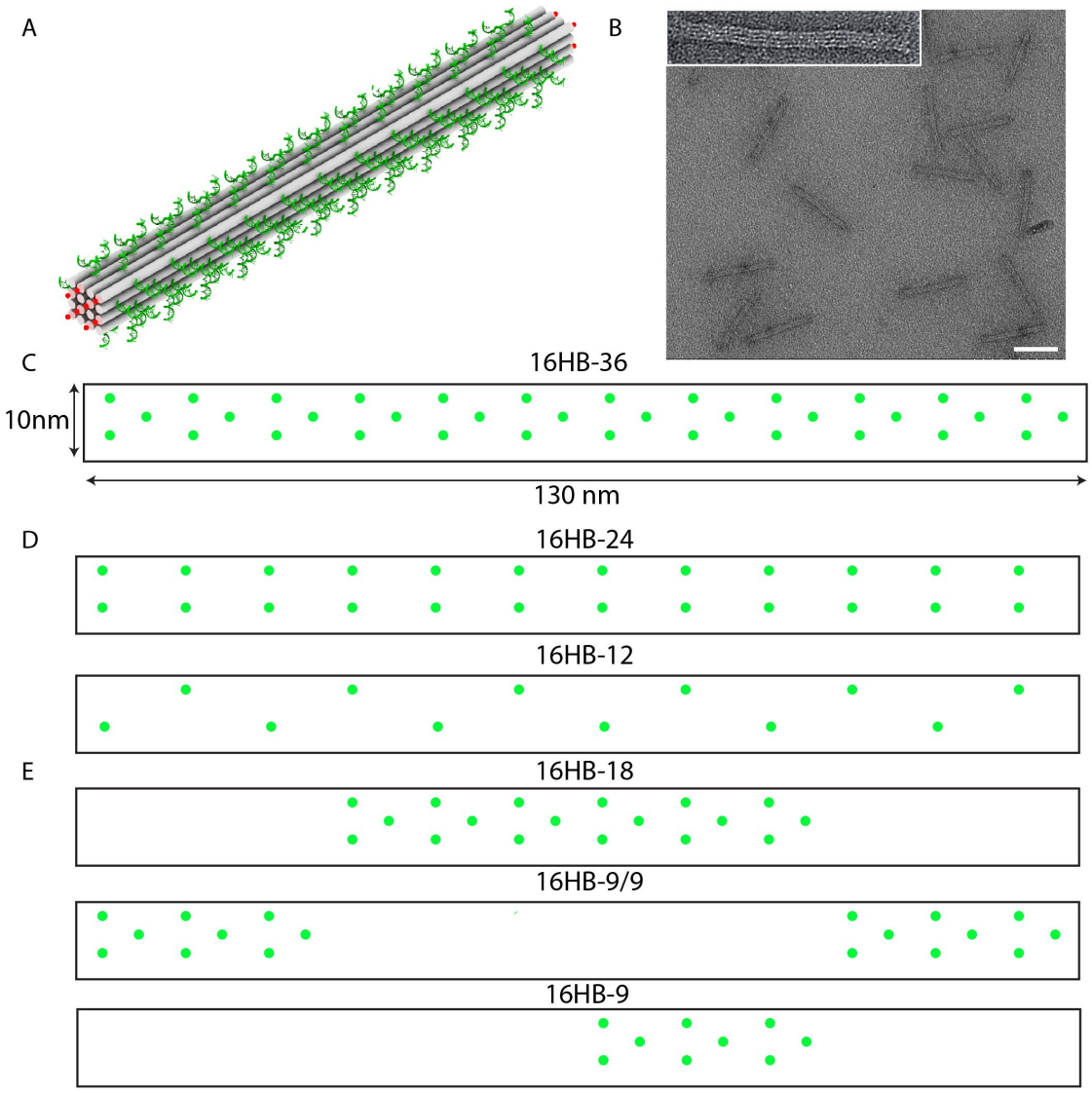

Figure 5-1. Design of 16HB DNA Origami Motor. A) 3D model of 16HB motor showing DNA origami body (grey), RNA-binding motor domains (green) and fluorescent-dye cargo strands (red). B) Representative TEM image of 16HB DNA origami motors with high magnification inset. Scale bar - 100 nm. C) Top down view of 16HB face showing possible location of all 36 motor domains. D) Variations in motor domain density with either 24 or 12 strands per face. E) Variations in motor domain polyvalency with constant density, with 18 strands in two different orientations or 9 strands.

These variant 16HB motor were prepared by swapping out staple strands containing the motor domain extensions with those lacking any extensions (a full list of all staples and their categorization used in this study can be found in the appendix). Following annealing, we analyzed each variation using both TEM and agarose gel electrophoresis. We found that there were no observable differences in the core structure of the 16HB regardless of the nature of the motor domain extensions, as seen on TEM images (data not shown). However, we did find differences in electrophoretic mobility that were dependent upon the number of motor domains that were present. For geometric mutants, increasing the number of sides which contained the RNA-binding extensions led to a concomitant decrease in mobility (Figure 5-2). Similarly, a decrease in mobility accompanied an increase in the number of extensions for the polyvalency mutants as well as for density mutants. This is consistent with the idea that ssDNA extensions from the surface of the particle increase both the overall size of the 16HB as well as the drag experienced during electrophoresis, thus leading to reduced mobility.

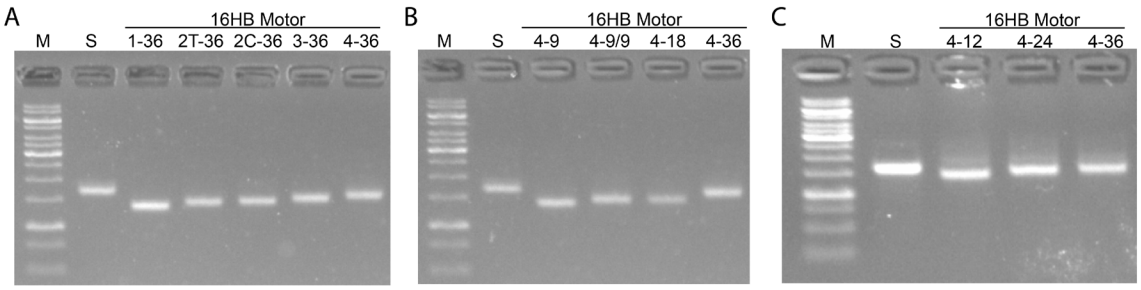

Figure 5-2. Assembly of Variant 16HB DNA Origami Motors. AGE of 16HB DNA origami motors with different motor domain distributions. M - 1kB DNA marker, S - p7560 scaffold. A) Geometric mutants with 36 motor domains on different numbers of sides B) Polyvalency mutants with all 4 sides modified with different strand patterns. C) Density mutants with all 4 sides modified with different numbers of strands.

We were also interested in designing structures to help us understand how the rigidity of the DNA motors and subsequent cooperativity between individual motor domains would affect motor behavior. In order to test this, we purposefully designed flexible 16HB structures in which a set number of staple strands were removed from the center of the design – this leads to the formation of two separate 16HB units connected together by 16 short ssDNA scaffold domains (Figure 5-3). We altered the number of staples removed to create two designs with either an 8-nt or a 32-nt ssDNA gap region and used AGE and TEM to characterize these structures. We found that the mobility of the flexible 16HB was decreased relative to control 16HB motors, and that the structures exhibited significant bending as imaged via TEM. The decreased mobility observed for the flexible structures is likely due the increased resistance experienced while moving through the agarose gel due to the loss of the streamlined profile exhibited by the standard 16HB rod. We analyzed the relative distribution of angles observed from TEM for the two different designs in order to try to quantify their flexibility – we found that the 32bp gap design did have significantly higher flexibility than the 8bp gap design as demonstrated by the decrease in the average angle observed between the two whole 16HB arms.

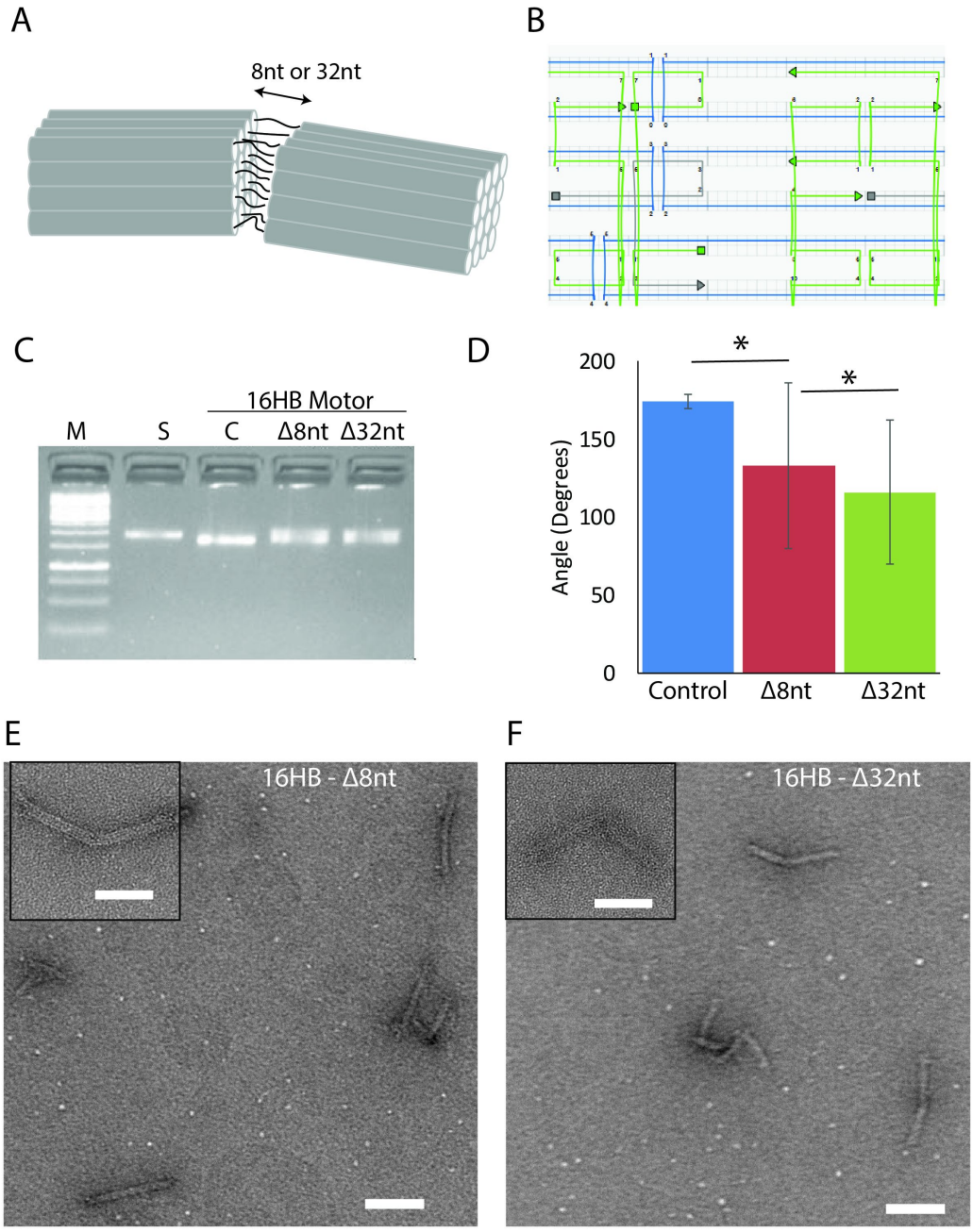

Figure 5-3 Assembly of Flexible 16HB Motors. A) Schematic showing two 16HB halves split by 16 ssDNA scaffold segments of either 8nt or 32nt lengths. B) Section of caDNAno file showing 8-nt gap design. C) AGE of 16HB motors with gaps. M - 1kB DNA marker, S - p7560 scaffold, C - Full 16HB motor. D) Average angle between each arm of the 16HB motor for the control full motor (blue), motor with 8-nt gap (red) and motor with 32-nt gap (green). N>100, mean ± s.d., * $p < .05$. E,F) Representative TEM images with high magnification inset of E) 8-nt gap motor and F) 32-nt gap motor. Scale bar - 100 nm, 50 nm inset.

5.5.1.2 Characterization of DNA Origami Motor Motion

The track for 16HB locomotion consists of a glass surface coated with an RNA-DNA chimera. The RNA sequence is single-stranded, allowing it to bind to complementary DNA sequences via Watson-crick base pairing. The RNA strand is covalently modified with a Cy3 fluorescent dye, facilitating the visualization of RNA surface coverage during the experiments. Following motor strand hybridization to the RNA track, the activity of RNase H selectively cleaves the RNA portion of the RNA/DNA duplex, altering the energy state of the motor (Figure 5-4). This change encourages binding of new motor domains to the remaining RNA track strands on the surface through a burned-bridge Brownian ratchet mechanism - the motor can then roll as a means of bringing new DNA motor domains into contact with the RNA surface.

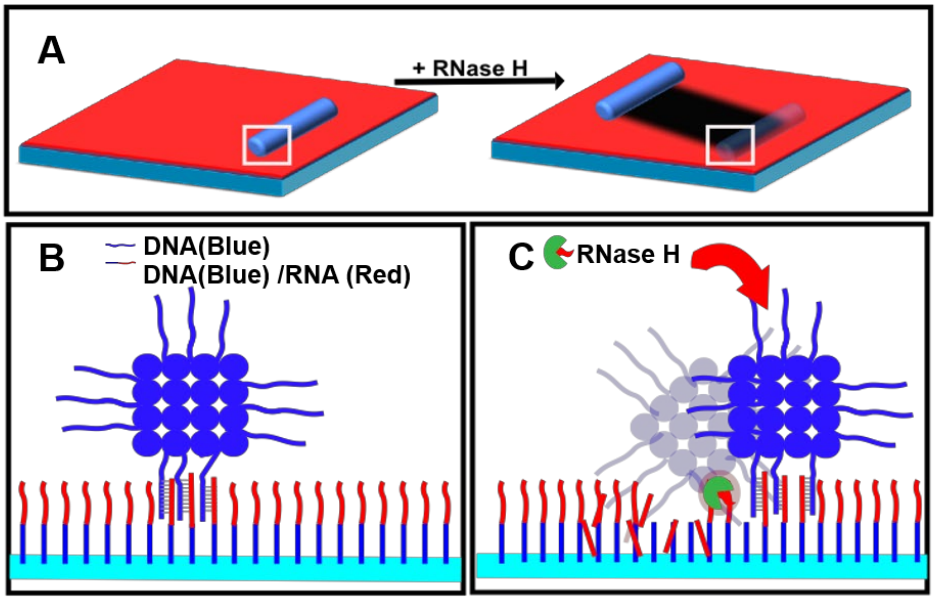

Figure 5-4. Schematic of 16HB Locomotion. RNase H cleavage of RNA in RNA/DNA duplexes induces motion of the 16HB through a burned-bridge Brownian ratchet mechanism. Degradation of Cy3-tagged RNA leads to the appearance of a depletion track where RNase H is active.

Incubation of the DNA origami motors onto the RNA surface leads to the appearance of bright spots in the AF647 channel corresponding to the 16HB, showing that the motors bind to the surface (Figure 5-5). Control experiments using DNA origami structures without motor binding domains or surfaces lacking RNA strands do not show the appearance of the spots, pointing to RNA/DNA duplex formation driving 16HB surface binding (data not shown). Upon addition of RNase H into the solution, the spots corresponding to DNA origami motors begin to move and a concomitant decrease in Cy3-lebeled RNA surface coverage is observed, consistent with RNase cleavage of the RNA substrate. Single particle tracking of the 16HB motor was accomplished by fitting a Gaussian curve to the point-spread function of a single origami and tracking the centroid of the Gaussian over time. The individual data points were smoothed to remove lateral noise and the path of the 16HB could be fit to this data, with the color along the path indicating time of localization. Using this same procedure for multiple particles within the field of view enabled the visualization and analysis of a large population of individual DNA origami motors.

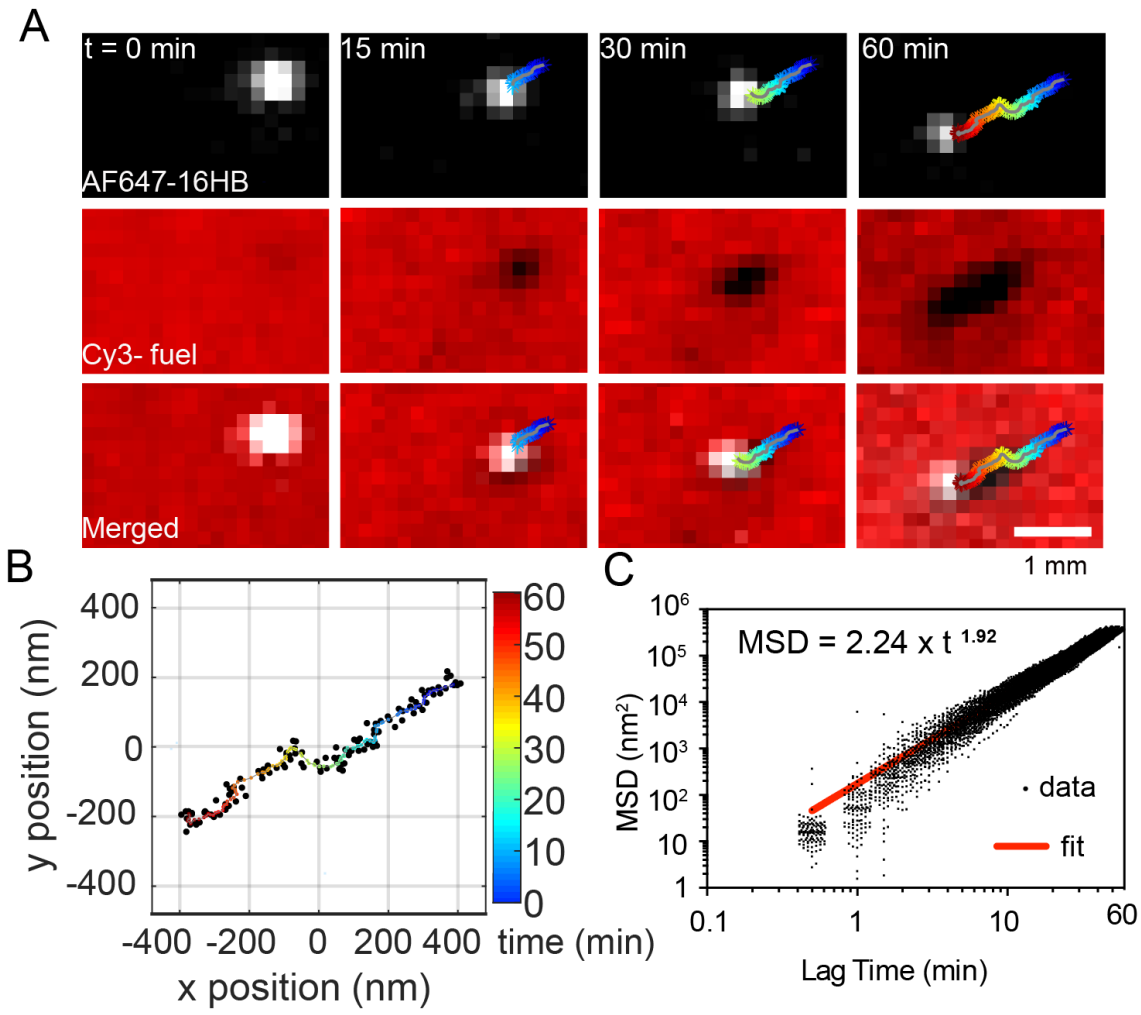

Figure 5-5. Single-Particle Tracking of 16HB Motor Movement. A) Single-particle fluorescent images of 16HB motor at different time points, with image of 16HB (top), RNA fuel (middle) and merged image (bottom). Path of 16HB movement was over-laid on top of image. B) Localizations of a 16HB from A) over time and fit of path taken color-coded based on time of acquisition. C) MSD vs time of 16HB motor from A) along with exponential fit.

One technique for analyzing molecular motion is to plot the mean squared displacement (MSD) against time. MSD is known to be proportional to t^{α}, where α is a scaling factor which can be used to identify the type of motion[178]. An α value of 1 is consistent with standard Brownian motion, while an α value less than 1 implies a sub-diffusive regime where motion is hindered and an α value of greater than 1 implies a super-diffusive regime, such as self-avoiding (α ~1.5) or ballistic (α ~ 2) motion. Because the motion of our 16HB motors should be biased away from the consumed RNA substrate and towards new regions that had not been previously sampled, we hypothesized that this motion would be in the super-diffusive regime. We plotted MSD vs time for a single 16HB and fit the data to an exponential function to calculate the α coefficient. Most of particles demonstrate an alpha coefficient greater than 1.7 which is indicative of super-diffusive motion. Furthermore, we calculated a directionality coefficient for the motion of origami structures over time, defined as the ratio of net displacement over total distance travelled. For Brownian motors this coefficient over 120 steps is 0.08 but was 0.2 for our 16HB DNA origami motors (data not shown). This was suggestive that these origami structures are rolling and not walking or sliding, as rolling should theoretically produce more linear motion.

The AF647-generated tracks match the wide-field Cy3 depletion tracks, which confirm that particle motion was associated with continual RNA hydrolysis. Structured illumination microscopy (SIM) was used to estimate the width of the depletion tracks, with an average full width half max (FWHM) of 133 nm, which closely matches the dimensions of the 16HB motor (data not shown),

We then sought to find conditions which would optimize motor processivity. We found that imaging solution conditions play a significant role in determining overall motor activity. For instance, the introduction of formamide, a denaturant which enhances RNase H activity and destabilizes dsDNA, led to significant enhancement in motor speed, processivity, and overall displacement (vide infra). We also sought to identify how enzyme concentration would affect 16HB motor activity (Figure 5-6). In the absence of any enzyme we did not see any significant motion from the motors, confirming that RNase activity is needed to destabilize existing DNA/RNA interactions and induce movement. As the enzyme concentration increased motility of the 16HB motors increased, with significant displacement occurring at 28.8nM RNase H and further processivity observed at 43.2nM. However, enzyme concentration did not have an impact on the mechanism of motion, as the alpha coefficient was the same in all conditions. The increase in 16HB MSD with increasing enzymatic concentrations confirms that RNase H activity is inducing motor translocation, as higher enzyme concentrations leads to faster RNA substrate turnover and faster k_{off} rates for the 16HB motor to leave one foothold and roll to another.

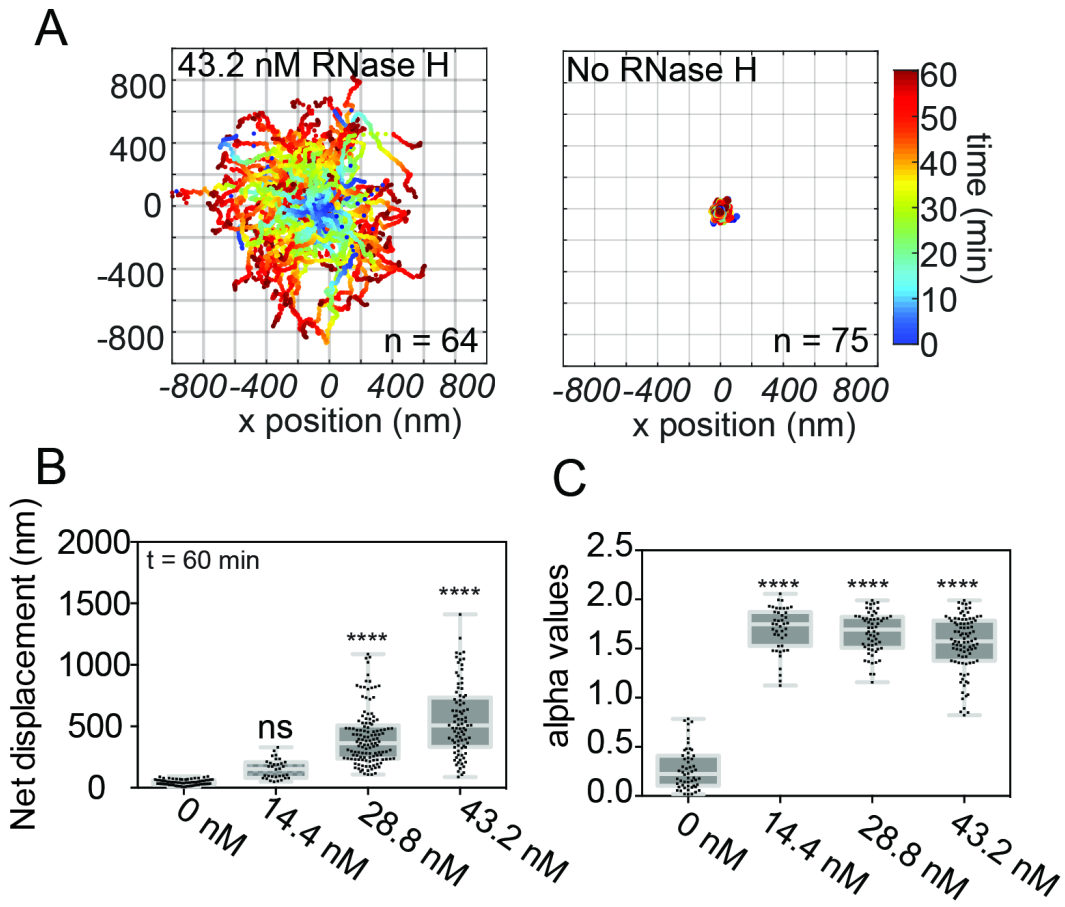

Figure 5-6. Effect of RNase H Concentration on 16HB Motor Movement. A) Over-lay of displacement of many 16HBs with starting point normalized to (0,0) in the presence (left) and absence (right) of RNase H. B) Box-whisker plot of net displacement of 16HB motors at different RNase H concentrations. C) Box-whisker plot of α values for 16HB motors at different RNase H concentrations. NS, $p > .05$, **** $p < .05$ compared to 0nM control.

5.5.1.3 Interrogating Mechanism of Motion with Geometric Mutants

To confirm the hypothesis that the mechanism of translocation of these origami nanostructures is indeed rolling and not walking, we created a library of origami structures with anisotropic display of RNA-binding domains across the 4 faces of the rectangular prism ('geometric mutations') (Figure 5-7). Structures were designed with between 1-4 faces modified with all 36 motor domains. For the 16HB2 design, we created two different isoforms - one in which the two modified sides were adjacent to each other ($16HB_{2Cis-36}$) and two opposite each other ($16HB_{2Trans-36}$). If motion primarily occurs through a walking/sliding mechanism, then motion should be identical as long as one face of the 16HB displays motor domains. However, if the major mechanism of motion is rolling, then 16HB with motor domains on multiple sides should show increased motility.

In our initial experiments, we found that only the $16HB_{4-36}$ structure exhibited any sustained motion, as it was the only structure with MSD significantly greater than the no-enzyme control. When imaging conditions more permissive of motor translocation were used (due to the introduction of formamide) all 5 motors showed significant displacement relative to no-enzyme controls. However, even in this permissive state, evidence of rolling behavior was still apparent. $16HB_{1-36}$ and $16HB_{2Cis-36}$, the two 16HB motors with the largest distance between neighboring motor domain-modified sides, showed motor behavior that was more consistent with general Brownian diffusion ($\alpha = 1$) than the super-diffusive directed motion seen with the other three structures. Furthermore, $16HB_{1-36}$ and $16HB_{2Cis-36}$ also exhibited the least processive movement with the smallest MSD relative to the other structures, which all showed similar behaviors.

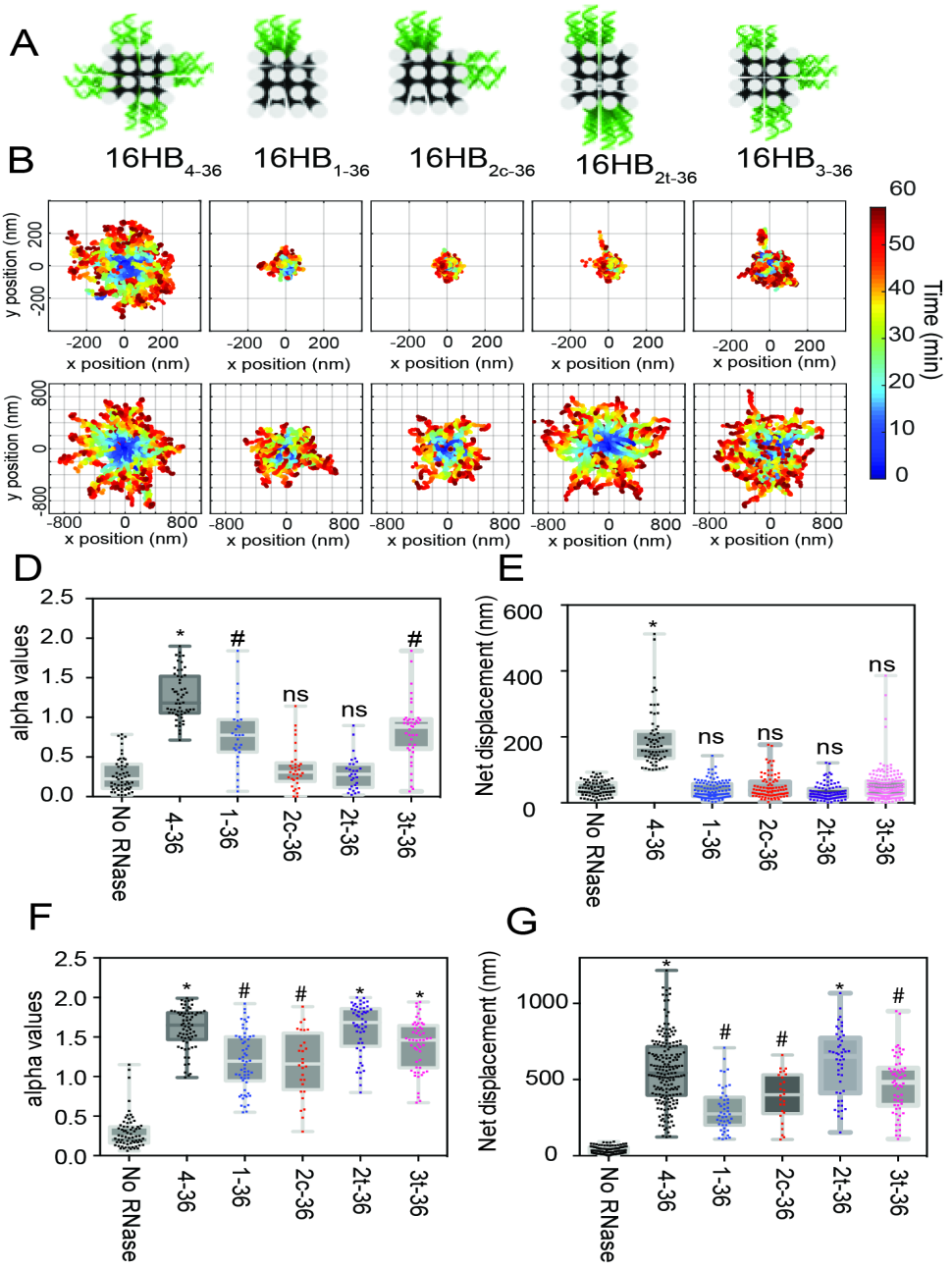

Figure 5-7. Analysis of Motor Behavior Using Geometric Mutants. A) 3D model of cross-section of 16HB geometric mutants showing distribution of motor domains. B,C) Over-lay of displacement of many 16HBs with starting point normalized to (0,0) for each design in the B) absence and C) presence of formamide. D,F) Box-whisker plot of α values for 16HB motors with different geometric mutations in the D) absence and F) presence of formamide. E,G) Box-whisker plot of net displacement for 16HB motors with different geometric mutations in the E) absence and G) presence of formamide. ns, $p > .05$, * $p < .05$ compared to -RNase H control, # $p<.05$ compared to 16HB4-36.

It is interesting that in permissive environments the geometric mutant structures were able to exhibit motion, as we had expected that the rolling motion would be required for significant displacement. $16HB_{2Trans-36}$ and $16HB_{3-36}$ both exhibited motion comparable to that of the full $16HB_{4-36}$ despite the fact that one or more sides were blank. We attribute this to the fact that there is likely some flexibility in the region of space which the ssDNA motor domains can sample, such that there is the possibility for strand to "wrap around" and bind to free RNA domains even when present on the top of the structure. This wrap around allows these structures to still participate in the rolling motion. For the $16HB_{1-36}$ and $16HB_{2Cis-36}$, the distance between neighboring motor regions is much larger (or non-existent) which hinders or prevents his phenomenon. As such, these motors cannot participate in rolling and thus display a slower crawling/walking behavior.

5.5.1.4 Design Parameters Affecting Motor Behavior

Having demonstrated that these DNA origami motors are capable of processively converting chemical energy to mechanical motion through a cog-and-wheel translocation mechanism, we next sought to further analyze parameters governing this rolling motion. In particular, we were interested in investigating the relative effects of the total number of DNA legs (polyvalency) vs the relative spatial distribution of these legs (density). We created a library of DNA origami structures which decoupled polyvalency/density, such that different numbers DNA legs could be non-uniformly distributed along the surface of the motors (Figure 5-8). This allowed us to create motors with different polyvalency but constant density ($16HB_{4-9}$, $16HB_{4-9+9}$, $16HB_{4-18}$) and those with lower density ($16HB_{4-12}$, $16HB_{4-24}$). While all motors did show processive movement along the RNA-coated surface, there were some small differences between the groups. In general, it appears that all

structures still exhibit rolling motion, with comparable α values indicating super-diffuse motor behavior. The structure with the split binding domain ($16HB_{4\text{-}9+9}$) demonstrated the smallest α coefficient, which could be contributed to loss of coherence between the two different domains. Correspondingly, this structure also exhibited decreased MSD relative to the control 16HB. The 16HB motor with the lowest density ($16HB_{4\text{-}12}$) also exhibited decreased mobility despite having a similar α value. This is consistent with data obtained using imaging conditions without formamide, in which structures with decreased density had decreased mobility. We hypothesize that this is due to decreased relative motor domain density relative to RNA strand density, which we approximate to be ~4.5 strands/200 nm^2. If the motor domain density drops below this (as with the 2 strands/200 nm^2 of $16HB_{4\text{-}12}$), motor strands can bind to adjacent DNA strands within the same vicinity after RNase H activity. It is only after all the RNA has been cleaved beneath the 16HB that sampling of a new region of RNA via rolling can occur. On the other side of the spectrum, $16HB_{4\text{-}9}$ - showed the largest and most consistent MSD. This could be due to the fact that less RNase H activity is needed before rolling is induced.

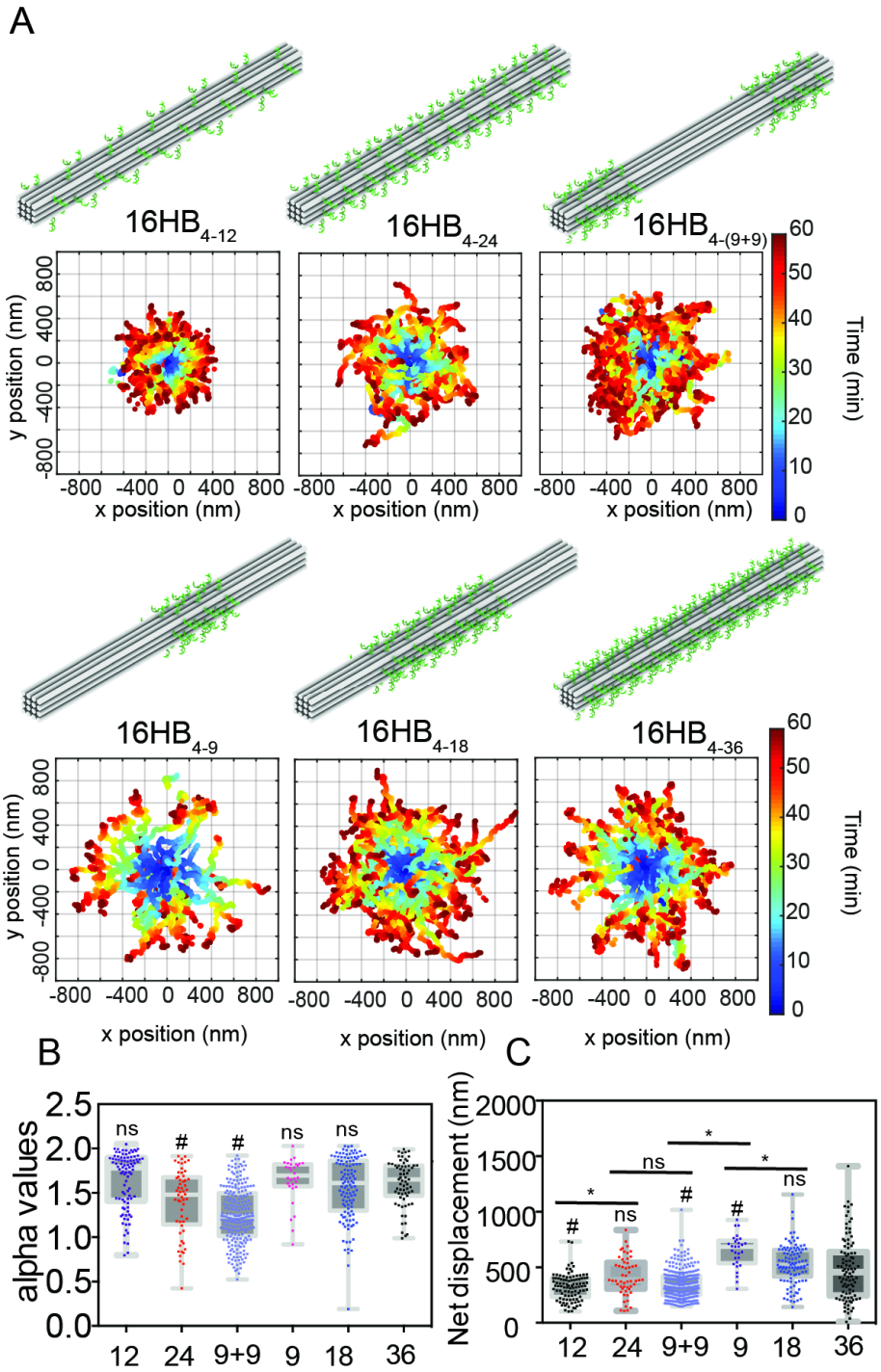

Figure 5-8. Effect of Motor Domain Distribution on Locomotion. A) 3D models (top) and over-lay of displacement of many 16HBs with starting point normalized to (0,0) (bottom) for 16HB with different motor domain placement. B) Box-whisker plot of α values for 16HB motors with different motor domain placement C) Box-whisker plot of net displacement for 16HB motors with different motor domain placement. ns $p > .05$, # $p < .05$ compared 16HB4-36 control * $p < .05$.

Finally, we hypothesized that increased flexibility of the 16HB could limit movement. We used the 16HB motors which had staple strands removed, producing a ssDNA region which led to increased flexibility within the structure (Figure 5-9). We found that these DNA origami motors still exhibited processive motion. However, these structures had smaller α coefficients and decreased MSD relative to the rigid 16HB motors, which implies that rigidity of the motor plays a role in mechanism of motion. This reduced motion could be due to a loss of coherence between motor domains on either end of the gap – if one region attempts to move in one direction while the other half moves in another, the overall directionality and velocity of the motors could be decreased.

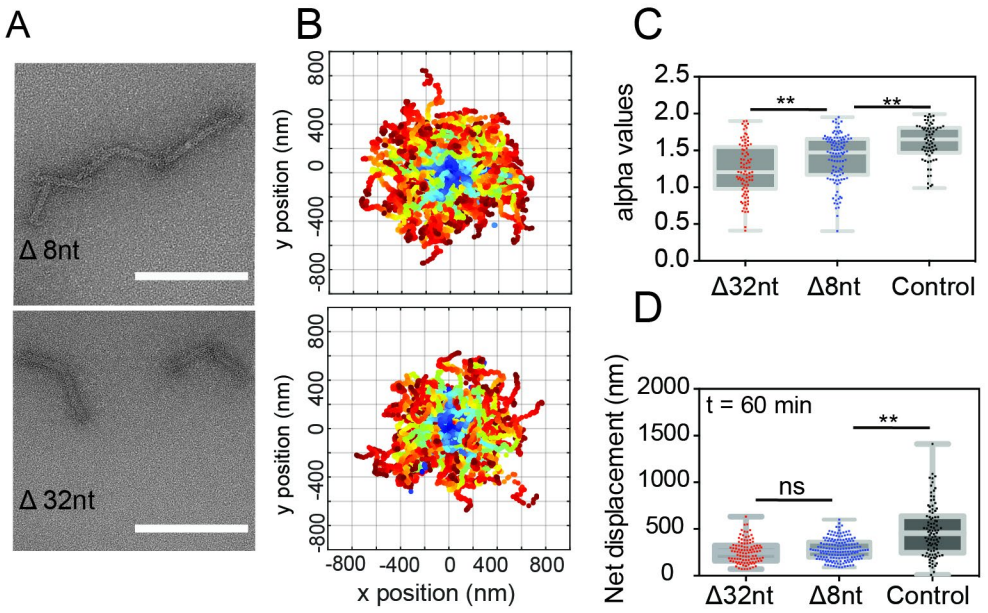

Figure 5-9. Effect of 16HB Motor Flexibility on Locomotion. A) Representative TEM images of flexible 16HB motors with either 8-nt (top) or 32-nt (bottom) gaps. Scale bar - 200 nm. B) Over-lay of displacement of many 16HBs with starting point normalized to (0,0) of 16HB motors with either 8-nt (top) or 32-nt (bottom) gaps. C) Box-and-whisker plot of fit alpha values for 16HB motors with 8-nt, 32-nt or no gaps. D) Box-and-whisker plot of net displacement for 16HB motors with 8-nt, 32-nt or no gaps. ns $p > .05$, ** $p < .05$.

5.6 Conclusions and Future Directions

We have created the first DNA origami motor which processively converts chemical energy into mechanical motion and the first nanoscale motor to exhibit the cog-and-wheel rolling behavior. These motors are processive over multiple hours and can move micron-scale distances with max velocities of 200 nm/min, significant improvements over canonical DNA molecular motors. The DNA origami motors also are the first to display autonomous, directed motion in the absence of external factors, such as magnetic fields or track patterning. By taking advantage of the unique addressability of DNA origami, we were able to provide evidence that the primary mechanism of motion is this rolling behavior and not walking through the selective engineering of geometric mutants. We were also able to investigate how various physical properties of the motor affect their locomotion. The kinetics of these DNA origami motors is related to the density of motor domains and is likely related to the relative density matching between these domains and the RNA track - if RNA strands are present in higher abundance than DNA strands the motor displacement is decreased. Additionally, it appears that localizing motor domains to a smaller region at a constant density leads to enhanced motor efficiency. Finally, the rigidity of the DNA motor is an important factor in determining directed motion, as structures with engineered flexibility exhibited diminished directionality and kinetics. The insights gleaned from this study will help to facilitate the design of the next generation of molecular motors with enhanced processivity, directionality, and velocity. These motors are promising for use in a number of applications, including DNA computing, biosensing, and molecular robotics.

Future work should first be focused on validating that the same behavior is observable with other DNA nanostructures, and not just the 16HB rod. The design of new structures will also allow us to further validate the effect of density and polyvalency observed here, along with the investigation of new factors. For example, it would be interesting to see how the shape of the DNA origami motors impacts locomotion - how would using rods with different diameters alter the kinetics and directionality? Would the use of spherical particles rather than rods alter the directionality that was observed? Future work should also be directed to developing applications for these motors. Given that we already have designed strategies for carrying cargo, it would be interesting to show the ability for these motors to pick and a deliver cargo in an autonomous manner.

APPENDIX A. CADNANO DESIGN FILES AND STRAND LIST

A.1 16HB Design for IONP Binding

Figure A.1: Schematic of 16HB staple extension design showing 12 binding sites of 3 strands each.

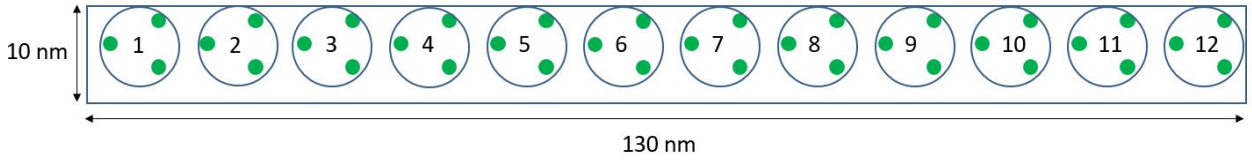

Figure A.2: caDNAno Design of 16HB: (staples colored in red correspond to binding sites on side 1, blue for side 2, green for side 3, and yellow for side 4). Grey strands correspond to staples without 5' extensions on the faces of the 16HB, while the long blue strand corresponds to the p7560 scaffold.

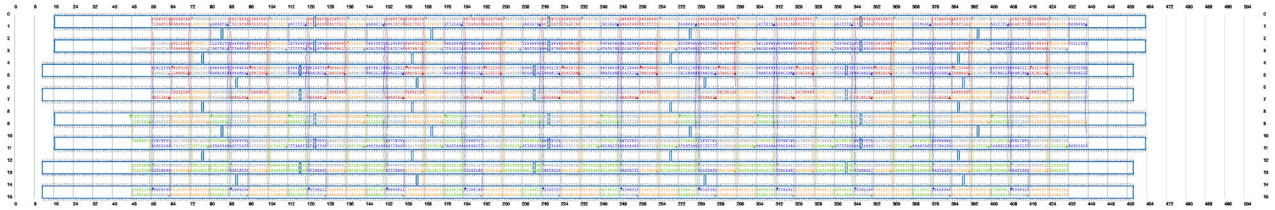

Figure A.3: Design of 16HB Dimerization Strands: Dark blue – bridging strands with 5bp overhand. Light blue – filler strands

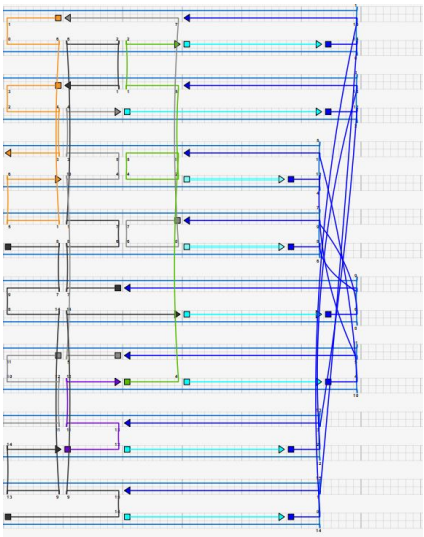

A.2 16HB Design for Molecular Motor

Figure A.4: 16HB caDNAno files for 16HB molecular motor. Blue: p7560 scaffold strand. Red – Cargo-carrying strands. Grey – Unmodified Staple. Green – Staple modified with RNA binding 'motor' domain.

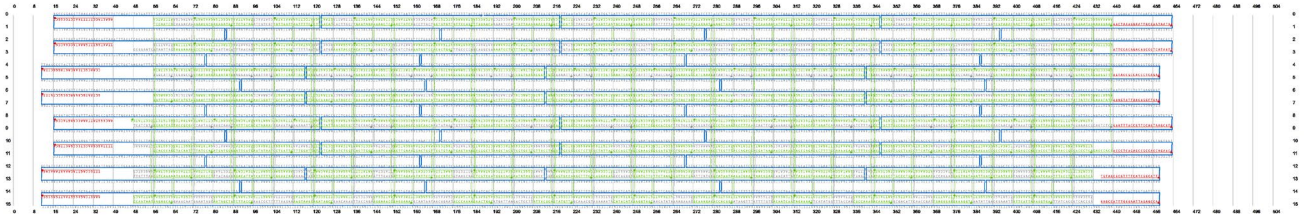

Figure A.5: Design of Flexible 16HB Motors. Top: 8nt gap. Bottom – 32nt Gap

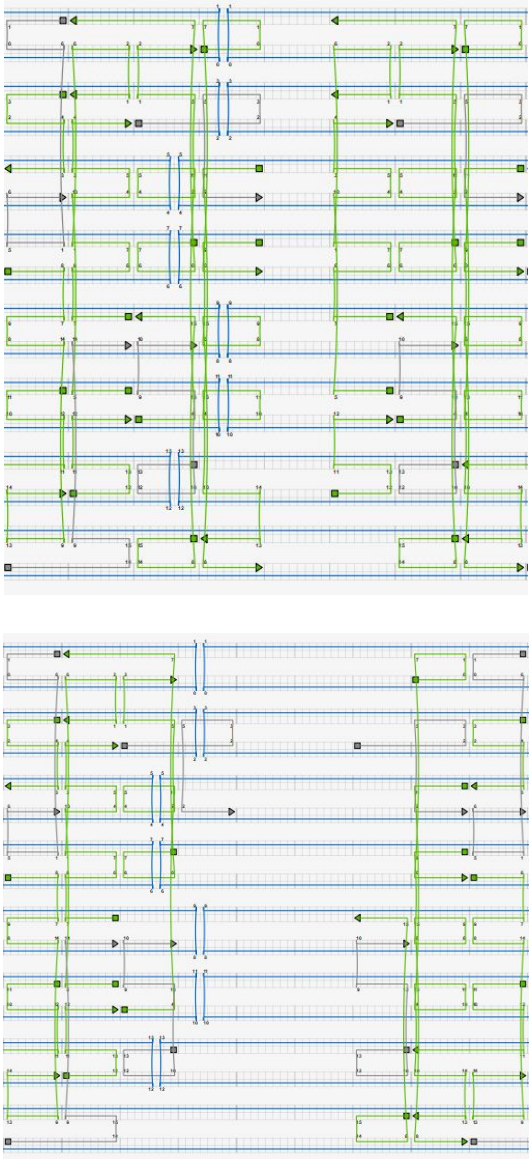

A.3 16HB Staple List

Start	End	Sequence
0[71]	5[71]	AATAGTGACAAGACAAAATTCTGTTCGAGCCA
0[103]	5[103]	CGATAGCTATCGTCGCACAAAATCGAATTATT
0[135]	5[135]	TTTGATTACACTTGCCGAATGGCTTGGCCAAC
0[167]	5[167]	ATCACGCAGCCTTGCTGGTTAAGAAAGCGTTG
0[199]	5[199]	AACCGTCTAGAGTCCAATTAATGATCTTTTCA
0[231]	5[231]	ATATGATACTAGCTGAGAGTAACAGCATTAAA
0[263]	5[263]	GAGAAAGGTATTTTTGGTAGCCAGTAACCAAT
0[295]	5[295]	TGAGTAATTCGGTTGTATTGCTGAGTAGCTCA
0[327]	5[327]	TTAGAACCTACTTTTGAGAGGTCAGTACGGTG
0[359]	5[359]	CCGATAGTATGACAACCTCATCTTAAATACGT
0[391]	5[391]	CTTTCGAGATATTCGGAGGCGAAATAAAAGTT
0[423]	5[423]	GGAGCCTTAGCGGAGTTGCTCAGTTGTATCAC
3[48]	5[63]	CCGGAATCATAATTACTTAATTTCAGGCATTT
3[80]	5[95]	TAATTACATTTAACAAGTGAATAAAAGGAGGC
3[112]	5[127]	TTTTTTAATGGCATGGACGCTAAAGGACATTC
3[144]	5[159]	ACGCTCAATCGTCTGACAATATTATGACCTGA
3[176]	5[191]	TTGCCCCAGCAGGCGAAATAGCCCGTGGTTTT
3[208]	5[223]	TGGTTCCGAAACGTAAGTAATTCGTAAAATTC
3[240]	5[255]	ATATGTACCCCGGTTGGAGTCTGGTCATTTTT
3[272]	5[287]	TCAATAACCTGTTTAGAGCCTCAGATAATGCT
3[304]	5[319]	GGCGCGAGCTGAAAAGCAAGGCAACAACTAAA
3[336]	5[351]	TAATAGTAGTACAGCAACCCTGCAAACGGGTA
3[368]	5[383]	GAACGAGGGTAGCAACAGGGAGTTCACCAACC
3[400]	5[415]	ACTGAGTTTCGTCACCATTTTCTGGGAATAGG
12[55]	9[55]	GAGCGTCTTTGTTTAACTAAGAACTCATCGTA
12[87]	9[87]	TTCCTGATTTACAGAGCAAAATCAAAGCAAAT
12[119]	9[119]	TAACCACCAGAAATAGCTGAATAAAGAAATTG
12[151]	9[151]	TTATCTAAATTTGAGGCTTGCTGAGTGCCACG
12[183]	9[183]	ATTTCTCCGTAAGCAACGTAATCATGTTTCCT
12[215]	9[215]	GACTGAATGGCCTGGCGACGGAGGATTCCACA
12[247]	9[247]	CCAGGGTTGCCAGGGTGCTGCGCACTCCAGCC
12[279]	9[279]	GTAAGAGCATTCATGCGAAAACCACCGGATCC
12[311]	9[311]	ATACATAACAACATTACCAATACTGAAAACGA
12[343]	9[343]	CAGTTTAGTGAGATGAGGTAATAGGTCTTTAC
12[375]	9[375]	TTACCCAAACCAGAACACAGATGAAGACGGTC
12[407]	9[407]	CCGGAACCTAGCGACACTTGATATATAAATCC
15[64]	9[79]	GAAACAATGAAATAGCACAGGGAACCAATAGC
15[96]	9[111]	AAGCCCTTTTTAAGAATAATTTTAAGAAATAA
15[128]	9[143]	GAACAAAGTTACCAGAAACTCGTACTGCAACA

15[160] 9[175] GCAATAATAACGGAATCGACAGTGAATATAGC
15[192] 9[207] ATGATTAAGACTCCTTTTTACGCTCGCTCACA
15[224] 9[239] GCAAACGTAGAAAATATGTCCCGCAGATCGCA
15[256] 9[271] AACATATAAAAGAAACTCCTTAGTTTCTGGTG
15[288] 9[303] ATAAGTTTATTTTGTCGTTGGGAAACAGTTCA
15[320] 9[335] TCATATGGTTTACCAGTTTAAGAAAAAATCAG
15[352] 9[367] GCGACATTCAACCGATAACTTTAACGAGGCGC
15[384] 9[399] AATATTGACGGAAATTTCGATAGCAACAACAA
15[416] 9[439] TTATCACCGTCACCGATAGCAAGGGGAAAGCGCAGTCTCT
6[87] 0[72] CGACAAAACATCGGGAGACGCTGAGAAGAGTC
6[119] 0[104] TTATGAATTGCTTATGATCCTTGAAAACATAG
6[151] 0[136] CACAGACACGCCATTAGTTGTAGCAATACTTC
6[183] 0[168] ACGCGCGGGTTGCGCTGTAAAAGAGTCTGTCC
6[215] 0[200] GATTCGTGACCTGTCTACGTCAAAGGGCGAAA
6[247] 0[232] AACATTAACCGTAATGAGTCAAATCACCATCA
6[279] 0[264] CGCGTCTGTTCGAGCTAAAGATTCAAAAGGGT
6[311] 0[296] GATGGCTTAACTCCAATTTTAAATGCAATGCC
6[343] 0[328] AGCGCTCCTAATTGATGCAAGGATAAAAATTT
6[375] 0[360] AGAATACAAACGGAGACTTAAACAGCTTGATA
6[407] 0[392] GATAAGTGTGCCCCCTTCGGTTTATCAGCTTG
6[439] 0[424] AGGATTAGGAAACATGAAAAAAGGCTCCAAAA
11[80] 1[87] ATGATGGCCAAGAAAAAGAATATACCTACTTTAGAAATGC
11[112] 1[119] TTTGGATTTAATGAGCTTACCAAGCAGTACATAATTTTCC
11[144] 1[151] AAATCAACATTGGCAGAACCCTTCCCGCCAGCAGAACTCA
11[176] 1[183] TGAGTAAACCTGAGAGGCGCCAGGGAGATAGGGTTCCAGT
11[208] 1[215] GTTACCTCTTTCAACAACGGGTGTGCAAAATCGAACGTGG
11[240] 1[247] GCCAGCTGATAAGCAAAAATCAGCAGCAAACATGCCGGAG
11[272] 1[279] ATCATAACCATTTCGCCATCAAAAAGCGGCTAACAAAATA
11[304] 1[311] AACCAAAACGAACGAGTAAATATGAGAATTAGCATTATGA
11[336] 1[343] GTTTTGCCCCATTCCATTTCATTATTAACATCGCCTTTAT
11[368] 1[375] AGAGTAATTGAGGACTTACGAAGGAAAGGCCGCCCACGCA
11[400] 1[407] CAGAGCCGATAGCAAGTATAGCCCTATGGGATAACTTTCA
11[432] 1[439] GAGCCACCCACCCTCAGGAGGTTTGTCTTTCCAAAGGAAC
8[79] 2[72] CTTCAATCGAAACTTAGGTAAAGTAGAACGCGTTCAAATA
8[111] 2[104] TTTAACGTCGCCTGATACCAAGTTTATTAATTAAATCAAT
8[143] 2[136] AAAACAGATAAAACATATATTTTTTGAGTAGACATTGCAA
8[175] 2[168] TGAGTGAGTTAATTGCGGAGAGGCGGTGTGTTGTTGAAAT
8[207] 2[200] GAAGCATAGTCGGGAACCAGCTGCCTATTAAACCTTATAA
8[239] 2[232] GTTTGAGGCGGATTGAATGTGAGCTAAATTAAAGAGAATC
8[271] 2[264] TTTATGGGTGTAGTAAGCCTTCCTAGAGATCTTCAGGTCA
8[303] 2[296] AAGAGGAACGGAAGCAAGAGCTTAACCAAAAACAAAATTA
8[335] 2[328] TCAGAAGCAGTACCTTTTTTGATACGGGAGAACAATAAAT
8[367] 2[360] AATCCGCGCAAAGTACCTAAAACAAACCATCGCTTTTGCG

8[399]	2[392]	GTAACAGTACAGTTAACCGTCGAGTCGTAAACTTTGCCTG
8[431]	2[424]	GGTAATAAATTATTCTCGGGGTTTGAGAATAGAGACGTTA
10[79]	3[79]	GATATAGAGTAATAAGCAATTTAGGCCTGAAT
10[111]	3[111]	TGGAAGGGCATTTCAAAAAAGAAGGAATTACC
10[143]	3[143]	ACCTCAAAAGAGATAGATTCACCAACATTTTG
10[175]	3[175]	TGGTCGAACGTATTGGAGTTGCAGACGCTGGT
10[207]	3[207]	ATCCCCGGCCAGTGAGGCTGATTGTTTGATGG
10[239]	3[239]	ACTGTTGGTTTTTGTTATATTTAATGTCAATC
10[271]	3[271]	GGCAAAGCAGGAACGCAAACCCCAAAAAGTGG
10[303]	3[303]	GCGGAATCACATGTTTTAGATTTATCATTTGG
10[335]	3[335]	TAAAATGTTCTGGAAGTATAACAGAATTCTAC
10[367]	3[367]	ACGGTGTAAATGCCACAAAGACTTCAGCATCG
10[399]	3[399]	TCACATGAGATATAAGCCCAATAGACCGTAAC
10[431]	3[431]	GTTGAGGCCGTACTCAGAGCCACCCTACAACG
2[71]	4[64]	TATTTTAGTAGAAAAATATCATAT
2[103]	4[96]	ATATGTGATTTCATTTATGATGAA
2[135]	4[128]	CAGGAAAAAAATACCTGTCACACG
2[167]	4[160]	ATCCAGAAAATGGTCCCAAGCGGA
2[199]	4[192]	ATCAAAAGAAATCCTGCCCTTCAC
2[231]	4[224]	GATGAACGAACTAGCAATTGTAAA
2[263]	4[256]	TTGCCTGAATAATCAGAAAACAGG
2[295]	4[288]	AGCAATAACTATATTTGTTTGACC
2[327]	4[320]	CATACAGGGTGGCATCTTGATTCC
2[359]	4[352]	GGATCGTCGCGAAAGATTTCATGA
2[391]	4[384]	AGGCTTGCGGCCATGTGAACCTAC
2[423]	4[416]	GTAAATGAAGTACAAAACCCTCAT
13[72]	11[79]	AGCAGCCTTATCTGAATTATCCAG
13[104]	11[111]	CGGAACAAAGAAGGAGCCTGATTG
13[136]	11[143]	GATAATACAATATCTTCAGTTGGC
13[168]	11[175]	TGCCATCTGAACTCTGTGGTGTAA
13[200]	11[207]	AATATAGGCGGCTGACTGGTGCTT
13[232]	11[239]	CAGGAGAATTCCCAGTGCTATTAC
13[264]	11[271]	GGTTGTGAAACAGGCGCTGCAACT
13[296]	11[303]	TAACGGAACGCCAAAAACGATAAA
13[328]	11[335]	TCATCAGTGAATACCACAAAAGAA
13[360]	11[367]	CGAGAAACATCAACGTCTTCATCA
13[392]	11[399]	GTAATCAGAGAGCCACGCCTCCCT
13[424]	11[431]	TAGCGTCAGCCATCTTCACCCTCA
10[71]	12[56]	AGGCTTATCTACAATTTCTTACCAACGCTAAC
10[103]	12[88]	TTAGAACCAATATAATCGGAATTATCATCATA
10[135]	12[120]	TATCAAACTATCTGGTTAGGAGCACTAACAAC
10[167]	12[152]	AAATCTAAGGACTGGTACCTCATTGAGGAAGG
10[199]	12[184]	GTACCGAGAAGCTACGGCATTTCACATAAATC

10[231] 12[216] GAAGGGCGGCCTCTTCCACGACGTTGTAAAAC
10[263] 12[248] GCCATTCGGGGATGTGATTAAGTTGGGTAACG
10[295] 12[280] GTCATAAAACCAGACGGGAATTACGAGGCATA
10[327] 12[312] TTAGACTGGGCTTTTGCATTCAACTAATGCAG
10[359] 12[344] CAGACCAGTGGCTGACAACAAAGCTGCTCATT
10[391] 12[376] CCAACTTTGAAGAACCCACCGCCGGATATTCA
10[423] 12[408] AGGTCAGAAGAACCGCTTCATAATCAAAATCA
7[64] 13[71] AGCATGTAAATAATCGTACCGCGCGCGCATTAATGAAAAT
7[96] 13[103] AACGGATTCAGATGAACGTAAAACAAAGTTTGTCATTTTG
7[128] 13[135] GATAGCCCGGTGAGGCAACACCGCTTAAATCCCGTCAATA
7[160] 13[167] GAATCACACTAACCGACAGCAGCACGGAGACTGTATTCCC
7[192] 13[199] GCTTTCCAAAGTGTAATTGTTATCCGCCCTGGTGGGCACG
7[224] 13[231] ACAAACGGGGACGACGCCTCAGGACAAAATAAAGCTTTCT
7[256] 13[263] CACGTTGGCGCATCGTGGCACCGCGCTGAATTTTCTAAGT
7[288] 13[295] AACCAGACGCCCGAAATGCTTTAAGAAAAATCAAACGAAC
7[320] 13[327] GATTAGAGAAAGCGGAATAAATCACTGGCTCAAGAAAGAT
7[352] 13[359] GCGCGAAAACCTGCTCAGCCGGAATCATTGTGTGCCCTGA
7[384] 13[391] ATCTATAAGCCCGGCCGGGAACCGAGCGGCTTAATTGACC
7[416] 13[423] CGGAACCTGTTTTAACGCCAGAATCCGGAAACTTTGCCTT
4[63] 14[56] GCGTTATAGCACCCAGCCGGTATTCGTCAAAAGACGGGAG
4[95] 14[88] ACAAACATAATTCATCTACCATATAGACATTAAGTAAATA
4[127] 14[120] ACCAGTAAATAATCAACCTCACTTATTAGAGCTTTGCCCG
4[159] 14[152] TTATTTACAGTTGAAAAGCATCACATTTAGAATTACAAAC
4[191] 14[184] CGCCTGGCCAGGGCTTCTCGAATTCTCGTCGGAGTGACTC
4[223] 14[216] CGTTAATAGATTGCGGATCGGAAACAGTGCCACCCCGCTT
4[255] 14[248] AAGATTGTGCGAAAGGCCATTCAGGGATGTTCGTCAACCT
4[287] 14[280] ATTAGATACCTCGTTTTATTCATTGCATAATATACGTCGA
4[319] 14[312] CAATTCTGTAGCGAGAGATAGCGTTTACAGGTTTATACCA
4[351] 14[344] GGAAGTTTAGATAGGCGCGCAGGGATAAGGCTAATTACCT
4[383] 14[376] AGAGGCTTCTTGACAAGAAAGAGGGAGTAGTAGAGATGGT
4[415] 14[408] TTTCAGGGCCACCCTCCGATTGGCGAATCAAGGTCACCAA
6[63] 15[63] CCAGACGAGGAATCATGCTGTCTTAAGAGCAA
6[95] 15[95] GCGCATACTATTTGCATATACAGTTCTTACCG
6[127] 15[127] ATTAGTCTCGTGTATTGGTCAAGAAGATAGCC
6[159] 15[159] ATACGTGGCTGAGAGCACCACCAGGAGGAAAC
6[191] 15[191] ATCGGCCAGTGTGAAAAGCCTGGGGAACTGGC
6[223] 15[223] ACCCGTCGCAAATCGGACAGTCATGTATGTTA
6[255] 15[255] CTTTCATCAGCTTTCCAACCGTGCAAGGTGGC
6[287] 15[287] ATATAATTCCCTCAAAGACTTCAAACCACGGA
6[319] 15[319] TTTTTGCGGAATGACCTTGCATCATAGAAAAT
6[351] 15[351] TGACCCCCCCTTACTTCATGTGACACAAAAGG
6[383] 15[383] GAGGCAAAAATCATAATGATAAATGGAAGGTA
6[415] 15[415] ACCAGGCGTCATTAAAGGGGTCAGAAGGTGAA

14[55]	8[47]	AATTAACTCCAATAATTCCTTATCA
14[87]	8[80]	ACATAAAAAATAGCTAAACAGTAC
14[119]	8[112]	AACGTTATAAGTAAGCTTTTCAGG
14[151]	8[144]	AATTCGACAGGAAACCCAGAAGAT
14[183]	8[176]	TATGATACACCCAAAAGTGCCTAA
14[215]	8[208]	CTAATCTAATTACGCAACGAGCCG
14[247]	8[240]	TATGACAACATACATAATCTGCCA
14[279]	8[272]	CTTAAGTGGCAAAGACATATCGCG
14[311]	8[304]	GTCAGGACACAATCAAAAAAGATT
14[343]	8[336]	TATGCGATCGCCAAAGTATTATAG
14[375]	8[368]	TTAATTTCTGAGGGAGTGTGTCGA
14[407]	8[400]	TGAAACCAATTCATTATGCCTTGA
1[56]	7[63]	TCCAATCGATTTATCAAATTTACG
1[88]	7[95]	TTCTGTAATAGATTAAGAAACAAT
1[120]	7[127]	CTTAACATGTAATAGACGCGAACT
1[152]	7[159]	AACTATCGAATTAACCAAAATACC
1[184]	7[191]	TTGGAACAATCACCGACACTGCCC
1[216]	7[223]	ACTCCGTTTTCAACCACCGTGGGA
1[248]	7[255]	AGGGTAGCCCGGAGACGGATAGGT
1[280]	7[287]	AAGCTAAAGTGTAGGTTCAAAGCG
1[312]	7[319]	CCCTGTAACTCATATACAGGTCAG
1[344]	7[351]	TTCCGACATGCGCAACTATACCAA
1[376]	7[383]	TAACCGATGTGAATTTTTTGTATC
1[408]	7[415]	ACAGTTTCTAATTGTAGCCTATTT
0[463]	0[440]	TTTTTTCACGTTGAAAATCTCCAA
2[463]	2[440]	AGCGTAACGATCTAAAGTTTTGTC
4[458]	4[440]	CCGCCACCCTCAGAACCGC
6[458]	6[440]	ACTCCTCAAGAGAAGGATT
8[463]	8[440]	ATACATGGCTTTTGATGATACAGG
10[463]	10[440]	ACCACCAGAGCCGCCGCCAGCATT
12[458]	12[435]	TCGGTCATAGCCCCCTTATTAGCG
14[458]	14[435]	CAAAATCACCAGTAGCACCATTAC
1[16]	1[47]	TAGGTTGGGTTATATAACTATATGTAAATGCT
3[16]	3[47]	GTGATAAATAAGGCGTTAAATAAGAATAAACA
5[11]	5[43]	TTGAGAATCGCCATATTTAACAACGCCAACATG
7[11]	7[43]	TCAACAATAGATAAGTCCTGAACAAGAAAAATA
9[16]	9[47]	ACTCATCGAGAACAAGCAAGCCGTTTTTATTT
11[16]	11[47]	GGAGGTTTTGAAGCCTTAAATCAAGATTAGTT
13[11]	13[43]	CATATTATTTATCCCAATCCAAATAAGAAACGA
15[11]	15[43]	AATATCAGAGAGATAACCCACAAGAATTGAGTT

A.4 Additional Sequences

ID	Sequence (5'-3')
16HB-IONP Sequences	
IONP Strand	CTC TCT CTC TCT CTC TCT CT - DBCO
IONP Capture	AG AGA GAG AGA GAG AGA GAG – Origami Staple
Bead Anchor 1	AAA GTC AGA GGG TAA TTG AGC GCT CTG GCT TGC CAA AAA AAA AAA AA
Bead Anchor 2	AAC GGG TAT TAA ACC AAG TAC CGC CTG GCT TGC CAA AAA AAA AAA AA
Bead Anchor 3	CCA ACG CTC AAC AGT AGG GCT TAA CTG GCT TGC CAA AAA AAA AAA AA
Bead Anchor 4	TTA ATG GTT TGA AAT ACC GAC CGT CTG GCT TGC CAA AAA AAA AAA AA
Release Strand	TTT TTT TTT TTT TTT GGC AAG CCA G
16HB-Motor Sequences	
DNA anchor	5AmMC6/GA GAG AGA TGG GTG CTT TTT TTT TTT TTT T/35OctdU/
RNA/DNA chimera substrate	GCACCCATCTCTCTCrCrCrCrCrCrCrUrGrUrGrArUrUrGrArUrUrArCrU /3Cy3Sp/
DNA Motor Strands	Origami Staple – TTT-AGTAATCAATCACAG

Cargo Strands	ATACATCTACTGTCGTGCCTC – Origami Staple
AF647 Strand	GAGGCACGACAGTAGATGTAT /3AlexF647N/

REFERENCES

1. Wang, P., et al., *The Beauty and Utility of DNA Origami.* Chem, 2017. **2**(3): p. 359-382.

2. Seeman, N.C., *DNA in a material world.* Nature, 2003. **421**(6921): p. 427-31.

3. Stulz, E., *DNA architectonics: towards the next generation of bio-inspired materials.* Chemistry, 2012. **18**(15): p. 4456-69.

4. Stulz, E. and G.H. Clever, *DNA in supramolecular chemistry and nanotechnology*. 2015, Chichester, West Sussex, UK: John Wiley & Sons, Inc. xxi, 500 pages.

5. Seeman, N.C., *Nucleic acid junctions and lattices.* J Theor Biol, 1982. **99**(2): p. 237-47.

6. Chen, J.H. and N.C. Seeman, *Synthesis from DNA of a molecule with the connectivity of a cube.* Nature, 1991. **350**(6319): p. 631-3.

7. Ke, Y., et al., *Three-dimensional structures self-assembled from DNA bricks.* Science, 2012. **338**(6111): p. 1177-83.

8. Rothemund, P.W., *Folding DNA to create nanoscale shapes and patterns.* Nature, 2006. **440**(7082): p. 297-302.

9. Castro, C.E., et al., *A primer to scaffolded DNA origami.* Nat Methods, 2011. **8**(3): p. 221-9.

10. Hong, F., et al., *DNA Origami: Scaffolds for Creating Higher Order Structures.* Chemical Reviews, 2017. **117**(20): p. 12584-12640.

11. Ke, Y., et al., *Scaffolded DNA origami of a DNA tetrahedron molecular container.* Nano Lett, 2009. **9**(6): p. 2445-7.

12. Andersen, E.S., et al., *Self-assembly of a nanoscale DNA box with a controllable lid.* Nature, 2009. **459**(7243): p. 73-6.

13. Douglas, S.M., et al., *Self-assembly of DNA into nanoscale three-dimensional shapes.* Nature, 2009. **459**(7245): p. 414-8.

14. Douglas, S.M., et al., *Rapid prototyping of 3D DNA-origami shapes with caDNAno.* Nucleic Acids Res, 2009. **37**(15): p. 5001-6.

15. Ke, Y., et al., *Multilayer DNA origami packed on a square lattice.* J Am Chem Soc, 2009. **131**(43): p. 15903-8.

16. Ke, Y., et al., *Multilayer DNA origami packed on hexagonal and hybrid lattices.* J Am Chem Soc, 2012. **134**(3): p. 1770-4.

17. Dietz, H., S.M. Douglas, and W.M. Shih, *Folding DNA into Twisted and Curved Nanoscale Shapes.* Science, 2009. **325**(5941): p. 725-730.

18. Han, D.R., et al., *DNA Origami with Complex Curvatures in Three-Dimensional Space.* Science, 2011. **332**(6027): p. 342-346.

19. Endo, M., et al., *Regulation of DNA methylation using different tensions of double strands constructed in a defined DNA nanostructure.* J Am Chem Soc, 2010. **132**(5): p. 1592-7.

20. Yamamoto, S., et al., *Single molecule visualization and characterization of Sox2-Pax6 complex formation on a regulatory DNA element using a DNA origami frame.* Nano Lett, 2014. **14**(5): p. 2286-92.

21. Endo, M., et al., *Single-molecule visualization of the hybridization and dissociation of photoresponsive oligonucleotides and their reversible switching behavior in a DNA nanostructure.* Angew Chem Int Ed Engl, 2012. **51**(42): p. 10518-22.

22. Endo, M., et al., *A versatile DNA nanochip for direct analysis of DNA base-excision repair.* Angew Chem Int Ed Engl, 2010. **49**(49): p. 9412-6.

23. Suzuki, Y., et al., *DNA origami based visualization system for studying site-specific recombination events.* J Am Chem Soc, 2014. **136**(1): p. 211-8.

24. Raz, M.H., et al., *Torsional Constraints of DNA Substrates Impact Cas9 Cleavage.* J Am Chem Soc, 2016. **138**(42): p. 13842-13845.

25. Rajendran, A., et al., *Controlling the stoichiometry and strand polarity of a tetramolecular G-quadruplex structure by using a DNA origami frame.* Nucleic Acids Res, 2013. **41**(18): p. 8738-47.

26. Rajendran, A., et al., *Direct and single-molecule visualization of the solution-state structures of G-hairpin and G-triplex intermediates.* Angew Chem Int Ed Engl, 2014. **53**(16): p. 4107-12.

27. Rajendran, A., et al., *HIV-1 nucleocapsid proteins as molecular chaperones for tetramolecular antiparallel G-quadruplex formation.* J Am Chem Soc, 2013. **135**(49): p. 18575-85.

28. Sannohe, Y., et al., *Visualization of dynamic conformational switching of the G-quadruplex in a DNA nanostructure.* J Am Chem Soc, 2010. **132**(46): p. 16311-3.

29. Rajendran, A., et al., *Direct and real-time observation of rotary movement of a DNA nanomechanical device.* J Am Chem Soc, 2013. **135**(3): p. 1117-23.

30. Ke, Y., et al., *Self-assembled water-soluble nucleic acid probe tiles for label-free RNA hybridization assays.* Science, 2008. **319**(5860): p. 180-3.

31. Zhang, Z., et al., *Asymmetric DNA origami for spatially addressable and index-free solution-phase DNA chips.* Adv Mater, 2010. **22**(24): p. 2672-5.

32. Ke, Y., et al., *Regulation at a distance of biomolecular interactions using a DNA origami nanoactuator.* Nat Commun, 2016. **7**: p. 10935.

33. Kuzuya, A., et al., *Allosteric control of nanomechanical DNA origami pinching devices for enhanced target binding.* Chem Commun (Camb), 2017. **53**(59): p. 8276-8279.

34. Kuzuya, A., et al., *Nanomechanical DNA origami 'single-molecule beacons' directly imaged by atomic force microscopy.* Nat Commun, 2011. **2**: p. 449.

35. Marras, A.E., et al., *Programmable motion of DNA origami mechanisms.* Proc Natl Acad Sci U S A, 2015. **112**(3): p. 713-8.

36. Le, J.V., et al., *Probing Nucleosome Stability with a DNA Origami Nanocaliper.* ACS Nano, 2016. **10**(7): p. 7073-84.

37. Hudoba, M.W., et al., *Dynamic DNA Origami Device for Measuring Compressive Depletion Forces.* ACS Nano, 2017. **11**(7): p. 6566-6573.

38. Samanta, A. and I.L. Medintz, *Nanoparticles and DNA - a powerful and growing functional combination in bionanotechnology.* Nanoscale, 2016. **8**(17): p. 9037-9095.

39. Liu, W.Y., et al., *Self-organized architectures from assorted DNA-framed nanoparticles.* Nature Chemistry, 2016. **8**(9): p. 867-873.

40. Liu, W.Y., et al., *Diamond family of nanoparticle superlattices.* Science, 2016. **351**(6273): p. 582-586.

41. Tian, Y., et al., *Prescribed nanoparticle cluster architectures and low-dimensional arrays built using octahedral DNA origami frames.* Nature Nanotechnology, 2015. **10**(7): p. 637-+.

42. Wang, P.F., et al., *Programming Self-Assembly of DNA Origami Honeycomb Two-Dimensional Lattices and Plasmonic Metamaterials.* Journal of the American Chemical Society, 2016. **138**(24): p. 7733-7740.

43. Schreiber, R., et al., *Ordering Gold Nanoparticles with DNA Origami Nanoflowers.* Acs Nano, 2016. **10**(8): p. 7303-7306.

44. Kuzyk, A., et al., *DNA-based self-assembly of chiral plasmonic nanostructures with tailored optical response.* Nature, 2012. **483**(7389): p. 311-314.

45. Schreiber, R., et al., *Chiral plasmonic DNA nanostructures with switchable circular dichroism.* Nat Commun, 2013. **4**: p. 2948.

46. Zhou, C., X.Y. Duan, and N. Liu, *A plasmonic nanorod that walks on DNA origami.* Nature Communications, 2015. **6**.

47. Lan, X., et al., *Au Nanorod Helical Superstructures with Designed Chirality.* Journal of the American Chemical Society, 2015. **137**(1): p. 457-462.

48. Urban, M.J., et al., *Plasmonic Toroidal Metamolecules Assembled by DNA Origami.* Journal of the American Chemical Society, 2016. **138**(17): p. 5495-5498.

49. Pal, S., et al., *DNA Directed Self-Assembly of Anisotropic Plasmonic Nanostructures.* Journal of the American Chemical Society, 2011. **133**(44): p. 17606-17609.

50. Kuzyk, A., et al., *Reconfigurable 3D plasmonic metamolecules.* Nature Materials, 2014. **13**(9): p. 862-866.

51. Acuna, G.P., et al., *Fluorescence Enhancement at Docking Sites of DNA-Directed Self-Assembled Nanoantennas.* Science, 2012. **338**(6106): p. 506-510.

52. Pal, S., et al., *Quantum Efficiency Modification of Organic Fluorophores Using Gold Nanoparticles on DNA Origami Scaffolds.* Journal of Physical Chemistry C, 2013. **117**(24): p. 12735-12744.

53. Kuhler, P., et al., *Plasmonic DNA-Origami Nanoantennas for Surface-Enhanced Raman Spectroscopy.* Nano Letters, 2014. **14**(5): p. 2914-2919.

54. Samanta, A., et al., *Fluorescence Quenching of Quantum Dots by Gold Nanoparticles: A Potential Long Range Spectroscopic Ruler.* Nano Letters, 2014. **14**(9): p. 5052-5057.

55. Ko, S.H., K. Du, and J.A. Liddle, *Quantum-Dot Fluorescence Lifetime Engineering with DNA Origami Constructs.* Angewandte Chemie-International Edition, 2013. **52**(4): p. 1193-1197.

56. Fu, J., et al., *Interenzyme substrate diffusion for an enzyme cascade organized on spatially addressable DNA nanostructures.* J Am Chem Soc, 2012. **134**(12): p. 5516-9.

57. Fu, J., et al., *Multi-enzyme complexes on DNA scaffolds capable of substrate channelling with an artificial swinging arm.* Nat Nanotechnol, 2014. **9**(7): p. 531-6.

58. Zhao, Z., et al., *Nanocaged enzymes with enhanced catalytic activity and increased stability against protease digestion.* Nat Commun, 2016. **7**: p. 10619.

59. Derr, N.D., et al., *Tug-of-war in motor protein ensembles revealed with a programmable DNA origami scaffold.* Science, 2012. **338**(6107): p. 662-5.

60. Shaw, A., et al., *Spatial control of membrane receptor function using ligand nanocalipers.* Nat Methods, 2014. **11**(8): p. 841-6.

61. Lauterbur, P.C., *Image Formation by Induced Local Interactions: Examples Employing Nuclear Magnetic Resonance.* Nature, 1973. **242**(5394): p. 190-191.

62. Mansfield, P., *Multi-planar image formation using NMR spin echoes.* Journal of Physics C: Solid State Physics, 1977. **10**(3): p. L55-L58.

63. Suetens, P., *Fundamentals of medical imaging*. Third edition. ed. 2017, Cambridge: Cambridge University Press. xi, 257 pages.

64. Bulte, J.W. and D.L. Kraitchman, *Iron oxide MR contrast agents for molecular and cellular imaging.* NMR Biomed, 2004. **17**(7): p. 484-99.

65. Vuong, Q.L., et al., *Magnetic resonance relaxation induced by superparamagnetic particles used as contrast agents in magnetic resonance imaging: a theoretical review.* Wiley Interdiscip Rev Nanomed Nanobiotechnol, 2017. **9**(6).

66. Vuong, Q.L., P. Gillis, and Y. Gossuin, *Monte Carlo simulation and theory of proton NMR transverse relaxation induced by aggregation of magnetic particles used as MRI contrast agents.* J Magn Reson, 2011. **212**(1): p. 139-48.

67. Vuong, Q.L., et al., *A universal scaling law to predict the efficiency of magnetic nanoparticles as MRI T(2)-contrast agents.* Adv Healthc Mater, 2012. **1**(4): p. 502-12.

68. Na, H.B., I.C. Song, and T. Hyeon, *Inorganic Nanoparticles for MRI Contrast Agents.* Advanced Materials, 2009. **21**(21): p. 2133-2148.

69. Gupta, A.K. and M. Gupta, *Synthesis and surface engineering of iron oxide nanoparticles for biomedical applications.* Biomaterials, 2005. **26**(18): p. 3995-4021.

70. Wang, Y.X., *Superparamagnetic iron oxide based MRI contrast agents: Current status of clinical application.* Quant Imaging Med Surg, 2011. **1**(1): p. 35-40.

71. Qiao, R.R., C.H. Yang, and M.Y. Gao, *Superparamagnetic iron oxide nanoparticles: from preparations to in vivo MRI applications.* Journal of Materials Chemistry, 2009. **19**(35): p. 6274-6293.

72. Chandrasekharan, P., et al., *Vitamin E (D-alpha-tocopheryl-co-poly(ethylene glycol) 1000 succinate) micelles-superparamagnetic iron oxide nanoparticles for enhanced thermotherapy and MRI.* Biomaterials, 2011. **32**(24): p. 5663-5672.

73. Landazuri, N., et al., *Magnetic Targeting of Human Mesenchymal Stem Cells with Internalized Superparamagnetic Iron Oxide Nanoparticles.* Small, 2013. **9**(23): p. 4017-4026.

74. Sathe, T.R., A. Agrawal, and S.M. Nie, *Mesoporous silica beads embedded with semiconductor quantum dots and iron oxide nanocrystals: Dual-function microcarriers for optical encoding and magnetic separation.* Analytical Chemistry, 2006. **78**(16): p. 5627-5632.

75. Sun, C.R., et al., *PEG-Mediated Synthesis of Highly Dispersive Multifunctional Superparamagnetic Nanoparticles: Their Physicochemical Properties and Function In Vivo.* Acs Nano, 2010. **4**(4): p. 2402-2410.

76. Kalambur, V.S., et al., *In vitro characterization of movement, heating and visualization of magnetic nanoparticles for biomedical applications.* Nanotechnology, 2005. **16**(8): p. 1221-1233.

77. Yavuz, C.T., et al., *Low-field magnetic separation of monodisperse Fe3O4 nanocrystals.* Science, 2006. **314**(5801): p. 964-967.

78. Zhu, H.B., et al., *Spatial control of in vivo CRISPR-Cas9 genome editing via nanomagnets.* Nature Biomedical Engineering, 2019. **3**(2): p. 126-136.

79. Lee, G.Y., et al., *Theranostic Nanoparticles with Controlled Release of Gemcitabine for Targeted Therapy and MRI of Pancreatic Cancer.* Acs Nano, 2013. **7**(3): p. 2078-2089.

80. Santhosh, P.B. and N.P. Ulrih, *Multifunctional superparamagnetic iron oxide nanoparticles: Promising tools in cancer theranostics.* Cancer Letters, 2013. **336**(1): p. 8-17.

81. Peng, X.H., et al., *Targeted magnetic iron oxide nanoparticles for tumor imaging and therapy.* International Journal of Nanomedicine, 2008. **3**(3): p. 311-321.

82. Lee, N., et al., *Water-dispersible ferrimagnetic iron oxide nanocubes with extremely high r(2) relaxivity for highly sensitive in vivo MRI of tumors.* Nano Lett, 2012. **12**(6): p. 3127-31.

83. Roch, A., et al., *Superparamagnetic colloid suspensions: Water magnetic relaxation and clustering.* Journal of Magnetism and Magnetic Materials, 2005. **293**(1): p. 532-539.

84. Matsumoto, Y. and A. Jasanoff, *T2 relaxation induced by clusters of superparamagnetic nanoparticles: Monte Carlo simulations.* Magn Reson Imaging, 2008. **26**(7): p. 994-8.

85. Berret, J.F., et al., *Controlled clustering of superparamagnetic nanoparticles using block copolymers: design of new contrast agents for magnetic resonance imaging.* J Am Chem Soc, 2006. **128**(5): p. 1755-61.

86. Poselt, E., et al., *Relaxivity optimization of a PEGylated iron-oxide-based negative magnetic resonance contrast agent for T(2)-weighted spin-echo imaging.* ACS Nano, 2012. **6**(2): p. 1619-24.

87. Balasubramaniam, S., et al., *Toward design of magnetic nanoparticle clusters stabilized by biocompatible diblock copolymers for T(2)-weighted MRI contrast.* Langmuir, 2014. **30**(6): p. 1580-7.

88. Yoon, T.J., et al., *Multicore assemblies potentiate magnetic properties of biomagnetic nanoparticles.* Adv Mater, 2011. **23**(41): p. 4793-7.

89. Bruns, O.T., et al., *Real-time magnetic resonance imaging and quantification of lipoprotein metabolism in vivo using nanocrystals.* Nat Nanotechnol, 2009. **4**(3): p. 193-201.

90. Perez, J.M., et al., *Magnetic relaxation switches capable of sensing molecular interactions.* Nat Biotechnol, 2002. **20**(8): p. 816-20.

91. Perez, J.M., et al., *Viral-induced self-assembly of magnetic nanoparticles allows the detection of viral particles in biological media.* J Am Chem Soc, 2003. **125**(34): p. 10192-3.

92. Grimm, J., et al., *Novel nanosensors for rapid analysis of telomerase activity.* Cancer Res, 2004. **64**(2): p. 639-43.

93. Perez, J.M., et al., *DNA-based magnetic nanoparticle assembly acts as a magnetic relaxation nanoswitch allowing screening of DNA-cleaving agents.* J Am Chem Soc, 2002. **124**(12): p. 2856-7.

94. Perez, J.M., et al., *Peroxidase Substrate Nanosensors for MR Imaging.* Nano Letters, 2004. **4**(1): p. 119-122.

95. Zhao, M., et al., *Magnetic sensors for protease assays.* Angew Chem Int Ed Engl, 2003. **42**(12): p. 1375-8.

96. Gallo, J., et al., *CXCR4-targeted and MMP-responsive iron oxide nanoparticles for enhanced magnetic resonance imaging.* Angew Chem Int Ed Engl, 2014. **53**(36): p. 9550-4.

97. Taktak, S., R. Weissleder, and L. Josephson, *Electrode chemistry yields a nanoparticle-based NMR sensor for calcium.* Langmuir, 2008. **24**(14): p. 7596-8.

98. Atanasijevic, T., et al., *Calcium-sensitive MRI contrast agents based on superparamagnetic iron oxide nanoparticles and calmodulin.* Proc Natl Acad Sci U S A, 2006. **103**(40): p. 14707-12.

99. Tsourkas, A., et al., *Magnetic relaxation switch immunosensors detect enantiomeric impurities.* Angew Chem Int Ed Engl, 2004. **43**(18): p. 2395-9.

100. Sun, E.Y., R. Weissleder, and L. Josephson, *Continuous analyte sensing with magnetic nanoswitches.* Small, 2006. **2**(10): p. 1144-7.

101. Kim, G.Y., et al., *Magnetic relaxation switch detection of human chorionic gonadotrophin.* Bioconjug Chem, 2007. **18**(6): p. 2024-8.

102. Chen, Y.P., et al., *Immunosensor based on magnetic relaxation switch and biotin-streptavidin system for the detection of Kanamycin in milk.* Biosens Bioelectron, 2013. **39**(1): p. 112-7.

103. Daniel, K.D., et al., *Implantable diagnostic device for cancer monitoring.* Biosens Bioelectron, 2009. **24**(11): p. 3252-7.

104. Ling, Y., et al., *Implantable magnetic relaxation sensors measure cumulative exposure to cardiac biomarkers.* Nature biotechnology, 2011. **29**(3): p. 273.

105. Brown, K.A., et al., *Scaling of transverse nuclear magnetic relaxation due to magnetic nanoparticle aggregation.* Journal of magnetism and magnetic materials, 2010. **322**(20): p. 3122-3126.

106. Min, C., et al., *Mechanism of Magnetic Relaxation Switching Sensing.* ACS Nano, 2012. **6**(8): p. 6821-6828.

107. Hak, S., et al., *Transverse relaxivity of iron oxide nanocrystals clustered in nanoemulsions: Experiment and theory.* Magnetic Resonance in Medicine, 2015. **74**(3): p. 858-867.

108. Zhou, Z., et al., *Artificial local magnetic field inhomogeneity enhances T2 relaxivity.* Nature Communications, 2017. **8**: p. 15468.

109. Ryu, Y., et al., *Size-Controlled Construction of Magnetic Nanoparticle Clusters Using DNA-Binding Zinc Finger Protein.* Angewandte Chemie International Edition, 2015. **54**(3): p. 923-926.

110. Amos, L.A., *Molecular motors: not quite like clockwork.* Cellular and Molecular Life Sciences, 2008. **65**(4): p. 509.

111. Vale, R.D., *The molecular motor toolbox for intracellular transport.* Cell, 2003. **112**(4): p. 467-80.

112. Vale, R.D. and R.A. Milligan, *The way things move: looking under the hood of molecular motor proteins.* Science, 2000. **288**(5463): p. 88-95.

113. Kay, E.R., D.A. Leigh, and F. Zerbetto, *Synthetic molecular motors and mechanical machines.* Angew Chem Int Ed Engl, 2007. **46**(1-2): p. 72-191.

114. von Delius, M. and D.A. Leigh, *Walking molecules.* Chemical Society Reviews, 2011. **40**(7): p. 3656-3676.

115. Shiroguchi, K. and K. Kinosita, *Myosin V walks by lever action and Brownian motion.* Science, 2007. **316**(5828): p. 1208-1212.

116. Schliwa, M. and G. Woehlke, *Molecular motors.* Nature, 2003. **422**(6933): p. 759-65.

117. Hirokawa, N., R. Nitta, and Y. Okada, *The mechanisms of kinesin motor motility: lessons from the monomeric motor KIF1A.* Nature Reviews Molecular Cell Biology, 2009. **10**(12): p. 877.

118. Block, S.M., *Kinesin motor mechanics: binding, stepping, tracking, gating, and limping.* Biophysical journal, 2007. **92**(9): p. 2986-2995.

119. Astumian, R.D. and M. Bier, *Mechanochemical coupling of the motion of molecular motors to ATP hydrolysis.* Biophysical journal, 1996. **70**(2): p. 637-653.

120. Hänggi, P. and F. Marchesoni, *Artificial Brownian motors: Controlling transport on the nanoscale.* Reviews of Modern Physics, 2009. **81**(1): p. 387.

121. Sherman, W.B. and N.C. Seeman, *A Precisely Controlled DNA Biped Walking Device.* Nano Letters, 2004. **4**(7): p. 1203-1207.

122. Shin, J.S. and N.A. Pierce, *A synthetic DNA walker for molecular transport.* J Am Chem Soc, 2004. **126**(35): p. 10834-5.

123. Gu, H., et al., *A proximity-based programmable DNA nanoscale assembly line.* Nature, 2010. **465**(7295): p. 202.

124. Bath, J., S.J. Green, and A.J. Turberfield, *A free-running DNA motor powered by a nicking enzyme.* Angewandte Chemie International Edition, 2005. **44**(28): p. 4358-4361.

125. Tian, Y., et al., *A DNAzyme that walks processively and autonomously along a one-dimensional track.* Angew Chem Int Ed Engl, 2005. **44**(28): p. 4355-8.

126. Green, S., J. Bath, and A. Turberfield, *Coordinated chemomechanical cycles: a mechanism for autonomous molecular motion.* Physical review letters, 2008. **101**(23): p. 238101.

127. Omabegho, T., R. Sha, and N.C. Seeman, *A bipedal DNA Brownian motor with coordinated legs.* Science, 2009. **324**(5923): p. 67-71.

128. Lund, K., et al., *Molecular robots guided by prescriptive landscapes.* Nature, 2010. **465**(7295): p. 206.

129. Pei, R., et al., *Behavior of Polycatalytic Assemblies in a Substrate-Displaying Matrix.* Journal of the American Chemical Society, 2006. **128**(39): p. 12693-12699.

130. Yehl, K., et al., *High-speed DNA-based rolling motors powered by RNase H.* Nat Nanotechnol, 2016. **11**(2): p. 184-90.

131. Jung, C., P.B. Allen, and A.D. Ellington, *A Simple, Cleated DNA Walker That Hangs on to Surfaces.* ACS Nano, 2017. **11**(8): p. 8047-8054.

132. Mason, S.D., et al., *Emerging bioanalytical applications of DNA walkers.* TrAC Trends in Analytical Chemistry, 2018. **107**: p. 212-221.

133. Chen, Y., et al., *A restriction enzyme-powered autonomous DNA walking machine: its application for a highly sensitive electrochemiluminescence assay of DNA.* Nanoscale, 2015. **7**(3): p. 981-986.

134. Peng, L., et al., *Bi-directional DNA walking machine and its application in an enzyme-free electrochemiluminescence biosensor for sensitive detection of microRNAs.* Analytical chemistry, 2017. **89**(9): p. 5036-5042.

135. Wang, D., et al., *A DNA walker as a fluorescence signal amplifier.* Nano letters, 2017. **17**(9): p. 5368-5374.

136. Li, C., et al., *Simple electrochemical sensing of attomolar proteins using fabricated complexes with enhanced surface binding avidity.* Chemical science, 2015. **6**(7): p. 4311-4317.

137. Li, W., L. Wang, and W. Jiang, *A catalytic assembled enzyme-free three-dimensional DNA walker and its sensing application.* Chemical Communications, 2017. **53**(40): p. 5527-5530.

138. Xu, Z., et al., *Ultrasensitive electrochemiluminescence biosensor for microRNA detection by 3D DNA walking machine based target conversion and distance-controllable signal quenching and enhancing.* Analytical chemistry, 2017. **89**(16): p. 8282-8287.

139. Chen, J., et al., *A target-triggered DNAzyme motor enabling homogeneous, amplified detection of proteins.* Analytical chemistry, 2017. **89**(23): p. 12888-12895.

140. Li, F., et al., *Binding-Induced Molecular Amplifier as a Universal Detection Platform for Biomolecules and Biomolecular Interaction.* Analytical chemistry, 2018. **90**(14): p. 8651-8657.

141. Peng, H., et al., *A microRNA-initiated DNAzyme motor operating in living cells.* Nature communications, 2017. **8**: p. 14378.

142. You, M., et al., *DNA probes for monitoring dynamic and transient molecular encounters on live cell membranes.* Nature nanotechnology, 2017. **12**(5): p. 453.

143. Cha, T.-G., et al., *A synthetic DNA motor that transports nanoparticles along carbon nanotubes.* Nature Nanotechnology, 2013. **9**: p. 39.

144. Thubagere, A.J., et al., *A cargo-sorting DNA robot.* Science, 2017. **357**(6356).

145. Meyer, T.A., C.A. Quinto, and G. Bao, *Control of iron oxide nanoparticle clustering using dual solvent exchange.* IEEE Magnetics Letters, 2015. **7**: p. 1-4.

146. Lee, N., et al., *Iron Oxide Based Nanoparticles for Multimodal Imaging and Magnetoresponsive Therapy.* Chem Rev, 2015. **115**(19): p. 10637-89.

147. Sadat, M.E., et al., *Effect of spatial confinement on magnetic hyperthermia via dipolar interactions in Fe3O4 nanoparticles for biomedical applications.* Materials Science and Engineering: C, 2014. **42**: p. 52-63.

148. Materia, M.E., et al., *Mesoscale assemblies of iron oxide nanocubes as heat mediators and image contrast agents.* Langmuir, 2015. **31**(2): p. 808-16.

149. Tong, S., et al., *Self-assembly of phospholipid–PEG coating on nanoparticles through dual solvent exchange.* Nano letters, 2011. **11**(9): p. 3720-3726.

150. Sun, S., et al., *Monodisperse mfe2o4 (m= fe, co, mn) nanoparticles.* Journal of the American Chemical Society, 2004. **126**(1): p. 273-279.

151. Stookey, L.L., *Ferrozine---a new spectrophotometric reagent for iron.* Analytical chemistry, 1970. **42**(7): p. 779-781.

152. Jun, Y.W., et al., *Nanoscale size effect of magnetic nanocrystals and their utilization for cancer diagnosis via magnetic resonance imaging.* J Am Chem Soc, 2005. **127**(16): p. 5732-3.

153. Laurent, S., et al., *Magnetic fluid hyperthermia: Focus on superparamagnetic iron oxide nanoparticles.* Advances in Colloid and Interface Science, 2011. **166**(1): p. 8-23.

154. Gonzales-Weimuller, M., M. Zeisberger, and K.M. Krishnan, *Size-dependant heating rates of iron oxide nanoparticles for magnetic fluid hyperthermia.* J Magn Magn Mater, 2009. **321**(13): p. 1947-1950.

155. Andreu, I., et al., *Same magnetic nanoparticles, different heating behavior: Influence of the arrangement and dispersive medium.* Journal of Magnetism and Magnetic Materials, 2015. **380**: p. 341-346.

156. Etheridge, M.L., et al., *Accounting for biological aggregation in heating and imaging of magnetic nanoparticles.* Technology (Singap World Sci), 2014. **2**(3): p. 214-228.

157. Branquinho, L.C., et al., *Effect of magnetic dipolar interactions on nanoparticle heating efficiency: implications for cancer hyperthermia.* Sci Rep, 2013. **3**: p. 2887.

158. Haase, C. and U. Nowak, *Role of dipole-dipole interactions for hyperthermia heating of magnetic nanoparticle ensembles.* Physical Review B, 2012. **85**(4): p. 045435.

159. Urtizberea, A., et al., *Specific absorption rates and magnetic properties of ferrofluids with interaction effects at low concentrations.* The Journal of Physical Chemistry C, 2010. **114**(11): p. 4916-4922.

160. Ghosh, D., et al., *M13-templated magnetic nanoparticles for targeted in vivo imaging of prostate cancer.* Nature nanotechnology, 2012. **7**(10): p. 677.

161. Rafati, A., A. Zarrabi, and P. Gill, *Fabrication of DNA nanotubes with an array of exterior magnetic nanoparticles.* Materials Science and Engineering: C, 2017. **79**: p. 216-220.

162. Douglas, S.M., J.J. Chou, and W.M. Shih, *DNA-nanotube-induced alignment of membrane proteins for NMR structure determination.* Proceedings of the National Academy of Sciences, 2007. **104**(16): p. 6644-6648.

163. Wagenbauer, K.F., et al., *How We Make DNA Origami.* ChemBioChem, 2017. **18**(19): p. 1873-1885.

164. Zhang, C., et al., *A general approach to DNA-programmable atom equivalents.* Nature Materials, 2013. **12**: p. 741.

165. Gates, E.P., et al., *Optimizing gold nanoparticle seeding density on DNA origami.* RSC Advances, 2015. **5**(11): p. 8134-8141.

166. Takabayashi, S., et al., *High precision and high yield fabrication of dense nanoparticle arrays onto DNA origami at statistically independent binding sites.* Nanoscale, 2014. **6**(22): p. 13928-13938.

167. Sharma, J., et al., *Toward Reliable Gold Nanoparticle Patterning On Self-Assembled DNA Nanoscaffold.* Journal of the American Chemical Society, 2008. **130**(25): p. 7820-7821.

168. Bui, H., et al., *Programmable Periodicity of Quantum Dot Arrays with DNA Origami Nanotubes.* Nano Letters, 2010. **10**(9): p. 3367-3372.

169. Amstad, E., et al., *Ultrastable Iron Oxide Nanoparticle Colloidal Suspensions Using Dispersants with Catechol-Derived Anchor Groups.* Nano Letters, 2009. **9**(12): p. 4042-4048.

170. Nandivada, H., X. Jiang, and J. Lahann, *Click Chemistry: Versatility and Control in the Hands of Materials Scientists.* Advanced Materials, 2007. **19**(17): p. 2197-2208.

171. Shaw, A., E. Benson, and B. Högberg, *Purification of Functionalized DNA Origami Nanostructures.* ACS Nano, 2015. **9**(5): p. 4968-4975.

172. Pan, J., et al., *Recent progress on DNA based walkers.* Curr Opin Biotechnol, 2015. **34**: p. 56-64.

173. Yin, P., et al., *A unidirectional DNA walker that moves autonomously along a track.* Angew Chem Int Ed Engl, 2004. **43**(37): p. 4906-11.

174. Ke, Y., *Designer three-dimensional DNA architectures.* Curr Opin Struct Biol, 2014. **27**: p. 122-8.

175. Wang, F., et al., *Programming Motions of DNA Origami Nanomachines.* Small, 2019: p. e1900013.

176. Korosec, C.S., M.J. Zuckermann, and N.R. Forde, *Dimensionality-dependent crossover in motility of polyvalent burnt-bridges ratchets.* Physical Review E, 2018. **98**(3): p. 032114.

177. Schnitzbauer, J., et al., *Super-resolution microscopy with DNA-PAINT.* Nature Protocols, 2017. **12**: p. 1198.

178. Kepten, E., et al., *Guidelines for the Fitting of Anomalous Diffusion Mean Square Displacement Graphs from Single Particle Tracking Experiments.* PLOS ONE, 2015. **10**(2): p. e0117722.